The electron's spin is a natural two-level system. It can be aligned parallel or antiparallel to an external magnetic field, with a certain energy difference between both system states. In the context of quantum information processing, those two spin orientations can be used to define the states of a qubit–a quantum mechanical two-level system with a complete set of manipulations and the requirement of tunable coupling to other qubits. However, an excited spin state may eventually relax into the ground state, and hereby lose its stored information. Knowing and understanding the mechanism of spin relaxation is crucial for the implementation of a spin-based quantum computer.

This work gives a comprehensive quantitative analysis of the relaxation of electron spins confined in top-gated, laterally coupled semiconductor quantum dots. We choose the two most prominent host materials for the dot implementation, gallium arsenide and silicon, and compare the characteristics of both semiconductors to each other. The quantum dot that we consider is loaded with either a single electron or with two electrons, which form singlet and triplet states. Highly accurate numerics supported by analytical approximations are presented and discussed for a wide range of system parameters, such as the external magnetic field, the interdot coupling strength, and the in-plane electric field (detuning). For the spin relaxation mechanism, we use the model of phonon-mediated transitions induced by spin-orbit or hyperfine coupling.

Universitätsverlag Regensburg

ISBN 978 3 86845 103 0

9 783868 451030

ISBN 978-3-86845-103-0

gefördert von:

Alumni der physikalischen Fakultät der Universität Regensburg e.V.

Universität Regensburg

Dissertationsreihe Physik - Band 35

Martin Raith

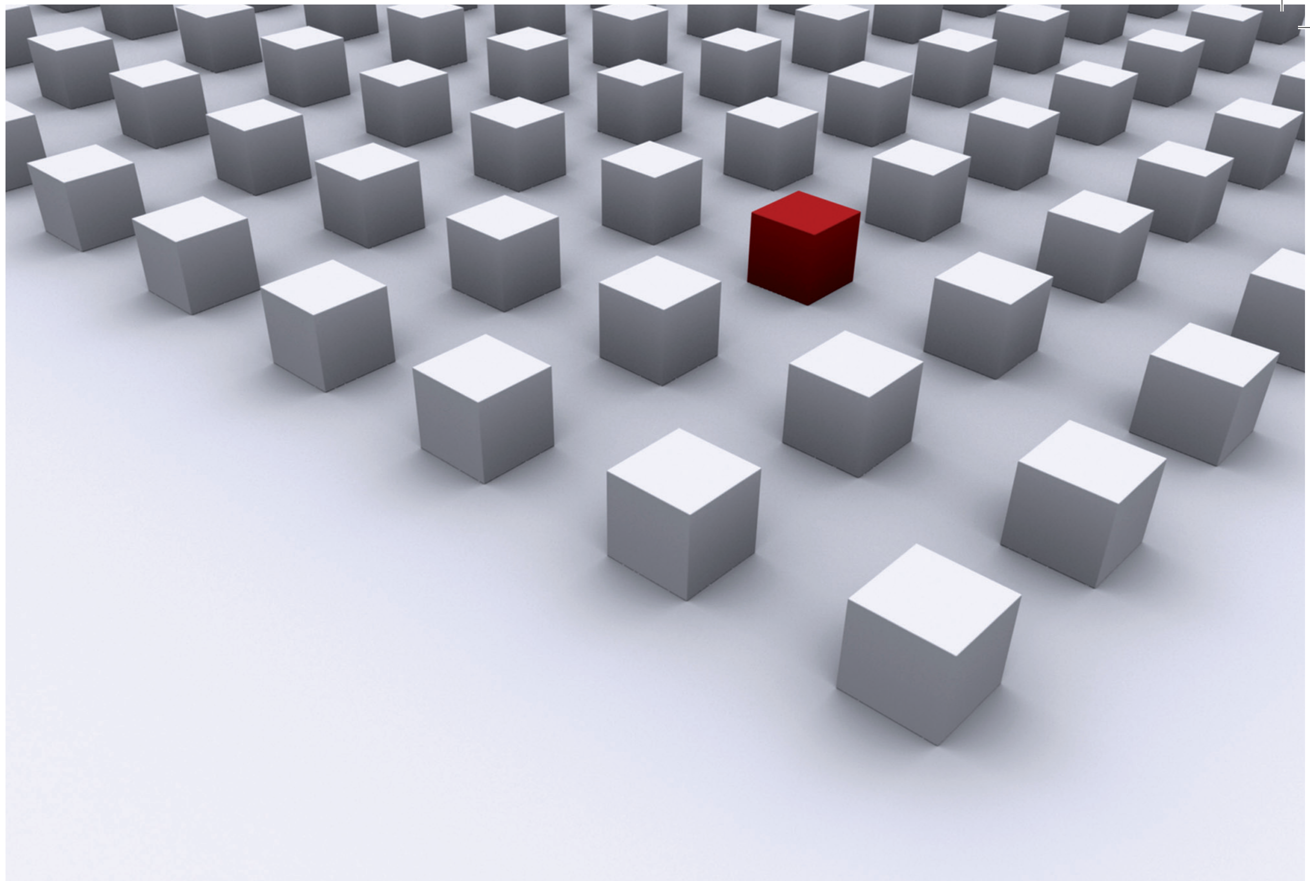

Martin Raith

Theory of Spin Relaxation in Laterally Coupled Quantum Dots

Universitätsverlag Regensburg

35

Dissertationsreihe Physik

Martin Raith

Theory of Spin Relaxation in Laterally Coupled Quantum Dots

Theory of Spin Relaxation in Laterally Coupled Quantum Dots

Dissertation zur Erlangung des Doktorgrades der Naturwissenschaften (Dr. rer. nat.)
der Fakultät für Physik der Universität Regensburg
vorgelegt von

Martin Raith
Regensburg
2013

Die Arbeit wurde von Prof. Dr. Jaroslav Fabian angeleitet.
Das Promotionsgesuch wurde am 06.05.2013 eingereicht.

Prüfungsausschuss: Vorsitzender: Prof. Dr. Dominique Bougeard
1. Gutachter: Prof. Dr. Jaroslav Fabian
2. Gutachter: Prof. Dr. John Schliemann
weiterer Prüfer: Prof. Dr. D. Weiss

Dissertationsreihe der Fakultät für Physik der Universität Regensburg, Band 35

Herausgegeben vom Präsidium des Alumnivereins der Physikalischen Fakultät:
Klaus Richter, Andreas Schäfer, Werner Wegscheider, Dieter Weiss

Martin Raith

Theory of Spin Relaxation in Laterally Coupled Quantum Dots

Universitätsverlag Regensburg

Bibliografische Informationen der Deutschen Bibliothek.
Die Deutsche Bibliothek verzeichnet diese Publikation
in der Deutschen Nationalbibliografie. Detailierte bibliografische Daten
sind im Internet über http://dnb.ddb.de abrufbar.

1. Auflage 2013
© 2013 Universitätsverlag, Regensburg
Leibnizstraße 13, 93055 Regensburg

Konzeption: Thomas Geiger
Umschlagentwurf: Franz Stadler, Designcooperative Nittenau eG
Layout: Martin Raith
Druck: Docupoint, Magdeburg
ISBN: 978-3-86845-103-0

Alle Rechte vorbehalten. Ohne ausdrückliche Genehmigung des Verlags ist es nicht gestattet, dieses Buch oder Teile daraus auf fototechnischem oder elektronischem Weg zu vervielfältigen.

Weitere Informationen zum Verlagsprogramm erhalten Sie unter:
www.univerlag-regensburg.de

Theory of Spin Relaxation in Laterally Coupled Quantum Dots

DISSERTATION

zur Erlangung des Doktorgrades
der Naturwissenschaften (Dr. rer. nat.)
der Fakultät für Physik
der Universität Regensburg

vorgelegt von
Martin Raith
aus Regensburg

im Jahr 2013

Promotionsgesuch eingereicht am: 06.05.2013
Das Promotionskolloquium fand am 23.07.2013 statt.
Die Arbeit wurde angeleitet von: Prof. Dr. Jaroslav Fabian

Prüfungsausschuss:
Vorsitzender: Prof. Dr. Dominique Bougeard
1. Gutachter: Prof. Dr. Jaroslav Fabian
2. Gutachter: Prof. Dr. John Schliemann
weiterer Prüfer: Prof. Dr. Dieter Weiss

Publication List

- M. Raith, P. Stano, and J. Fabian
  Theory of single electron spin relaxation in Si/SiGe lateral coupled quantum dots
  Phys. Rev. B **83**, 195318 (2011)
- M. Raith, P. Stano, F. Baruffa, and J. Fabian
  Theory of Spin Relaxation in Two-Electron Lateral Coupled Quantum Dots
  Phys. Rev. Lett. **108**, 246602 (2012)
- M. Raith, P. Stano, and J. Fabian
  Theory of spin relaxation in two-electron laterally coupled Si/SiGe quantum dots
  Phys. Rev. B **86**, 205321 (2012)

Contents

Publication List iii

1. Introduction 1

2. Electron Spins in Semiconductor Quantum Dots 5

3. Single-Electron Quantum Dots 15
- 3.1. Theoretical Model 16
- 3.2. Gallium Arsenide 20
- 3.3. Silicon 22
  - 3.3.1. Energy Spectrum 23
  - 3.3.2. Spin Relaxation 27
- 3.4. Summary 34

4. Two-Electron Quantum Dots 37
- 4.1. Theoretical Model 39
- 4.2. Gallium Arsenide 41
  - 4.2.1. Energy Spectrum 41
  - 4.2.2. Spin Relaxation 42
- 4.3. Silicon 51
  - 4.3.1. Energy Spectrum 51
  - 4.3.2. Spin Relaxation 55
- 4.4. Summary 68

5. Conclusions and Outlook 71

A. Numerical Method vii

Bibliography xv

CHAPTER 1

Introduction

Since the invention of the microprocessor more than 40 years ago [1], the computational power has reached a level of unforeseen limits. Computers have become the crucial companion in everyday life, and their ubiquity rises day by day. As seen from the validity of Moore's law [2], transistors become smaller and smaller and the performance growth seems unstoppable. But there is an end of the road—at least with the conventional computer architecture [3]. Quantum mechanics and thermodynamics set the ultimate limit for traditional scaling of silicon circuits, which provokes the quest for the "next switch" [4]. Besides the efforts to reinvent the classical computers, the new concept of quantum computation has emerged [5]. Information processing utilizing quantum bits (qubits), rather than classical bits, enables a new level of thinking [6]. With the power of quantum computers, we will enter a new age of performance leading to unimaginable opportunities. Yet, the vision is still fiction. This decade is in the name of the search for the best qubit architecture for large scale quantum computation, with a multitude of promising candidates currently investigated in today's research facilities all over the world.

A quantum computer could be used for "Simulating Physics with Computers" [7], as already proposed by Richard Feynman in 1982. Modern physics relies on quantum mechanics, but quantum systems are difficult to understand by classical means. A quantum computer could naturally use its quantum nature to attack such problems efficiently. In 1992, David Deutsch and Richard Jozsa presented an exemplary algorithm that scales exponentially on a classical computer, but is easy to handle on a quantum computer [8, 9]. It was the first to prove the capability of a quantum computer and the advantage over a classical one in an explicit case. Based on this inspiration, Peter Shor came up with a quantum algorithm for the factorization of integers [10], which could be used for cryptography [11], and Lov Grover invented a quantum search algorithm for unsorted databases [12, 13], useful for data mining [14]. Indeed, it was mathematically proven [15, 16] that the Grover algorithm is the fastest possible algorithm for this type of problem. Many other smart ideas followed, and down to the present day the list of quantum algorithms has grown impressively [17].

The key requirements on the hardware system of a quantum computer were specified by David DiVincenzo in 2000 [18]. Known as the DiVincenzo criteria, these requirements span the general framework of any candidate for the physical realization of a qubit. In a more modern (and more general) terminology given by Ladd et. al. [19], the DiVincenzo criteria demand

- “small enough” decoherence,
- scalability,
- universal logic, and
- correctability.

The real challenge of building a quantum computer is the interplay between those four competing points. For instance, a scalable system of qubits requires a strong isolation from the environment to ensure a long coherence time. However, initialization, manipulation, and read-out of the qubits must happen within a time frame much shorter than the decoherence time to ensure correctability [20]. This requires fast gates and therefore a strong coupling of the physical measurement instruments (which are part of the environment) to the qubits, causing decoherence even if unused. Finding a quantum system with a proper balance of the DiVincenzo criteria is the goal of all research efforts on candidates for the best qubit system.

Most approaches to the realization of a quantum computer are based on qubits that utilize the spin of electrons or nuclei. Hence, the physics of quantum information processing is closely related to the concepts of spintronics (spin-based electronics) [21–23]. Since the discovery of the giant magnetoresistance (GMR) in 1988 [24, 25], spintronics is in the focus of research for novel devices and applications in science and industry. In this thesis, we consider a true spintronic device—an electron spin trapped inside a semiconductor quantum dot that is controlled electrically. As a matter of fact, this system is a very promising candidate for a scalable qubit [26, 27]. The main goal of our work is to make realistic predictions for the lifetime of the information stored in a quantum-dot-based qubit.

Outline of the Thesis In *Chapter 1*, we started with a very brief historical overview of quantum computation and the motivation for building a quantum computer.

Chapter 2 is a more specific introduction. First, we briefly describe the best qubit candidates that are currently investigated, such as photon-based qubits, diamond defects, superconducting qubits, and semiconductor quantum dots. We take a closer look at the top-gated lateral quantum dots, the model system of our calculations, and comment on the two fundamental sources of decoherence, hyperfine coupling and spin-orbit coupling. Lateral quantum dot systems are typically fabricated in gallium arsenide or silicon heterostructures, and we discuss the main differences between both materials from a theoretical point of view. We pay special attention to the conduction band valleys in silicon, and comment on the valley splitting and possible implications for the realization of a coherent qubit. We also describe the spin relaxation mechanism that we consider throughout this thesis, and discuss an explicit experimental measurement of the spin lifetime in a two-electron quantum dot. The background of theoretical and experimental research on this topic is also given, putting this work into context.

The main part of the thesis is organized in two chapters. In *Chapter 3*, we restrict ourselves to quantum dots charged by a single electron. We introduce in Sec. 3.1 the theoretical model, which we use throughout this chapter, in a way suitable for both GaAs- and Si-based dots. For completeness, we comment in Sec. 3.2 on the well-understood single-electron GaAs quantum dots, and list relevant publications. In Sec. 3.3, we then present our numerical and analytical results on the electronic properties (Sec. 3.3.1) and the spin relaxation (Sec. 3.3.2) of silicon-based quantum dots. Hereby, we complete the comprehensive understanding of GaAs dots with a quantitative analysis of silicon dots, which satisfies a general trend seen in the community. Finally, we conclude this chapter in Sec. 3.4.

Chapter 4 is solely dedicated to two-electron quantum dots. In Sec. 4.1, we complete the theoretical model of Sec. 3.1 to cope with the second electron. We study GaAs quantum dots in Sec. 4.2, and silicon quantum dots in Sec. 4.3. For both systems, we use highly accurate numerics (further described in Appendix A) to investigate the influence of tunnel coupling and detuning on the electric properties and the spin relaxation. We pay special attention to the anisotropy of the spin relaxation, which originates from the spin-orbit field, and the interplay of spin-orbit and hyperfine coupling. An analytical calculation of the spin relaxation rate is presented in Sec. 4.3.2. The chapter summary is given in Sec. 4.4.

Final conclusions are given in *Chapter 5*. Here we also include two schemes for the nuclear spin polarization and the detection of a spin-polarized current, which directly rely on our findings in the previous chapters. We end this thesis with an outlook and comment on possible future directions of research.

CHAPTER 2

Electron Spins in Semiconductor Quantum Dots

The mathematical requirements of a qubit can be well described [18, 28]. Yet, scientists have been puzzling over the physical requirements for decades with no definite answer to date [19, 29, 30]. A multitude of smart ideas for a qubit hardware are investigated at present, each with particular advantages and disadvantages. The topic of this thesis supports an implementation that uses the spins of electrons confined in semiconductor quantum dots. The beauty of this approach is, if nothing else, its relation to semiconductor industry—the fabrication of such devices could easily be integrated in today's economic system. Nevertheless, there are many other promising candidates for the best qubit device [19, 29, 30], and we present some of them in short below. However, note that despite the outstanding progress in following most of the ideas, all current technologies struggle with the unresolved fundamental issue of scalability. This obstacle needs to be addressed in the future with appropriate attention.

Qubit Candidates A qubit can consist of a photon, with the information stored in the state of polarization. Photons are extremely robust against decoherence, which implies, in return, that they are hard to manipulate and control. Nevertheless, the proof of concept was given in 2009, when Politi et. al. demonstrated the implementation of the Shor algorithm [10] on a photonic chip [31]. The implementation relied on the Knill-Laflamme-Milburn (KLM) scheme [32], which is considered as the standard approach to a photon-based quantum computer today.

A great history of quantum computing research exists in the field of activity of trapped atoms. Here we can distinguish two different kinds of qubits: those consisting of trapped ions [33–37], and the ones working with trapped neutral atoms [38–41]. While entanglement of ions can be achieved e.g. through a laser-induced coupling [42–44], it is more challenging to control an interaction between neutral atoms. A promising approach is to use the Rydberg states of an atom, which have a very large electric dipole moment [45, 46]. The coherence time of trapped atom qubits is of the order of seconds [19], which is by all means long enough for initialization, manipulation, and readout. However, a major issue of these systems, maybe even more than for the others, is the lack of scalability.

Superconducting qubits [47, 48] have coherence times up to a few microseconds [49, 50]. Fabricated on a chip on "macroscopic" scale (up to $100\,\mu$m), they could as well take advantage of the achievements of the semiconductor industry. There are three types of superconducting qubits: the charge [50–54], the flux [55], and the phase qubit [56]. They all require Josephson junctions [47] to create some kind of anharmonicity on top of their otherwise harmonic potential landscape. Although two-qubit gate operations can be performed in superconductors within a few tens of nanoseconds [57], the search for fast and efficient gate operations that allow for fault-tolerant quantum information processing [58] remains an open issue in these systems [48, 59].

Diamond is a fascinating candidate for the best host material of a quantum computer [60]. The qubits in diamond can be defined by the electron spin of an impurity center (color center), with nitrogen-vacancy (N-V) centers being the most prominent because of their very long coherence times [60–62]. Readout [63], coherent control [64], and two-qubit gates [65] have successfully been demonstrated in such systems. Alternatively, information can be stored in the spin of a nitrogen [66, 67] or carbon atom [68, 69] that is nearby the N-V center. Today's efforts are toward an all-optical control of the diamond qubits [70] and scaling up.

In a similar device, the impurity is a phosphorus donor in silicon [71–74]. The qubit is given by the spin of either the donor electron or the nucleus of ^{31}P, with coherence times of seconds in isotopically purified silicon [75–77]. Worthy of mention, a nuclear spin of ^{29}Si can preserve coherence for minutes [78], yielding a possible alternative to the donor. The drawback of those systems is the lack of an efficient coupling of qubits, because of the extremely short-range exchange interaction. As in the case of diamond, a photonic connection could provide a solution.

The physical properties of graphene are outstanding, and many novel applications have already been proposed [79]. Besides classical high-frequency transistors [80, 81], a graphene-based quantum computer may also be feasible [82, 83]. Most concepts for a graphene qubit make use of the spin of a confined electron for information storage. However, a suitable confinement in graphene is hard to achieve due to Klein tunneling [84], which stems from the linear dispersion at the Fermi level, and dominant edge states that influence the electronic properties [85, 86]. To this day, there is no operational realization of an experimentally reliable qubit based on graphene.

Formerly known as artificial atoms, semiconductor quantum dots provide an engineered confinement that binds the electrons (or holes) at nanometer scale [87, 88]. The system develops discrete energy levels which are suitable for quantum information processing [27, 89, 90] or other tasks [91, 92] such as the use as a single-photon source [93].

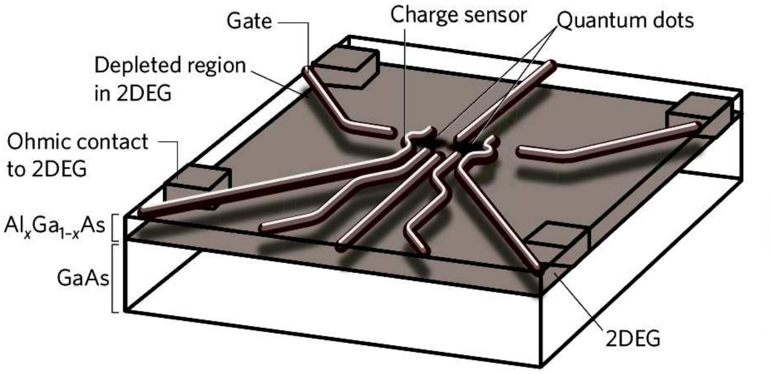

Figure 2.1.: Schematic drawing of a laterally coupled double quantum dot. The two-dimensional electron gas at the GaAs/AlGaAs interface is depleted by the electrostatic field of the top gates (indicated by shaded regions). The double dot forms at the center of the gate structure, with a charge sensor nearby each dot. (The figure is taken from Ref. [29]).

There are two prominent types of quantum dots: self-assembled (or self-organized) quantum dots [94, 95], and top-gated lateral quantum dots [96].[1] The former are three-dimensional, pyramid-like shaped structures at an interface of two semiconductors. The dots form spontaneously due to a difference in the lattice constants of the two constituents during the growth process at random locations.[2] Typically, a sample consists of many of those self-assembled dots, which are controlled optically [94]. Physical properties are measured as a statistical average over the whole dot ensemble [94].

The topic of this thesis is dedicated to the latter, the top-gated lateral quantum dots. They are created in a semiconductor heterostructure from a two-dimensional electron gas [96]. The dots are shaped by local depletion of the electron gas with electrostatic gates, which are spatially separated from the interface [98]. For a schematic sketch, see Figs. 2.1 and 2.2. In contrast to self-assembled dots, the dimensions of a gate-defined dot can be controlled electrically, and it has a definite location on the wafer determined by the lithographically fabricated gates. A measurement can address individual dots, which are typically manipulated electrically (through the gates) with an accompanying magnetic field [29]. Top-gated dots can be tuned with very high precision, which allows to store a single electron, a pair of electrons, or any other number.

A qubit requires a quantum-mechanical two-level system [5, 28]. Using laterally coupled quantum dots, there are a plenty of imaginative systems in the literature to

---

[1] For other systems such as vertical dots, see Refs. [92] and [96], and references therein.

[2] More advanced fabrication techniques can lead to a deterministic placement of the dots. See Ref. [97] for details.

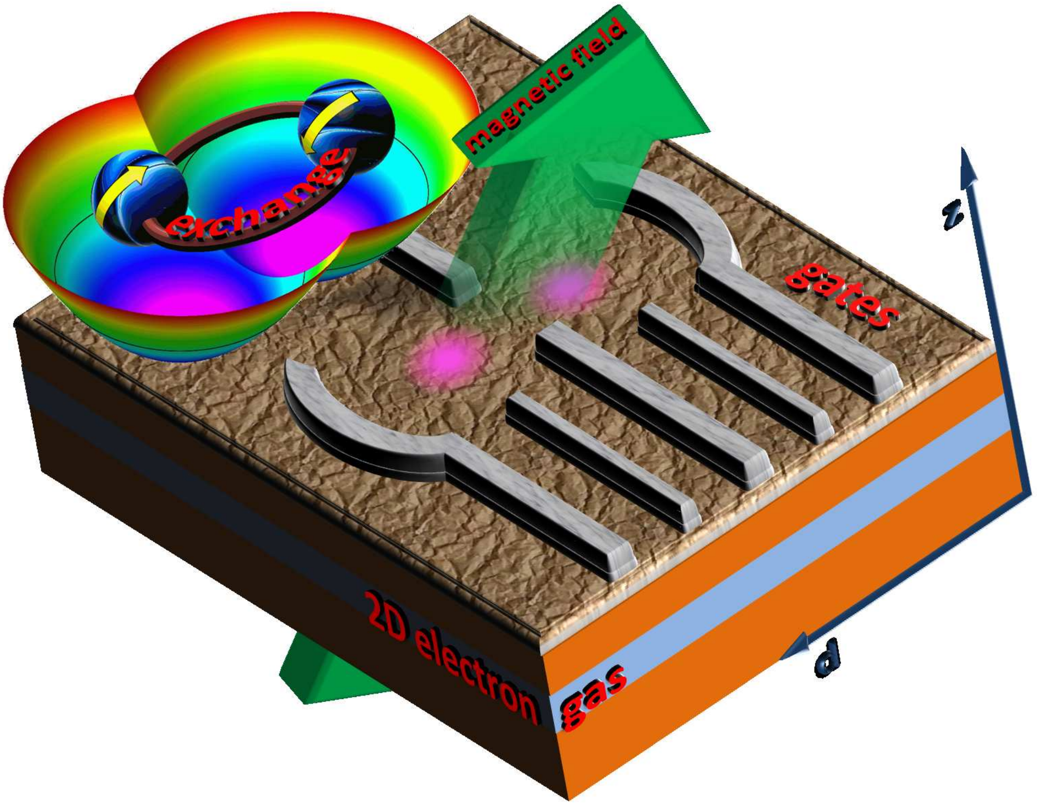

Figure 2.2.: Artist's view of a laterally coupled double quantum dot. The two-dimensional electron gas is locally depleted by top gates (shown in gray color) to form two potential minima (marked in pink). In this sketch, the double dot is charged with two electrons, connected through the exchange coupling. An arbitrarily oriented, external magnetic field is applied to the system (green arrow). The z-axis is along the growth direction of the heterostructure, and d indicates the in-plane direction connecting the dots.

represent a qubit [99]. Good candidates for a working quantum computer are presently the single-spin qubits (one electron in one dot) [100–102], and the singlet-triplet qubits (two electrons in two dots) [26, 103–106]. By calculating the spin relaxation of single and double dots charged with one electron (see Chap. 3), or with two electrons (see Chap. 4), we provide essential information for the realization of a qubit system based on the two best approaches to a quantum computer using gate-defined quantum dots to this day.

Semiconductor quantum dots have been in research focus for quantum information processing for more than a decade [22, 23, 27, 89, 100, 107–109]. In this domain, GaAs-based quantum dots are the state of the art [96, 110]. For those, the essential gate operations [28, 100, 111] for quantum computation [5, 18, 19] have already been demonstrated [26, 96, 101, 102, 104, 110, 112–116]. Electron spin measurements have been achieved using spin-to-charge conversion techniques [117]. Silicon-based quantum dots, on the other hand, are not yet as mature, but recent progress emphasizes their perspectives [118–128]. The spin-to-charge conversion was reported just recently [129]. In this work, we focus our research on laterally coupled double quantum dots based on those two semiconductors: gallium arsenide and silicon.

Quality of the Host Decoherence is the natural foe of any qubit implementation. In semiconductors, a serious effect causing decoherence is the coupling to the nuclei [130–132], and as a III-V semiconductor, GaAs possesses inherent nuclear spins ($I = 3/2$ for all naturally occurring isotopes of gallium and arsenic) [133–136]. Controlling this source of decoherence is of major interest and an active field of research [116, 137–144]. An alternative appears to be materials without nuclear magnetic moments, such as Si and C [19, 64, 78, 145–147]. Natural silicon consists of three isotopes, ^{28}Si (92.2%), ^{29}Si (4.7%), and ^{30}Si (3.1%) [136, 148]. Hereof only ^{29}Si has non-zero nuclear spin ($I = 1/2$), and purification can further reduce its abundance down to 0.05% [147, 149, 150].[3] For comparison, natural carbon has only two stable isotopes, ^{12}C (98.9%) and ^{13}C (1.1%) [82, 136], and only ^{13}C has a magnetic moment ($I = 1/2$), whose abundance can also be reduced by purification [145].

Another source of decoherence is spin-orbit coupling. Gallium (average relative atomic mass 69.723) and arsenic (74.922) are rather heavy atoms. Thus, spin-orbit coupling in GaAs systems is much stronger compared to the rather weak silicon (28.086) or carbon (12.011). This is a disadvantage of GaAs for most applications. However, because spin-orbit coupling is required for some spin manipulation schemes [96, 153], e.g. for the dynamical nuclear polarization [138, 154, 155], GaAs may also be advantageous in this context.

---

[3] A silicon-based top-gated lateral quantum dot is defined in a two-dimensional electron gas commonly formed at a Si/SiGe interface or in a MOS structure. Note that in natural germanium only ^{73}Ge (7.7%) has non-zero nuclear spin ($I = 9/2$) [136], which can also be purified [151, 152]. The SiO_2 interface has even better quality because natural oxygen is quite free of nuclear spins. The only isotope with non-zero nuclear spin is ^{17}O ($I = 5/2$), with an abundance of 0.04% [136].

Gallium arsenide is a direct band-gap semiconductor with zinc blende structure. Zinc blende is an FCC lattice with a two-atomic basis, such that each atom is positioned in the center of a regular tetrahedron formed by four atoms of the other species. The distance between different species is $\sqrt{3}a_0/4 = 2.45\,\text{Å}$, where $a_0 = 5.65\,\text{Å}$ is the lattice constant[4] [156, 157]. The low energy physics happens at the Γ point ($k = 0$), where the conduction band minimum is located. Consequently, GaAs is very suitable for the envelope function approximation (effective mass approximation), which is adopted for this work. It can be derived by the $\boldsymbol{k} \cdot \boldsymbol{p}$ method, see e.g. Refs. [23, 158–160] for details.

Silicon is an indirect band-gap semiconductor with diamond structure. The structure is essentially the zinc blende structure but with only one species of atoms. In the bulk, the conduction band minima are located at the X valleys, that is at $k_v \approx 0.84k_0$, $v = 1, \dots 6$, toward the six X points of the Brillouin zone, where $k_0 = 2\pi/a_0$ and $a_0 = 5.4\,\text{Å}$ is the lattice constant [156, 161–163]. In a (001)-grown Si heterostructure the valley degeneracy is partially lifted due to the presence of the interface and/or due to strain [162, 164], leaving a twofold conduction band minimum, the $\pm z$ valleys, which are separated from the fourfold excited valley states by at least 10 meV [161, 162, 165], large enough to neglect the upper four valleys [165–167]. The remaining twofold valley degeneracy is lifted if the perpendicular confinement is asymmetric. Then the orbital wave functions become symmetric and antisymmetric combinations of the single-valley states [168], which are separated by an energy difference called the ground-state gap [167] (or valley splitting) [166–174]. In recent years the origin and possible control of the valley splitting has been in focus.[5] Measurements in silicon heterostructures reveal a valley splitting of the order of μeV [164, 170, 176–180]. On the other hand, theoretical estimates of perfectly flat structures propose a splitting about three orders of magnitude larger [181]. Taking into account detailed properties of the interface (such as roughness), experiment and theory come to an agreement [128, 167–169, 171, 172, 182–186], and additional (in-plane) confinement allows the valley splitting to reach values of the order of meV [128, 171]. In Si/SiO$_2$ systems, the splitting can even be tens of meV [187–189]. In this work we assume that the valley splitting is larger than the typical energy scale of interest so that we can use the effective single-valley approximation [165, 190], in which only the lowest valley eigenstate is considered. This choice is strengthened by the fact that electron spins in valley-degenerate dots would not be viable qubits [165, 166, 190]. In fact, many recent experiments performed on Si/SiGe quantum dots have no evidence of valley degeneracy [125–127, 129, 191, 192], indicating that the splitting is large enough to justify a single valley treatment. Then, the silicon-based dots resemble the fairly well understood GaAs ones and we can use the same theoretical framework. On the other hand, a recent proposal of valley-defined qubits uses the valley degree of freedom as a tool for gate operations [193]. This requires precise control of the ground-state gap, a challenging task for the future.

---

[4] The lattice constant of a cubic crystal system such as zinc blende or diamond structure is the edge length of the cubic unit cell.

[5] An excellent review of the silicon valleys and the valley splitting is given in Ref. [175].

The in-plane effective mass in silicon is about three times larger compared to gallium arsenide. Therefore, the silicon dots must be about a factor of $\sqrt{3}$ smaller than the GaAs counterparts for a given energy scale. Because of that, and because of other characteristics such as strain[6], the fabrication of silicon dots is more challenging than of GaAs dots [195]. On the other hand, the larger g factor of silicon allows spin manipulations in smaller magnetic fields, which should be an advantage.

Spin Relaxation Spins in quantum dots are coupled to two environment baths: nuclear spins and phonons [130]. The decoherence of the spin state is dominated by the nuclei [96, 196] whereas the relaxation of energy-resolved spin states is induced by phonons. In this thesis we focus on the latter—the phonon-induced spin relaxation. It takes place only if the involved spin states are mixed, which can be due to spin-orbit coupling or the interaction with nuclear spins. A larger mixing favors a higher relaxation rate. The transition energy is absorbed by the emission of an acoustic phonon. Consequently, the relaxation is suppressed for small transition energies as here the phonon density of states is low. The dispersion relation of acoustic phonons can be assumed to be linear in this context. An anticrossing in the energy spectrum of two differing spin states, which is solely due to the nuclei or spin-orbit coupling, is called a spin hot spot [197]. Here, the transition rate between these two states is boosted by orders of magnitude because of the strong spin mixing even though the anticrossing gap is minute ($\sim \mu$eV) [198, 199]. Note that spectral crossings seem inevitable in manipulation schemes based on the Pauli spin blockade [100, 107], the current choice in spin qubit experiments [112]. For the electron-phonon couplings we use the model of deformation and piezoelectric potentials [200], noting that the latter is not present in silicon. The deformation potential of GaAs depends on longitudinal acoustic phonons only, while both longitudinal and transverse acoustic phonons are relevant in silicon [201–205].

There is an impressive history of theoretical and experimental research on semiconductor quantum dots. A review of single- and two-electron dots with experimental emphasis was published in 2007 by Hanson et. al. [96]. Quantum dots with more than two electrons were the topic of the review in 2002 by Reimann and Manninen [88]. And a review with special focus on silicon-based systems is written by Zwanenburg et. al. [175]. Most experimental achievements on the spin relaxation have been made with GaAs-based dots [133, 141, 198, 206–210], and the results are in agreement with

---

[6] Strain is inherently present in all Si/SiGe heterostructures because of the different lattice constants of silicon and germanium ($a_{\mathrm{Ge}} = 5.65$ Å, $a_{\mathrm{Si}} = 5.43$ Å [156, 160, 194]).

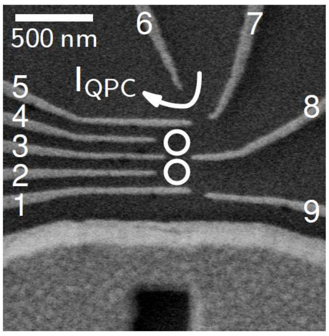

Figure 2.3: Scanning electron microscopy (SEM) [217] of a silicon-based laterally coupled double quantum dot. The circles indicate the locations of the electrostatic potential minima—the confinement. The top gates are numbered, and the nearby quantum point contact, defined by gate no. 6, is visualized by an arrow. (The figure is taken from Ref. [126]).

theoretical predictions [130, 153, 199, 211]. The experimental evolution of silicon-based dots is at a much earlier stage [195]. In silicon, the rates were measured on quantum dot ensembles [212, 213], on a many-electron quantum dot [192, 214], and a few electron quantum dot [126, 128, 129]. The single-electron regime was demonstrated only a few years ago [215, 216], and coherent singlet-triplet oscillations were reported just recently [127].

Let us have a closer look at the experiment of Prance et. al. on the spin relaxation in a Si/SiGe two-electron double dot, presented in Ref. [126]. The work demonstrates for the first time a single-shot readout of the triplet state in silicon. In contrast to averaging over signals of a quantum dot ensemble, the single-shot measurement needs only one entity to determine the characteristics of the system [198, 218]. The idea is to use spin-to-charge conversion [219–221], followed by a measurement of the charge state using a nearby quantum point contact [222] or another quantum dot [223]. In the experiment of Prance et. al., the double quantum dot is fabricated on a phosphorus-doped $\mathrm{Si/Si_{0.7}Ge_{0.3}}$ heterostructure. The electrons are confined in a quantum well of strained silicon, and the lateral dot shape is defined by the electric field of palladium top gates, shown in Fig. 2.3. The experiment is performed at a temperature of 15 mK, with a tunable, global magnetic field of up to 1 T parallel to the heterostructure plane. The number of electrons inside the double dot is found by creating a charge stability diagram [224, 225], that is the dots are first emptied and then recharged while counting electrons. An exemplary diagram of a comparable device in shown in Fig. 2.4. In the following, the double dot is steadily loaded with two electrons.

The spin lifetime of the triplet is measured by spin-to-charge conversion, which takes advantage of the Pauli spin blockade [87]. The measurement is all-electrical, meaning that it suffices to apply gate voltages in a certain sequence to probe the spin. The crucial manipulation in this case is detuning, i.e. applying an in-plane electric field parallel to the double dot such that a $(1,1)$ charge state (one electron in each dot) can be transformed into a $(2,0)$ or $(0,2)$ configuration (two electrons in the left or right dot). In Fig. 2.4, the effect of detuning is mapped to the diagonal of the charge stability diagram, say increasing V_R while decreasing V_L to go from $(1,1)$ across the

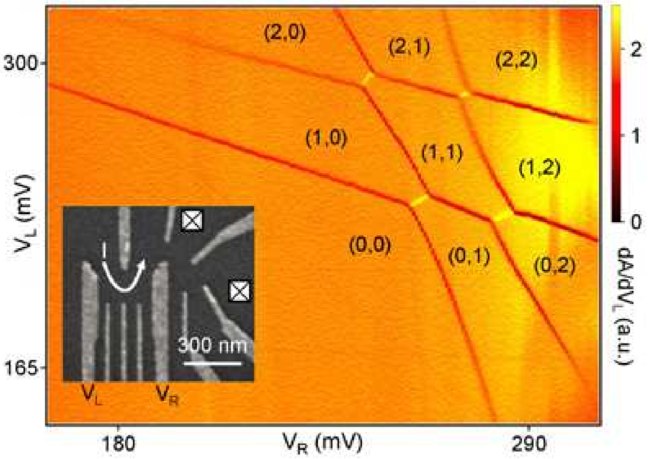

Figure 2.4.: Charge stability diagram of a silicon-based laterally coupled double quantum dot. The line shape draws regions of constant electron occupancy, as indicated by the labels (x, y) (x electrons in the left, and y electrons in the right dot). The largest region (at the bottom left) shows the $(0, 0)$ state—a fully emptied dot. While charging the dot, the electrons can be counted to determine the charge state (x, y). The inset shows a scanning electron microscopy (SEM) [217] of the given device. Note the additional quantum dot on the right hand side for charge measurements, which replaces the quantum point contact in conventional devices. (The figure is taken from Ref. [226]).

yellow transition line to $(0, 2)$. This is where the lifetime of the triplet can be measured, using the following readout sequence.[7]

At first, the double dot is initialized in the ground state of the $(0, 2)$ configuration, which is a singlet. Then, the detuning is decreased such that one electron jumps over to the other dot. After this step of preparation, the system is a singlet in the $(1, 1)$ configuration. But now the singlet and the triplets are close in energy, and thermal excitation, a coupling of states (for instance the hyperfine coupling due to nuclear spins), or a relaxation process (to the polarized ground state triplet in finite magnetic fields) can convert the singlet into a triplet state. The detuning is kept constant and the system evolves in time until the measurement is performed. For this purpose, the detuning is increased back toward to the initialization point, where the electrons tend to accumulate in one dot. A singlet state can now easily collapse back into the $(0, 2)$ ground-state singlet without the need to flip a spin (or the phase). On the contrary, a triplet is blocked in the $(1, 1)$ configuration, because the only accessible $(0, 2)$ state is the singlet, which requires a spin relaxation mechanism of some kind (to be explained later in the thesis). This situation is called Pauli spin blockade, and it is based upon the singlet-triplet energy splitting of two electrons in a single dot. For the measurement, the detuning is set to be in the range where the $(0, 2)$ singlet is the ground state, and the $(0,2)$ triplet is too high in energy. The time it takes until the $(1,1)$ triplet relaxes to the $(0,2)$ singlet can be measured with the help of the nearby quantum point contact. It is sensitive to the charge stored in the adjacent dot, thus it can detect whether there are one or two electrons in the right dot.

---

[7] We present other sequences in Chap. 5.

With this experiment, Prance et. al. measured a lifetime of the unpolarized triplet of about 10 ms, and up to 3 s for the polarized triplet in a magnetic field of 1 T [126]. This is of the same order as the related single-electron spin lifetimes found experimentally [129, 192, 214, 227], and about two orders of magnitude longer than in comparable GaAs dots [133, 209]. The data is also in good agreement with our findings presented in this thesis.

This Work in Context In the last decade, spin relaxation and decoherence rates were predicted by many authors for a variety of systems in certain regimes. Perturbative theories are available for single-dot single electron [228], and single- [202] and double-dot [229] singlet-triplet transitions. Non-perturbative approaches to semiconductor quantum dots so far focused on single dots [203, 230, 231], or vertical double dots [232, 233], in which the symmetry of the confinement potential lowers the numerical demands. A slightly deformed dot was considered in Refs. [234, 235], and a weakly detuned, strongly coupled double dot in Ref. [236].

We complete the existing theories by a comprehensive study of weakly coupled and biased double dots. The regimes we consider are the most important ones for spin qubit manipulations and the most relevant ones for ongoing experiments. Also, we give an unequaled thorough analysis of the relative roles of the spin-orbit and hyperfine interactions in the spin relaxation in quantum dots, particularly with respect to the spin hot spots [197]. The results are obtained non-perturbatively using exact numerical diagonalization (see Appendix A for details on the numerical method). We study the double dots for a wide range of parameters far beyond the validity of perturbative treatments. On the other hand, our findings are supported by analytical approaches where purposive.

CHAPTER 3

Single-Electron Quantum Dots

This chapter is dedicated to quantum dots that are charged with a single electron. In Sec. 3.1, we define our theoretical model, including the electron-phonon interaction and the spin relaxation. Gallium-arsenide based quantum dots are a mature field of research, and we comment on relevant findings in Sec. 3.2 to have a reference for the following. In Sec. 3.3 we focus on silicon-based dots. First, we briefly review the Si single and double dot spectra, paying attention to the states' orbital symmetries (Sec. 3.3.1). Then, we investigate the spin relaxation, starting with a single dot in an in-plane magnetic field (Sec. 3.3.2). Comparing our work to a recent experiment, we find that the results of the experiment indicate that the main spin relaxation channel is the mechanism we study here, and that the spin-orbit coupling strength of $\sim 0.1\,\mathrm{meV\,Å}$ seems realistic for Si/SiGe lateral quantum dots. We also present analytical formulas for the spin relaxation rate in the lowest order of the spin-orbit interactions. Comparing them to exact numerics, we demonstrate that these formulas are quantitatively reliable up to modest magnetic fields of 1-2 T. We find that a further analytical simplification often adopted, the isotropic averaging of the interaction strengths, leads to a result correct only within an order of magnitude. Later in Sec. 3.3.2, we deal with the double dot case and demonstrate that there the spin relaxation rate is sensitive to the spectral anticrossings (spin hot spots) [197], especially if the magnetic field is perpendicular to the heterostructure. For in-plane fields, the anisotropy of the spin-orbit interactions leads to the appearance of easy passages—magnetic field directions in which the relaxation rate is quenched by many orders of magnitude [199, 237, 238]. These results are analogous to the GaAs quantum dots, and we refer to the relevant publications. Finally, we summarize this chapter in Sec. 3.4.

3.1. Theoretical Model

The model describes a non-degenerate (with respect to the crystal symmetry) low-energy conduction band electron of semiconductors with isotropic effective mass within the envelope function approximation. For a lateral top-gated quantum dot, the electron motion along the heterostructure growth direction is frozen. The strong confinement induces an orbital energy level spacing larger than any other relevant energy scale, satisfying the approximation of two dimensions. The third dimension becomes relevant again if a magnetic field of about 10 Tesla or more is applied perpendicular to the growth direction [239]. Here we neglect any orbital effects of in-plane magnetic fields, and stick to the two-dimensional approximation throughout this thesis. In the following, we assume a $\hat{z} = [001]$ grown heterostructure. Due to the valley splitting in silicon, the relevant in-plane effective mass is isotropic, and we further assume the validity of the single-valley approximation (justified in Chap. 2). Within these assumptions, our model is eligible for gallium arsenide and for silicon based structures. The double dot we consider is occupied by a single, isolated electron, i.e. tunneling from or into the leads is forbidden. The Hamiltonian of the system reads as

$$H = T + V + H_{\mathrm{Z}} + H_{\mathrm{so}}, \tag{3.1}$$

with the following contributions:

We have the kinetic energy,

$$T = \frac{\mathbf{P}^2}{2m} = \frac{(-\mathrm{i}\hbar\nabla + e\mathbf{A})^2}{2m}, \tag{3.2}$$

with the proton charge e, and the effective electron mass m. We use the symmetric gauge, $\mathbf{A} = B_z\,(-y, x)\,/2$, adopting the neglect of perpendicular motion (the vector potential $\mathbf{A}$ is independent of the in-plane components of $\mathbf{B}$). Note that all vectors are two-dimensional, and we define the in-plane coordinates along the crystallographic axes, $\hat{x} = [100]$ and $\hat{y} = [010]$.

The double quantum dot is modeled by the biquadratic electrostatic confinement potential [165, 240, 241],

$$V = \frac{\hbar^2}{2ml_0^4}\min\{(\mathbf{r}-\mathbf{d})^2, (\mathbf{r}+\mathbf{d})^2\}. \tag{3.3}$$

The characteristic energy scale is given through the confinement length l_0 by the confinement energy $E_0 = \hbar^2/(ml_0^2)$. The vectors $\pm\mathbf{d}$ give the positions of the two potential minima, $d = 0$ describes the single dot. We define the angle δ between the main dot axis $\mathbf{d}$ and $\hat{x}$. The coupling strength of the dots is parametrized by the dimensionless interdot distance $2d/l_0$.

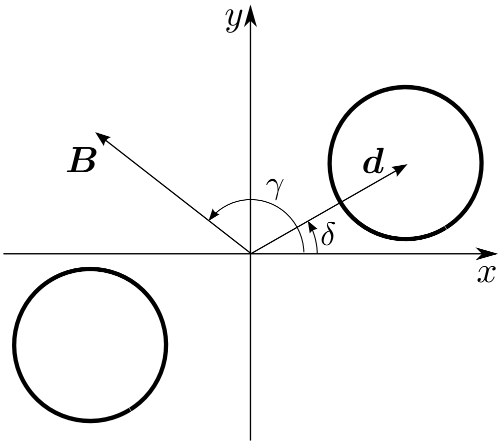

Figure 3.1: Orientation of the double dot in the coordinate system $\hat{x} = [100]$, $\hat{y} = [010]$. The potential minima, sketched by two circles, are parametrized by the position vectors $\pm\mathbf{d}$ or by the distance $2d$ and the angle δ. The in-plane magnetic field orientation is given by the angle γ.

The Zeeman energy reads as

$$H_{\mathrm{Z}} = (g/2)\,\mu_{\mathrm{B}}\boldsymbol{\sigma}\cdot\mathbf{B}. \tag{3.4}$$

It is proportional to the effective Landé factor g and a constant, the Bohr magneton μ_{B}. The vector $\boldsymbol{\sigma} = (\sigma_x, \sigma_y, \sigma_z)$ consists of the Pauli matrices. The magnetic field is given by $\mathbf{B} = (B_{||}\cos\gamma, B_{||}\sin\gamma, B_z)$, where γ is the angle between $\hat{x}$ and the in-plane component of $\mathbf{B}$. Figure 3.1 sketches the geometry.

The last term in Eq. (3.1),

$$H_{\mathrm{so}} = H_{\mathrm{br}} + H_{\mathrm{d}} + H_{\mathrm{d3}}, \tag{3.5}$$

accounts for the spin-orbit coupling of two-dimensional systems without inversion symmetry [22]. The structure inversion asymmetry arises, for example, from an electric field along the growth direction. It results in the Bychkov-Rashba Hamiltonian [22, 242],

$$H_{\mathrm{br}} = (\hbar/2ml_{\mathrm{br}})\,(\sigma_x P_y - \sigma_y P_x)\,, \tag{3.6}$$

with the spin-orbit length l_{br}, which is sensitive to, and hereby tunable by the perpendicular electric field. The bulk inversion asymmetry, as given in semiconductors with zinc blende structure such as GaAs, induces additional contributions—the Dresselhaus spin-orbit coupling [22, 243]. The linear Dresselhaus term reads as

$$H_{\mathrm{d}} = (\hbar/2ml_{\mathrm{d}})\,(-\sigma_x P_x + \sigma_y P_y)\,, \tag{3.7}$$

with the spin-orbit length l_{d}. The cubic Dresselhaus spin-orbit coupling is given by

$$H_{\mathrm{d3}} = \left(\gamma_c/2\hbar^3\right)\left(\sigma_x P_x P_y^2 - \sigma_y P_y P_x^2\right) + \mathrm{H.c.}, \tag{3.8}$$

where γ_c is a bulk parameter. Silicon has diamond structure. Consequently, the bulk symmetry of inversion does not allow for linear and cubic Dresselhaus spin-orbit couplings as given above. Instead, we consider for silicon the interface inversion asymmetry of heterostructures [23]. It gives rise to a Dresselhaus-like term [244, 245], which is of the same form as Eq. (3.7). Consequently, we can use Eq. (3.7) for both GaAs and Si, noting that l_d accounts for either type of asymmetry. Because the spin-orbit length l_d is in silicon about one or two magnitudes larger than in GaAs, we expect the higher-order contributions of the Dresselhaus-like spin-orbit coupling [namely the cubic term, Eq. (3.8)] also to be suppressed by at least one order of magnitude. In this work, we neglect the cubic contributions in silicon altogether.

The spin relaxation is mediated by low-energy acoustic phonons, and the accompanying spin-flip is allowed due to the presence of spin-orbit coupling. In our model, we consider the electron-phonon coupling of deformation and piezoelectric potentials, noting that the latter is absent in silicon. The coupling is described by

$$H_\mathrm{ep} = \mathrm{i} \sum_{\mathbf{Q},\lambda} \sqrt{\frac{\hbar Q}{2\rho V c_\lambda}} V_{\mathbf{Q},\lambda} \left[b^\dagger_{\mathbf{Q},\lambda} \mathrm{e}^{\mathrm{i}\mathbf{Q}\cdot\mathbf{R}} - b_{\mathbf{Q},\lambda} \mathrm{e}^{-\mathrm{i}\mathbf{Q}\cdot\mathbf{R}} \right], \tag{3.9}$$

with the phonon wave vector $\mathbf{Q} = (\mathbf{q}, Q_z)$, its unit vector $\hat{\mathbf{Q}}$, and the electron position vector $\mathbf{R} = (\mathbf{r}, z)$. The polarizations are given by $\lambda = t_1, t_2, l$ [160, 246], the polarization unit vector reads as $\hat{\mathbf{e}}$, and the phonon annihilation (creation) operator is denoted by b ($b^\dagger$). The mass density, the volume of the crystal, and the sound velocities are given by ρ, V, and c_λ, respectively. We switch between both effective phonon potentials with the choice of $V_{\mathbf{Q},\lambda}$. For the deformation potential, we use

$$V^\mathrm{df}_{\mathbf{Q},\lambda} = \Xi_\mathrm{d} \hat{\mathbf{e}}^\lambda_{\mathbf{Q}} \cdot \hat{\mathbf{Q}} + \Xi_\mathrm{u} \hat{\mathrm{e}}^\lambda_{\mathbf{Q},z} \hat{Q}_z, \tag{3.10}$$

and the piezoelectric potential is given by

$$V^\mathrm{pz}_{\mathbf{Q},\lambda} = -2\mathrm{i}eh_{14}(q_x q_y \hat{\mathrm{e}}^\lambda_{\mathbf{Q},z} + \mathrm{c.p.})/Q^3, \tag{3.11}$$

where c.p. stands for the cyclic permutation of $\{x, y, z\}$. The effective phonon potentials are parametrized by Ξ_d, Ξ_u, and h_{14}. In GaAs, the deformation potential is given by longitudinal phonons only. Adopting the common notation, we define $\Xi_\mathrm{d} = \sigma_e \delta_{\lambda,l}$, where σ_e is the deformation potential constant. Noting that $\Xi_\mathrm{u} = 0$, Eq. (3.10) then reads as $V^\mathrm{df}_{\mathbf{Q},\lambda} = \sigma_e \delta_{\lambda,l}$. The piezoelectric constant, h_{14}, is finite in zinc blende systems. In a (001)-grown silicon heterostructure, both the dilatation Ξ_d and the shear potential constant Ξ_u are finite, the latter accounting for the intravalley scattering within the z-valleys [201–205, 247].[1] There is no piezoelectric potential in diamond structures, i.e., $h_{14} = 0$.

---

[1] For the deformation potentials Ξ_d and Ξ_u, we stick to the notation by Herring and Vogt [201]. Note that the deformation potential Ξ_d represents a dilatation perpendicular to the growth direction while Ξ_u originates from a uniaxial strain parallel to the growth direction.

For the spin relaxation, we use Eq. (3.9) as a perturbation to the electronic system, and average over ensembles of the phonon system. The relaxation rate of a transition from state $|i\rangle$ into state $|j\rangle$ is given by Fermi's Golden Rule in the zero-temperature limit [23, 160, 199, 241, 248, 249],

$$\Gamma_{ij} = \frac{\pi}{\rho V} \sum_{\mathbf{Q},\lambda} \frac{Q}{c_\lambda} \left|V_{\mathbf{Q},\lambda}\right|^2 \left|M_{ij}\right|^2 \delta(E_{ij} - E_{\mathbf{Q}}^{\lambda}), \tag{3.12}$$

where $M_{ij} = \langle i|\mathrm{e}^{\mathrm{i}\mathbf{Q}\cdot\mathbf{R}}|j\rangle$ is the matrix element of the states with energy difference E_{ij}, and $E_{\mathbf{Q}}^{\lambda}$ is the energy of a phonon with wave vector $\mathbf{Q}$ and polarization λ. In the following, we define the relaxation rate, which is the inverse of the lifetime T_1, as the sum of the individual transition rates to all lower-lying states.

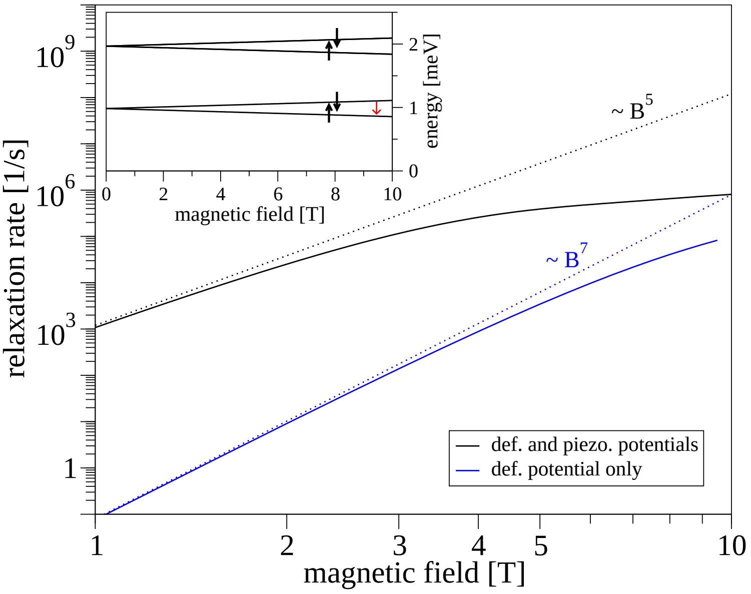

Figure 3.2.: Spin relaxation rate of a single electron in a GaAs-based single quantum dot as a function of in-plane magnetic field with orientation $\gamma = 135°$ (black, solid line). The auxiliary (black dotted) line emphasizes the B^5-dependence for low magnetic fields. The blue, solid line shows the spin relaxation switching off the piezoelectric potential, leaving only the deformation potential. For small magnetic fields, the rate follows a B^7-dependence, indicated by the auxiliary (blue dotted) line. The inset shows the corresponding energy spectrum, and the red arrow marks the transition states of the spin relaxation.

3.2. Gallium Arsenide

Theoretical research on single-electron quantum dots based on gallium arsenide has a longer tradition because of the experimental progress in the last two decades [87, 96, 250]. The influence of spin-orbit coupling on the single- [251–255] and double-dot [256, 257] energy spectrum has already been investigated. Quantitative results for the single-electron spin relaxation are also available [130, 198, 199, 210, 211, 238, 258] and in excellent agreement with experiments. For this reason, we skip a detailed discussion of the GaAs dot, and point to the named references instead. For silicon, a comparable work of reference is missing, and we complete the existing theories by a quantitative analysis of the silicon quantum dot in Sec. 3.3. For the purpose of comparison, we present in Fig. 3.2 an exemplary calculation of a GaAs-based single-electron single-dot spin relaxation rate as a function of the magnitude of an in-plane magnetic field. A corresponding graph of the silicon counterpart is given in Fig. 3.6. In both figures, we have the same magnetic field orientation ($\gamma = 135°$), and the dot parameters are chosen such that the confinement energy is $E_0 = 1\,\text{meV}$ in both systems ($l_0 = 34\,\text{nm}$ for GaAs, and $l_0 = 20\,\text{nm}$ for Si). In Fig. 3.2, we find that the total relaxation rate shows the expected B^5-dependence for small magnetic fields, which indicates that the dominant contribution comes from the piezoelectric potential [199]. We also plot the contribution of the deformation potential to the relaxation rate. It has a B^7-dependence for small magnetic fields as expected. We discuss Fig. 3.6 of the silicon dot in Sec. 3.3.2.

3.3. Silicon

In this section we present quantitative results of the energy spectrum and the spin relaxation for silicon-based single-electron double quantum dots.[2] In the following, we assume a (001)-grown SiGe/Si/SiGe quantum well, where the thin Si layer is sandwiched by the relaxed SiGe. To be more specific, we take a germanium concentration of about 25%, which is a typical value for real samples. The bulk electron effective mass of the X valleys is anisotropic in the directions longitudinal and transverse to the corresponding k_v-vector (see Chap. 2), given by $m_l = 0.916 m_e$ and $m_t = 0.191 m_e$, respectively, where m_e is the free electron mass. The in-plane mass of the z valley states is therefore the transverse mass [164, 174]. Due to the tensile strain (in-plane) of the Si layer [161, 194], the effective mass is slightly increased compared to the unstrained bulk Si, and we use $m = 0.198 m_e$ [260]. The effective Landé factor is $g = 2$ [171, 192, 261], and the spin-orbit lengths are set to be $l_{\mathrm{br}} = 38.5\,\mu\mathrm{m}$ and $l_{\mathrm{d}} = 12.8\,\mu\mathrm{m}$ for the Bychkov-Rashba and Dresselhaus-like spin-orbit coupling, respectively [245, 261]. Our choice is based on results of the theoretic tight-binding calculations of Ref. [245], as experimentally the spin-orbit coupling in silicon dots has not been measured up to date. We use the confinement energy $E_0 = 1\,\mathrm{meV}$, equivalent to the confinement length $l_0 = 20\,\mathrm{nm}$, which corresponds to realistic dot sizes [192, 262]. Our system is chosen to be in agreement with experimentally well established setups. For double dots, we use the orientation $\mathbf{d} \parallel [110]$ unless stated otherwise. The energy spectra for zero and non-zero magnetic fields are discussed in Sec. 3.3.1.

The spin relaxation of the single-electron silicon dot is presented in Sec. 3.3.2. The numerical results are obtained by the evaluation of Eq. (3.12), using the following parameters. The mass density is $\rho = 2.3 \times 10^3\,\mathrm{kg/m}^3$, and the velocities are given by $c_t = 5 \times 10^3$ m/s for transverse acoustic, and $c_l = 9.15 \times 10^3$ m/s for longitudinal acoustic phonons. The choice of deformation potential constants is not unique [263]. We use $\Xi_{\mathrm{d}} = 5\,\mathrm{eV}$ and $\Xi_{\mathrm{u}} = 9\,\mathrm{eV}$ according to Ref. [156], noting that other combinations such as $(\Xi_{\mathrm{d}}, \Xi_{\mathrm{u}}) = (1.1, 6.8)\,\mathrm{eV}$ [204], $(1.13, 9.16)\,\mathrm{eV}$, and $(-11.7, 9)\,\mathrm{eV}$ [205] appear in the literature as well. The needed electron wave functions and energies are obtained numerically as the eigensystem of the Hamiltonian in Eq. (3.1), which we diagonalize with the method of finite differences using the Dirichlet boundary condition (vanishing of the wave functions at the edge of the numerical grid). The magnetic field is included by the Peierls phase [264], and the diagonalization is carried out by the Lanczos algorithm. See Appendix A for more details on our numerical method. In this chapter, we use a grid of typically 50×50 points, which results in a relative precision in energy of 10^{-5} in zero magnetic field.

---

[2] Parts of Sec. 3.3 are based on Raith et. al., *Theory of single electron spin relaxation in Si/SiGe lateral coupled quantum dots*, Phys. Rev. B 83, 195318 (2011) [259].

	class	$\{E\}$	$\{I_x\}$	$\{I_y\}$	$\{I_{xy}\}$
irreducible repres.	Γ_1	1	1	1	1
	Γ_2	1	-1	1	-1
	Γ_3	1	-1	-1	1
	Γ_4	1	1	-1	-1

Table 3.1: Character table of the point group C_{2v}. The reflection operators with respect to the x and y axes are given by I_x and I_y, respectively. The point reflection is $I_{xy} = I_x I_y$, and the identity operator is denoted E. The four irreducible representations are labeled Γ_1, Γ_2, Γ_3, and Γ_4.

3.3.1. Energy Spectrum

Zero Magnetic Field In order to understand the details of the spin relaxation in silicon-based double quantum dots, we review briefly their electronic properties in zero magnetic field, including group theoretical classification, the influence of spin-orbit coupling, and the most important quantities for experiments. The Hamiltonian Eq. (3.1) for $\mathbf{B} = 0$ and without spin-orbit coupling has $C_{2v} \otimes SU(2)$ symmetry. We can label the orbital states according to the irreducible representations Γ_i, $i = 1, ..., 4$ of the Abelian point group C_{2v}, noting that each state is doubly spin-degenerate due to SU(2). This is done in Fig. 3.3, where the energy spectrum vs. the interdot distance in units of l_0 is plotted, and the corresponding character table is given in Table 3.1. Note that the potential V, Eq. (3.3), was chosen such that the states converge to Fock-Darwin states [87, 265, 266] in the limit of zero or infinite interdot distance. In the following we focus on the intermediate region where the interdot distance is comparable to the confining length. This is typically the region of experimental interest, as well as the one in which numerics becomes indispensable. Here we find several level crossings which may be lifted in the presence of spin-orbit coupling. Such anticrossings, also called spin hot spots [197], are of great importance for spin relaxation as we will see later. However, the linear spin-orbit coupling terms, Eq. (3.6) and Eq. (3.7), do not lead to level repulsion in the first order although allowed by symmetry [256]. The coupling can only be in higher order, which was analytically derived in Ref. [256] using Löwdin perturbation theory [158, 267, 268], which takes into account quasi-degenerate states exactly. We conclude that in zero magnetic field the double dot spectrum of silicon does not exhibit relevant spin hot spots.

For many applications including quantum dot spin qubits, the important physics happens at the bottom of the spectrum. We denote the spin-degenerate ground state as $\Gamma_1 \equiv \Gamma_S$ and the first excited state as $\Gamma_2 \equiv \Gamma_A$ to indicate the symmetry under inversion I_{xy}. The energy difference between these states is parametrized by the tunneling energy [256], $T = (E_A - E_S)/2$, a characteristic quantity for double quantum dots directly measurable experimentally [269]. Note that within the single-valley approximation we assumed a valley splitting of at least 1 meV which exceeds $2T$ at all interdot distances.

Using a linear combination of single dot orbitals (LCSDO) [256] we can approximate the exact wave functions by analytical expressions. Let $\Psi_{n,l}(\mathbf{r})$ be a Fock-Darwin state (omitting spin), where n is the principal and l the orbital quantum number [87, 265, 266].

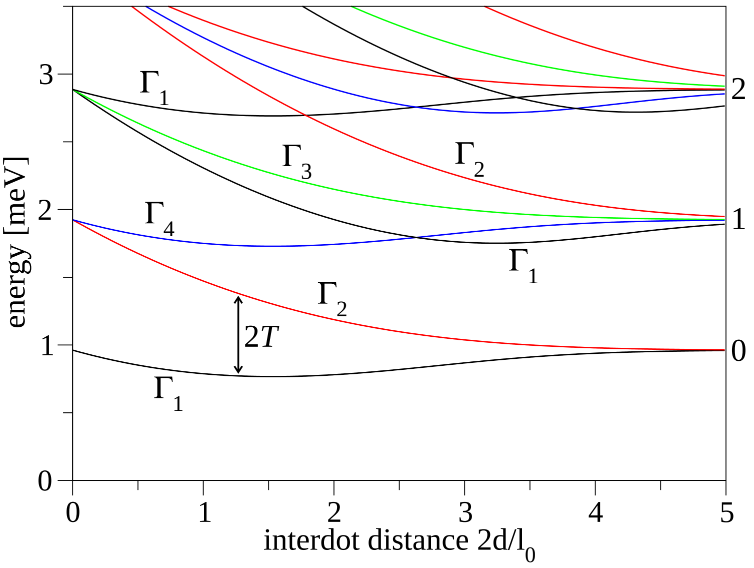

Figure 3.3.: Calculated energy spectrum of the silicon double quantum dot with respect to the interdot distance at zero magnetic field. The states are labeled (colored) according to the irreducible representations Γ_i of C_{2v}, see Table 3.1. On the right-hand side we give the highest orbital momentum of associated single dot states (Fock-Darwin states). The tunneling energy T is also shown.

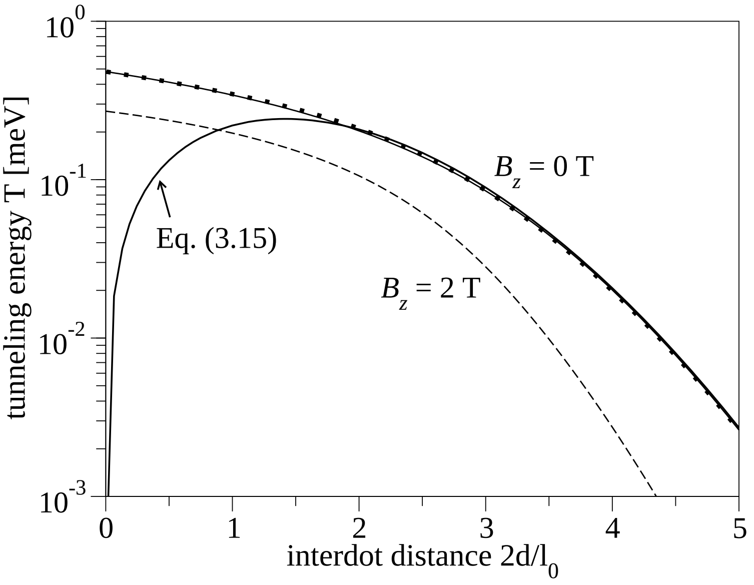

Figure 3.4.: Tunneling energy of the silicon double dot as given in Fig. 3.3 as a function of interdot distance for zero magnetic field, calculated by exact numerical diagonalization (dotted line), exact LCSDO formulas [Eq. (3.14), thin solid line] and leading order approximation [Eq. (3.15), thick solid line]. The tunneling energy for a finite perpendicular magnetic field ($B_z = 2\,\mathrm{T}$, dashed line) is given for comparison.

	class	$\{E\}$	$\{I_{xy}\}$
irred. rep.	Γ_{S}	1	1
	Γ_{A}	1	-1

Table 3.2: Character table of the point group C_2. The operator of point reflection is given by I_{xy}, and E is the identity. The two irreducible representations are labeled labeled Γ_{S}, and Γ_{A}.

Then the lowest orbital eigenstates of the double dot can be approximated using the Fock-Darwin states centered at the potential minima as

$$\begin{aligned}\Gamma_{\mathrm{S}} = &\ N_{+}\left[\Psi_{0,0}(\mathbf{r}+\mathbf{d})+\Psi_{0,0}(\mathbf{r}-\mathbf{d})\right],\\ \Gamma_{\mathrm{A}} = &\ N_{-}\left[\Psi_{0,0}(\mathbf{r}+\mathbf{d})-\Psi_{0,0}(\mathbf{r}-\mathbf{d})\right].\end{aligned} \tag{3.13}$$

Here $N_{\pm}$ are normalization constants. Calculating the eigenenergies as the expectation values of the Hamiltonian, Eq. (3.1), for zero magnetic field and without spin-orbit coupling, we obtain

$$\begin{aligned}E_{\mathrm{S}} &= E_0 \frac{1+\left[1-2d/\left(l_0\sqrt{\pi}\right)\right]\mathrm{e}^{-(d/l_0)^2}+(d/l_0)^2\,\mathrm{Erfc}(d/l_0)}{1+\mathrm{e}^{-(d/l_0)^2}},\\ E_{\mathrm{A}} &= E_0 \frac{1-\mathrm{e}^{-(d/l_0)^2}+(d/l_0)^2\,\mathrm{Erfc}(d/l_0)}{1-\mathrm{e}^{-(d/l_0)^2}},\end{aligned} \tag{3.14}$$

and through this the tunneling energy, which is plotted in Fig. 3.4. It is in excellent agreement with the exact numerical result. In the limit of large interdot distances the leading order reads as

$$T \approx E_0 \frac{d}{\sqrt{\pi}\, l_0}\mathrm{e}^{-(d/l_0)^2}, \tag{3.15}$$

which is a good approximation if $2d/l_0 > 2.5$.

In principle spin-orbit coupling terms affect the tunneling energy. However, it was shown [256] that this correction is of fourth order in the spin-orbit strengths α and/or β. For our parameters here it is of the order of peV and therefore negligible for all experimental purposes.

Non-Zero Magnetic Field In a perpendicular magnetic field without spin-orbit coupling, the group of the Hamiltonian becomes the Abelian point group C_2, see Table 3.2. The only remaining symmetry operator is the total inversion I_{xy}, and the one-dimensional irreducible representations have either symmetric or antisymmetric base functions. The spectrum of a double quantum dot in the perpendicular magnetic field is plotted in Fig. 3.5. The Zeeman interaction lifts the spin degeneracy, and the ground state, denoted as $\Gamma_{\mathrm{S}}^{\downarrow}$, is spin-polarized. Up to a certain magnitude of B_z (about 1.5 T for $2d/l_0 = 2.5$; see Fig. 3.5), the first excited state is $\Gamma_{\mathrm{S}}^{\uparrow}$, and the spin relaxation is the transition between these two wave functions with the same orbital parts and opposite spins. For larger magnetic fields the Zeeman splitting exceeds the orbital

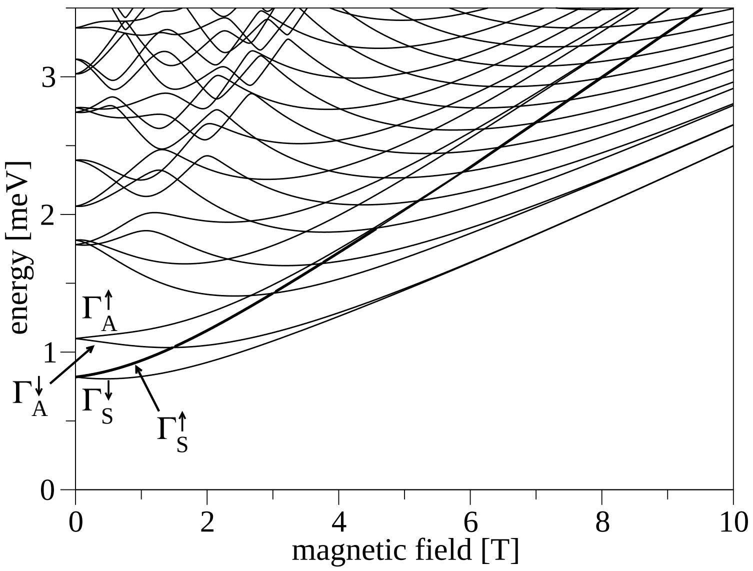

Figure 3.5.: Calculated energy spectrum of the silicon double quantum dot with interdot distance $2d/l_0 = 2.5$ plotted against the perpendicular magnetic field. The thick line indicates $\Gamma_S^\uparrow$, the lowest state with opposite spin-polarization compared to the ground state.

excitation energy and the first excited state is $\Gamma_A^\downarrow$, which has the same spin polarization as the ground state. For even higher fields more states fall below $\Gamma_S^\uparrow$, which all contribute to the spin relaxation. Note that the level spacings of interest at moderate magnetic fields are smaller than the assumed valley splitting, which again justifies the single-valley approximation.

Within the LCSDO, the single-dot wave functions acquire a phase when shifted. The building blocks in Eq. (3.13) are now given by $\Psi_{n,l}(\mathbf{r} \pm \mathbf{d}) \exp[\pm \mathrm{i} e B_z \mathbf{r} \cdot (\hat{z} \times \mathbf{d})/2\hbar]$, leading to

$$
\begin{aligned}
E_\mathrm{S} =& E_0 \frac{l_B^2}{l_0^2} \left(\frac{1 + \left[1 - d l_B^3 / \left(l_0^4 \sqrt{\pi}\right)\right] \mathrm{e}^{-d^2\left(2 l_B^{-2} - l_B^2 l_0^{-4}\right)}}{1 + \mathrm{e}^{-d^2\left(2 l_B^{-2} - l_B^2 l_0^{-4}\right)}} \right. \\
& \left. - \frac{d l_B^3 l_0^{-4} \left[\mathrm{e}^{-(d/l_B)^2} \pi^{-1/2} - d/l_B \operatorname{Erfc}(d/l_B)\right]}{1 + \mathrm{e}^{-d^2\left(2 l_B^{-2} - l_B^2 l_0^{-4}\right)}} \right), \\
E_\mathrm{A} =& E_0 \frac{l_B^2}{l_0^2} \left(\frac{1 - \left[1 - d l_B^3 / \left(l_0^4 \sqrt{\pi}\right)\right] \mathrm{e}^{-d^2\left(2 l_B^{-2} - l_B^2 l_0^{-4}\right)}}{1 - \mathrm{e}^{-d^2\left(2 l_B^{-2} - l_B^2 l_0^{-4}\right)}} \right. \\
& \left. - \frac{d l_B^3 l_0^{-4} \left[\mathrm{e}^{-(d/l_B)^2} \pi^{-1/2} - d/l_B \operatorname{Erfc}(d/l_B)\right]}{1 - \mathrm{e}^{-d^2\left(2 l_B^{-2} - l_B^2 l_0^{-4}\right)}} \right),
\end{aligned}
\tag{3.16}
$$

and we can repeat the computation of the tunneling energy with the result plotted in Fig. 3.4. One can see that the perpendicular magnetic field reduces the tunneling energy. This can be understood qualitatively as the renormalization of the confinement length, which is replaced by the effective (magneto-electric) confinement length l_B, where $l_B^{-4} = l_0^{-4} + l_\xi^{-4}$ with the auxiliary quantity $l_\xi = (2\hbar/B_z e)^{1/2}$. Using Eq. (3.16) in the limit of large interdot distances, the tunneling energy with a finite magnetic field simplifies to

$$T \approx E_0 \frac{d\, l_B}{\sqrt{\pi}\, l_0^2}\, \mathrm{e}^{-d^2\left(2l_B^{-2} - l_B^2 l_0^{-4}\right)}. \tag{3.17}$$

Note that for $B_z = 0$, we have $l_B = l_0$, and we recover Eq. (3.15).

3.3.2. Spin Relaxation

Single Quantum Dots Before we proceed to double dots, we first discuss a single quantum dot in an in-plane magnetic field, $\mathbf{B} = B_{\|}\,(\cos\gamma, \sin\gamma, 0)$, which already features anisotropies and relaxation rate spikes due to spin hot spots, as we will see. Removing the linear spin-orbit coupling terms in Eq. (3.1) with a unitary transformation [158, 267, 268, 270–272],[3]

$$U = \exp\left(\frac{\mathrm{i}}{2}\mathbf{n}_{\mathrm{so}} \cdot \boldsymbol{\sigma}\right), \tag{3.18}$$

where

$$\mathbf{n}_{\mathrm{so}} = \left(\frac{x}{l_{\mathrm{d}}} - \frac{y}{l_{\mathrm{br}}}, \frac{x}{l_{\mathrm{br}}} - \frac{y}{l_{\mathrm{d}}}, 0\right) \tag{3.19}$$

is the axis of the spin rotation, we find that the relaxation proceeds due to a spin-orbit-induced effective magnetic field [199, 238], given by

$$B_z^{\mathrm{eff}} = -B_{\|}\left[x\left(\frac{\cos\gamma}{l_{\mathrm{br}}} - \frac{\sin\gamma}{l_{\mathrm{d}}}\right) + y\left(\frac{\sin\gamma}{l_{\mathrm{br}}} - \frac{\cos\gamma}{l_{\mathrm{d}}}\right)\right], \tag{3.20}$$

which is perpendicular to the external magnetic field. The matrix element M_{ij} in Eq. (3.12) is proportional to this effective magnetic field, which results in the spin relaxation rate being proportional to the squared and inverse effective spin-orbit coupling length L [199, 237, 238],

$$L^{-2} = l_{\mathrm{br}}^{-2} + l_{\mathrm{d}}^{-2} - 2\sin(2\gamma)\, l_{\mathrm{br}}^{-1} l_{\mathrm{d}}^{-1}. \tag{3.21}$$

It is anisotropic since it depends on γ. However, the anisotropy disappears if one of the spin-orbit coupling lengths is dominant, particularly for $\beta = 0$. Thus, an experimental verification of the anisotropic single dot spin relaxation would verify the existence of the generalized Dresselhaus term, Eq. (3.7). The anisotropy is strongest if $l_{\mathrm{br}} = l_{\mathrm{d}}$, with the maximal rate at $\gamma = 135°$ and the minimal rate at $\gamma = 45°$.

---

[3] The transformed Hamiltonian reads as $\bar{H} = U^\dagger H U$, and $|\bar{\Psi}\rangle = U^\dagger |\Psi\rangle$.

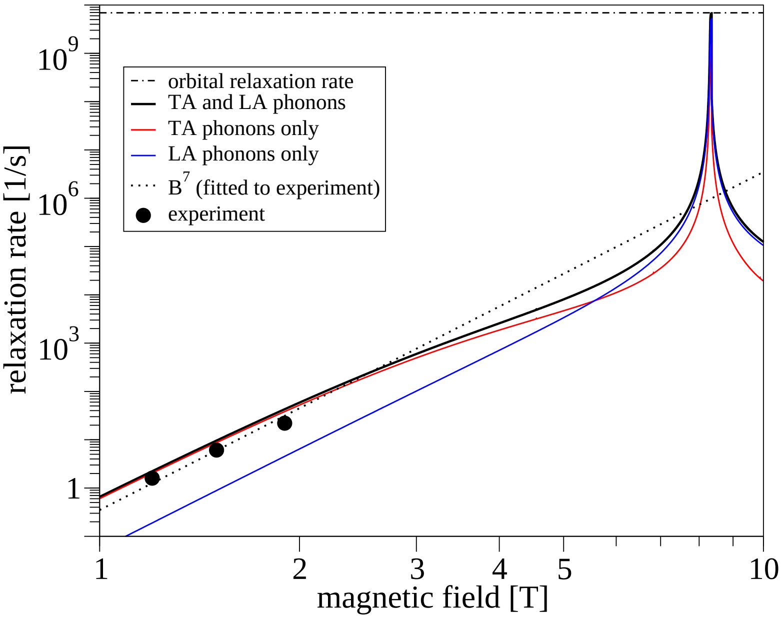

Figure 3.6.: Spin relaxation rates of a single electron in a silicon-based single quantum dot vs. in-plane field for $\gamma = 135°$. The total rate (solid black line) and its contributions of the transverse phonons (solid red line) and the longitudinal phonons (solid blue line) are shown. The spin hot spot at $B_{\|} \approx 8.3\,\mathrm{T}$ causes the spin relaxation rate to increase up to the orbital relaxation rate (dash-dotted line). The three dots give the experimental data of Ref. [192] fitted by a B^7 curve (dotted line).

Figure 3.6 displays the numerical results for the spin and orbital relaxation rates with $\gamma = 135°$. The transverse and longitudinal phonon contributions to the total spin relaxation rate are given to clarify their relative importance. We find that the rate for magnetic fields up to about 5 T essentially results from the transverse acoustic phonons. They do not depend on Ξ_{d} since the scalar product in $V^{\lambda}_{\mathbf{Q}}$, Eq. (3.10), vanishes. An important observation is the strong enhancement of the total spin relaxation rate at $B_{\|} \approx 8.3\,\mathrm{T}$. This is due to a spin hot spot that appears at the point at which the Zeeman splitting is equal to the level spacing of the Fock-Darwin states. The anticrossing induces a strong mixing of the spin states which boosts the spin relaxation. The spikes appear with equal height for any in-plane field orientation γ, as here the rate is given by the orbital relaxation rate [199], which is independent of γ.

In Fig. 3.6, we also plot the measured spin relaxation rate as reported in Ref. [192]. First, the observed power dependence corresponds to the coaction of spin-orbit interactions and deformation phonons [22, 23]. The energy conservation forbids a direct electron-nuclear spin flip-flop in finite magnetic fields. This process becomes allowed if accompanied by the emission of a phonon, yielding a relaxation rate proportional to B^5 [273]. Second, the order of magnitude agreement indicates that our choice of the spin-orbit strength is realistic, even though a direct fitting is not possible (the angle γ was not reported and the dot was not in a single-electron regime).

We now derive analytic formulas for the spin relaxation rate valid for weak in-plane magnetic fields. Treating the spin-orbit coupling perturbatively, we are able to evaluate Eq. (3.12) analytically. The total rate, $\Gamma_{\rm spin} = \Gamma^t_{\rm spin} + \Gamma^l_{\rm spin}$, is given by the contributions ($\lambda' = t, l$)

$$\Gamma^{\lambda'}_{\rm spin} = \mathcal{V}^2_{\lambda'} \frac{m^2 l_0^8}{24\pi\rho c^7_{\lambda'}\hbar^{10}} L^{-2} (g\mu_{\rm B} B_{\|})^7. \tag{3.22}$$

The energy parameter $\mathcal{V}^2_{\lambda'}$ reads as

$$\mathcal{V}^2_t = \frac{4}{35}\Xi^2_{\rm u}, \tag{3.23}$$

and

$$\mathcal{V}^2_l = \Xi^2_{\rm d} + \frac{2}{5}\Xi_{\rm d}\Xi_{\rm u} + \frac{3}{35}\Xi^2_{\rm u}, \tag{3.24}$$

for the transverse and longitudinal branches, respectively. The weak versus strong magnetic field limit is determined by the conditions $\mathcal{E}_\lambda \ll 1$ and $\mathcal{E}_\lambda \gg 1$ respectively, where $\mathcal{E}_\lambda = g\mu_{\rm B} B l_B/(\hbar c_\lambda)$ [199]. Here, the crossover $\mathcal{E}_\lambda = 1$ is at $B_{\|} = 1.4\,{\rm T}$ for transverse, and $B_{\|} = 2.6\,{\rm T}$ for longitudinal acoustic phonons. Comparing with the exact numerics, we find that the error of the value of Eq. (3.22) is less than 10% up to $B_{\|} = 0.8\,{\rm T}$ for transverse, and up to $B_{\|} = 2\,{\rm T}$ for longitudinal phonons. In any case, the error is less than 5% if $B_{\|} < 0.5\,{\rm T}$.

The integral in Eq. (3.12) can be done analytically only exceptionally, such as in the single dot case. Therefore, one often employs isotropically averaged deformation potentials to simplify the treatment [203, 204, 274]. This amounts to averaging $V^\lambda_{\mathbf{Q}}$, Eq. (3.10), over phonon directions distributed uniformly in three dimensions,

$$\left|V^\lambda_{\mathbf{Q}}\right|^2 \to \langle V^\lambda_{\mathbf{Q}}\rangle^2 \equiv \frac{1}{4\pi}\int |V_{\mathbf{Q}}|^2 {\rm d}\Omega. \tag{3.25}$$

Here it leads to Eq. (3.22) with

$$\mathcal{V}^2_{t,{\rm iso}} = 2\langle V^t_{\mathbf{Q}}\rangle^2 = \frac{4}{15}\Xi^2_{\rm u} \tag{3.26}$$

for the transverse, and

$$\mathcal{V}^2_{l,{\rm iso}} = \langle V^l_{\mathbf{Q}}\rangle^2 = \Xi^2_{\rm d} + \frac{2}{3}\Xi_{\rm d}\Xi_{\rm u} + \frac{1}{5}\Xi^2_{\rm u} \tag{3.27}$$

for the longitudinal contribution to the total rate. For our choice of parameters, we get $\langle V^t_{\mathbf{Q}}\rangle = 3.29\,{\rm eV}$ and $\langle V^l_{\mathbf{Q}}\rangle = 8.44\,{\rm eV}$. Comparing Eqs. (3.26) and (3.27) with Eqs. (3.23) and (3.24), we find that the averaging leads to rates which are 2.3 (transverse) and, for

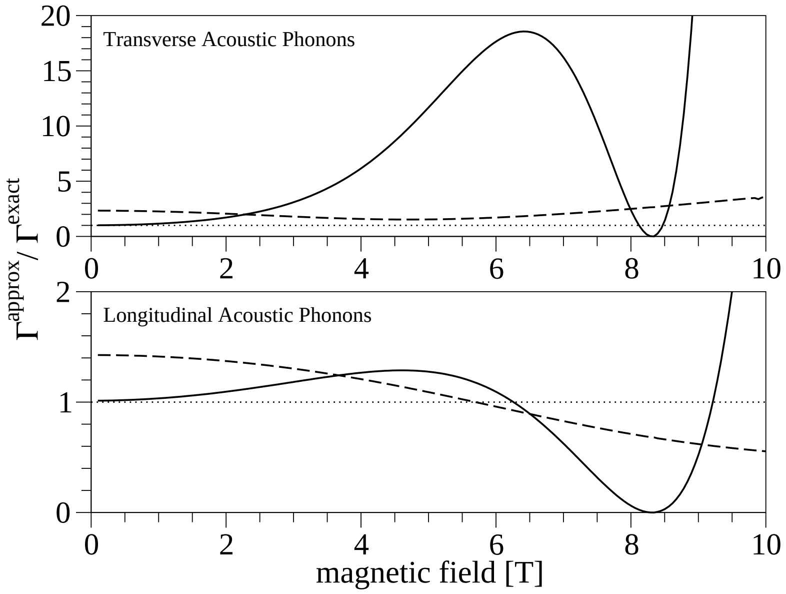

Figure 3.7.: Ratio of the relaxation rate of the approximations and the exact numerics vs. in-plane magnetic field. The low B-field limit, represented by Eqs. (3.23) and (3.24), is shown by the solid lines, and the numerically evaluated isotropic average approximation, Eq. (3.25), by the dashed lines. The contributions of the transverse and longitudinal phonons are given in the top and bottom panel, respectively. The magnetic field is in-plane and $\gamma = 135°$. The constant line at 1 (dotted) is a guide to the eye.

our parameters, 1.4 (longitudinal) times larger than the exact rates. Note that if we use instead of Eqs. (3.26) and (3.27) the averaged deformation potentials as reported in Ref. [204], we obtain relaxation rates that differ in the low-B-field limit from Eqs. (3.23) and (3.24) by a factor of 3.4 for the transverse, and 3.2 for the longitudinal contribution.

The isotropic average approximation becomes exact if the matrix element $|M_{ij}|$ is independent of the phonon direction. However, this directional invariance is not satisfied in lateral dots, which are strongly anisotropic in the perpendicular versus the in-plane direction. To assess the quality of the approximations, we compare the corresponding relaxation rates with the exact numerical result in Fig. 3.7 for magnetic fields up to 10 T. Our measure is the ratio between the rate of the approximation and of the numerics, which we plot for the transverse and longitudinal contributions separately. The parameters in Fig. 3.7 are identical to Fig. 3.6. We find that the analytical results (solid lines in Fig. 3.7) deviate significantly from numerics for fields beyond the low B-field limit. The especially large discrepancy at around 8.3 T, where the ratio is close to zero, stems from the fact that the analytic approximations assume no level crossings of the initial state. Thus, they account for neither spin hot spots, nor the transition into excited states. Equations (3.26) and (3.27) result in curves parallel to Eqs. (3.23) and (3.24), but shifted by the discrepancy factors 2.3 and 1.4 for the transverse and

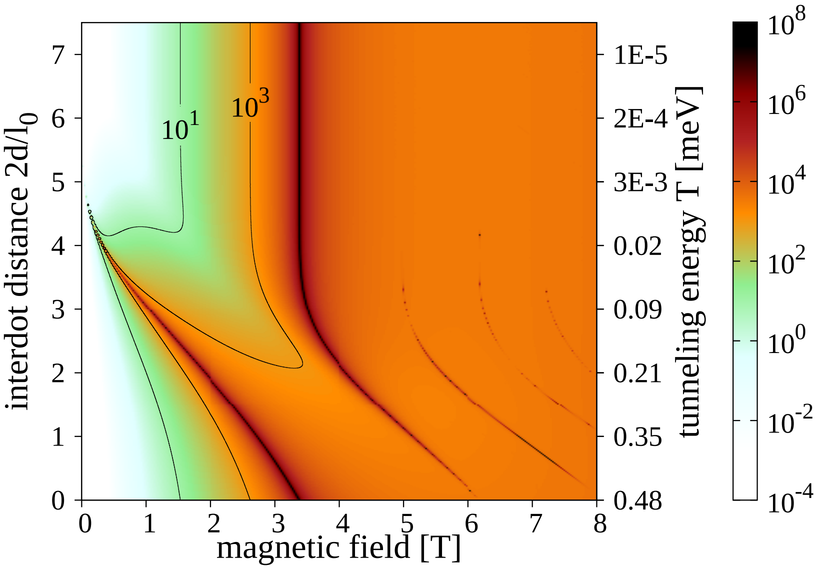

Figure 3.8.: Calculated spin relaxation rate in a silicon double quantum dot as functions of perpendicular magnetic field and interdot distance. The rate is given in inverse seconds by the color with the scale on the right. The y-axis is calibrated in interdot distance (left) and tunneling energy at $B = 0$ (right).

longitudinal contributions (not shown). Numerical evaluation of the spin relaxation rates via Eq. (3.12) using the average of Eq. (3.25) leads to a discrepancy represented by the dashed line in Fig. 3.7. We find that even in highly anisotropic (2D) lateral dots, the discrepancy factor is only of the order of 1. It is therefore expected to be legitimate to use the isotropic averaging also for more complicated dot geometries, such as the double dot, or a biased dot, where it can lead to significant simplifications.

Double Quantum Dots We now move to a double dot case, where we take $2d$ as a variable parameter, noting that it could stand for either the actual separation between two dots, or a gate-tunable coupling between dots of fixed distance. From the experimental point of view, it is more convenient to characterize a double quantum dot via the tunneling energy. We plot our results with respect to the interdot distance and give also the corresponding tunneling energy at zero magnetic field computed numerically (Fig. 3.4, dotted line).

The spin relaxation rate in a double quantum dot as a function of both the interdot distance in units of l_0 and the perpendicular magnetic field is shown in Fig. 3.8. We find that the plotted area is dominated by the spikes, which come from spin hot spots, and that there are no easy passages, that is there is no possibility for a fixed magnetic field to change the interdot distance from zero to infinite without passing through any of these peaks. For small fields, here $B_z < 3\,\mathrm{T}$, we have only one relevant spike, which

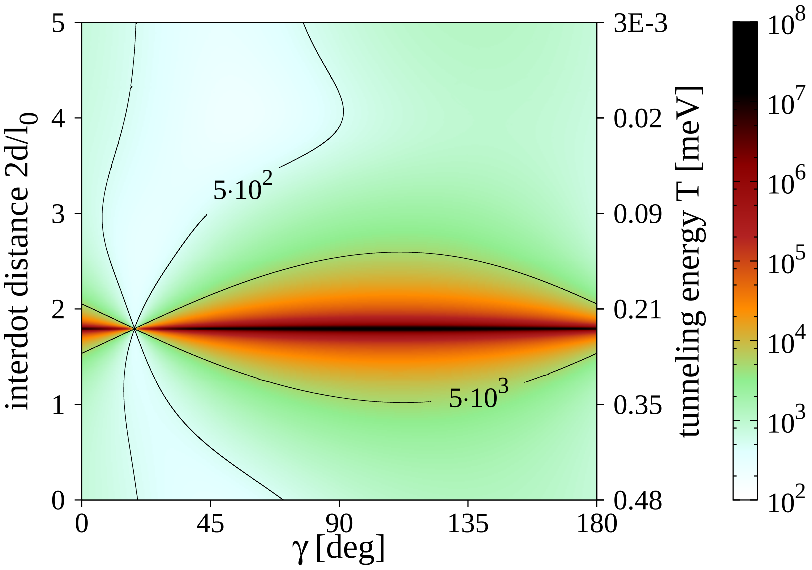

Figure 3.9.: Calculated spin relaxation rate in a silicon double quantum dot as a function of the interdot distance and the orientation of the in-plane magnetic field ($B_{\|} = 4\,\mathrm{T}$). The rate is given in inverse seconds by color with the scale on the right. The y-axis is calibrated in interdot distance (left) and tunneling energy at $B = 0$ (right). The dots main axis is along $[100]$.

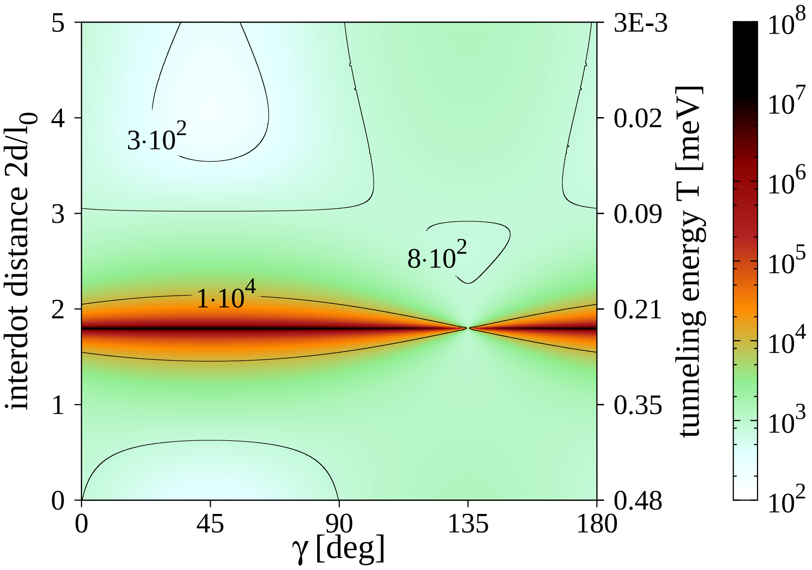

Figure 3.10.: Calculated spin relaxation rate in a silicon double quantum dot as a function of the interdot distance and the orientation of the in-plane magnetic field ($B_{\|} = 4\,\mathrm{T}$). The rate is given in inverse seconds by color with the scale on the right. The y-axis is calibrated in interdot distance (left) and tunneling energy at $B = 0$ (right). The dots main axis is along $[110]$.

comes from the anticrossing of $\Gamma_{\mathrm{S}}^{\uparrow}$ and $\Gamma_{\mathrm{A}}^{\downarrow}$ (see Fig. 3.5). For larger magnetic fields, crossings with higher orbital states occur which may, but need not, lead to spin hot spots, depending on the symmetry of the crossing states.

If the field is applied in the plane, the spin relaxation depends on the orientation of the magnetic field with respect to the crystallographic axes because of the interplay between Bychkov-Rashba and generalized Dresselhaus spin-orbit couplings. Once we rotate the coordinate system by δ around $\hat{z}$, the effective Zeeman field, Eq. (3.20), reads as [199, 238]

$$\begin{aligned}\tilde{B}_z^{\mathrm{eff}} =- \quad & B_{\|}\tilde{x}\left[l_{\mathrm{br}}^{-1}\cos(\gamma-\delta) - l_{\mathrm{d}}^{-1}\sin(\gamma+\delta)\right] + \\ + \quad & B_{\|}\tilde{y}\left[l_{\mathrm{br}}^{-1}\sin(\gamma-\delta) - l_{\mathrm{d}}^{-1}\cos(\gamma+\delta)\right] \ ,\end{aligned} \tag{3.28}$$

where the tilted axes are such that $\tilde{x}$ is parallel to $\mathbf{d}$. Since the first excited orbital state Γ_{A} transforms like $\tilde{x}$, only the first term in Eq. (3.28) can lead to spin hot spots for moderate magnetic fields in the intermediate regime. As an example, we plot in Fig. 3.9 the spin relaxation rate in a double dot aligned along [100] ($\delta = 0°$) in a magnetic field $B_{\|} = 4\,\mathrm{T}$ varying the orientation γ and the interdot distance. A sharp peak occurs at $2d/l_0 = 1.8$ but is intermittent at $\gamma_{\mathrm{e}} = 18°$ where the first term of Eq. (3.28) vanishes. Note that this angle, defining the easy passage, depends on the spin-orbit coupling lengths and is thus sample and setup dependent. An experimental determination of the easy passage angle would provide information about the relative spin-orbit coupling strengths via the relation $\tan(\gamma_{\mathrm{e}}) = \alpha/\beta$.

Equation (3.28) shows that the easy passage depends also on the double dot orientation with respect to the crystallographic axes. We note that for a double dot with the main axis along the [110] direction ($\delta = 45°$), the corresponding field orientation of the easy passage is universal ($\gamma_{\mathrm{e}} = 135°$), i.e. it is independent of the spin-orbit coupling strengths. We plot the spin relaxation rates for this case in Fig. 3.10 for completeness.

3.4. Summary

In Chap. 3, we investigated the energy spectrum and the spin relaxation of a single-electron (double) quantum dot using the theoretical model introduced in Sec. 3.1. For the analysis, we focused on dots defined in a laterally gated Si/SiGe heterostructure (Sec. 3.3). An analog discussion for the GaAs-based dot was skipped because of the thorough investigations of others during the last few years (see e.g. Stano et. al. [199, 238]). We commented on these works in Sec. 3.2 for completeness. In the present work, we consider the spin relaxation to be an inelastic transition in which the spin-flip is enabled by the presence of the spin-orbit interactions, while the energy difference between the initial and final state, arising from the applied magnetic field, is taken away by an acoustic phonon. We study relaxation rates while varying the interdot coupling from strong (a single dot regime) to negligible (a double dot regime), as well as changing the strength and orientation (in-plane or perpendicular) of the magnetic field.

We adopt the single-valley, the effective-mass, and the two-dimensional approximation, within which our results are numerically exact. Whereas the latter two are known to be well justified for lateral quantum dots, the single-valley approximation breaks down once the valley splitting drops below the orbital energy scale, $\sim$meV, and additional states appear in the lowest part of the dot spectrum. Concerning the spin relaxation, however, these states are irrelevant as the matrix elements for the phonon-induced intervalley transitions are greatly suppressed. This is so because long wavelength phonons, which arise due to the small transition energy ($q \lesssim 0.1\,\mathrm{nm}^{-1}$ at $3\,\mathrm{T}$), are ineffective in coupling states with disparate Bloch wave functions ($k_v \approx 10\,\mathrm{nm}^{-1}$); see Eq. (2) in Ref. [166] and the discussion therein.

We find that the spin relaxation in Si dots is roughly comparable to that in GaAs, although it bears certain differences. Namely, in the single dot the relaxation rate in Si is proportional to B^7, being due to the deformation phonon potential, in contrast to the B^5 dependence in piezoelectric GaAs. We compare our theory with experimental data, which confirm the magnetic field power dependence and show that the spin-orbit strengths of the order of $0.1\,\mathrm{meV\,Å}$ are to be expected in Si/SiGe quantum dots. We also derive an analytical expression for the relaxation rate treating the spin-orbit interactions in the lowest order. We find it to be an excellent approximation to the numerics up to magnetic fields of 1-2 T. A further simplification, the isotropic averaging, makes the analytical result to differ from the exact one by a factor of the order of 1.

We show that in the double dot the relaxation rate is a much more complicated function of the magnetic field and the interdot coupling, the two parameters most directly controllable experimentally. This is due to the fact that the rate is strongly influenced by spin hot spots, which occur at much lower magnetic fields in the double dot compared to the single dot. The anisotropy of the spin-orbit interactions leads to the rates dependent on the magnetic field direction with respect to the crystallographic axes. In a double dot, where the rotational symmetry of the potential is broken but the reflection symmetry is preserved, this anisotropy results in the appearance of easy passages—special directions of the external magnetic field which ensure a strong suppression of the relaxation rate. From these directions the ratio of the spin-orbit strengths can be found. Compared to GaAs, the position of the easy passage in Si relates directly to the linear spin-orbit strengths without being influenced by the spin-orbit interaction cubic-in-momenta.

Finally, we observe that, compared to GaAs, the spin relaxation rates in Si are typically two orders of magnitude smaller, as a result of the absence of the piezoelectric phonon interaction and generally weaker spin-orbit interactions.

CHAPTER 4

Two-Electron Quantum Dots

In the previous chapter we discussed the energy spectrum and spin relaxation of a double dot charged by a single electron. In this chapter, we add another electron to the system, and consider the energy spectrum and spin relaxation of the two-electron single and double quantum dots. A complication is given by the Coulomb interaction. It is dominant in typical dot configurations, which raises the numerical demands [275]. Without spin-orbit coupling, the spin state is a singlet or triplet. A spin relaxation channel is defined by the transition from such a singlet or triplet to a different spin state with lower energy. The total spin relaxation is given by the sum of all channels to the energetically lower-lying states. In the two-electron double dot, a thorough analysis of the spin relaxation is very challenging because many parameters need to be considered simultaneously: the magnitude and orientation of the magnetic field, the orientation of the dot with respect to the crystallographic axes, the strength of the interdot coupling (parametrized by either tunneling or exchange energy) and the bias applied across the double dot. Here we cover all these parameters, providing specific relevant predictions for experimental setups.

This chapter is organized as follows. In Sec. 4.1 we extend our model, which was initially introduced in Sec. 3.1, to cope with the second electron. We also include an external electric field, the bias, which accounts for detuning of the double dot, and the nuclear bath, which serves as an additional source of perturbation to enable the spin relaxation. Then we look at the energy spectra and spin relaxation. A GaAs-based double dot is considered in Sec. 4.2. We unveil that the nuclear spins can dominate the spin relaxation for unpolarized triplets even at high magnetic fields, contrary to common belief. We also find that the anisotropy of relaxation rates can be manipulated by detuning. The magnetic field orientation for a minimal rate becomes the one for maximum rate, and vice versa. We discuss silicon in Sec. 4.3. It shows the same anisotropic switch of the axis of prolonged spin lifetime with varying detuning. But the conditions for a possibly hyperfine-dominated relaxation (originating from the abundance of ^{29}Si) are much more stringent than in GaAs. This means that for experimentally relevant regimes, the spin-orbit coupling, although weak, is the dominant contribution, yielding anisotropic relaxation rates in silicon also for the unpolarized triplet. A summary of this chapter is given in Sec. 4.4.

4.1. Theoretical Model

The model for the two-electron dot is the natural extension of the model used for the single-electron dot, presented in Sec. 3.1. Here we discuss only the extensions to that model while the rest of Sec. 3.1 remains valid. For the analysis of two-electron dots, we also take the hyperfine coupling into account. Therefore, we introduce the nuclear spins in the following and show how they contribute to the relaxation.

The Hamiltonian of the two-electron system reads as

$$H = \sum_{i=1,2} \left(T_i + V_i + H_{\mathrm{Z},i} + H_{\mathrm{so},i} + V_{\mathrm{E},i} + H_{\mathrm{nuc},i} \right) + H_{\mathrm{C}}, \tag{4.1}$$

where i labels the electrons. The four known single-electron terms are the kinetic energy T, the potential energy V, the Zeeman energy H_{Z}, and the spin-orbit coupling H_{so}, given by Eqs. (3.2), (3.3), (3.4), and (3.5), respectively. The new terms in Eq. (4.1), V_{E}, H_{nuc}, and H_{C}, account for an in-plane electric field, the hyperfine coupling, and the Coulomb interaction, respectively. These terms are introduced in more detail in the following.

In addition to the static confinement potential V, we consider in this chapter also a static electric field $\mathbf{E}$ applied along the dot main axis $\mathbf{d}$, where

$$V_{\mathrm{E}} = e\mathbf{E} \cdot \mathbf{r}. \tag{4.2}$$

Turning on $\mathbf{E}$ shifts the potential minima of V relative to each other. The detuning energy ϵ is defined in this work as the energy difference between both minima, given by $\epsilon = 2eEd$. Note that detuning is the crucial parameter in most experiments of qubit manipulations [96].

The nuclear spins of GaAs and ^{29}Si predominantly couple through the Fermi contact interaction [131, 276, 277],

$$H_{\mathrm{nuc}} = \beta \sum_n \mathbf{I}_n \cdot \boldsymbol{\sigma}\, \delta(\mathbf{R} - \mathbf{R}_n), \tag{4.3}$$

where β is a constant, $\mathbf{I}_n$ is the spin of the n-th nucleus at the position $\mathbf{R}_n$, and $\mathbf{R} = (\mathbf{r}, z)$ is the three-dimensional electron position operator. Here we need to consider the finite extension of the wave function perpendicular to the heterostructure interface, which we assume to be fixed to the ground state of a hard-wall confinement of width w. The effective width [278] is given by

$$h_z = \left[\int \mathrm{d}z \, |\psi_0(z)|^4 \right]^{-1}. \tag{4.4}$$

For the quantum well, it is $h_z = 2w/3$. In the numerics, we treat the nuclear spins by averaging over unpolarized random ensembles. See Appendix A for details.

The only many-particle operator in the Hamiltonian, Eq. (4.1), and therefore responsible for the coupling of the two electrons, is the Coulomb interaction. It reads as

$$H_{\mathrm{C}} = \frac{e^2}{4\pi\varepsilon\left|\mathbf{r}_1 - \mathbf{r}_2\right|}, \tag{4.5}$$

where ε is the material dielectric constant.

The relaxation of a singlet or triplet in our model is mediated by acoustic phonons, just as for the single electron case. However, whereas in the previous chapter only spin-orbit interactions allow for the spin-flip by mixing the spin states, here we consider both spin-orbit and hyperfine coupling as a perturbation. The electron-phonon coupling, H_{ep}, is given by Eq.(3.9), where the factor $V_{\mathbf{Q},\lambda}$ for the deformation and piezoelectric potentials is given by Eqs. (3.10) and (3.11), respectively. The relaxation rate is defined as the sum of the individual transition rates to all lower-lying states. Each individual rate is evaluated for both the deformation and the piezoelectric potential via Eq. (3.12). Note that in the two-electron case, the matrix element in Eq. (3.12) reads as $M_{ij} = \langle i|\mathrm{e}^{\mathrm{i}\mathbf{Q}\cdot(\mathbf{R}_1+\mathbf{R}_2)}|j\rangle$, where $\mathbf{R}_i$ is the position operator of the i-th electron, and $|i\rangle$ and $|j\rangle$ are now two-electron wave functions. In the following, we focus on the singlet (S) and the three triplets (T_+, T_0, T_-) at the bottom of the energy spectrum.

4.2. Gallium Arsenide

In this section we present quantitative results of the energy spectrum and the spin relaxation of GaAs-based two-electron double quantum dots.[1] We perform our calculations using typical parameters of a lateral dot [112], with the effective mass $m = 0.067 m_e$, the effective Landé factor $g = -0.44$, the confinement energy $E_0 = 1.0\,\text{meV}$, corresponding to $l_0 = 34\,\text{nm}$, and the material dielectric constant $\epsilon = 12.9\epsilon_0$. For the spin-orbit and hyperfine coupling strengths, we take $l_{\text{br}} = 2.42\,\mu\text{m}$, $l_{\text{d}} = 0.63\,\mu\text{m}$, $\gamma_c = 27.5\,\text{eV}\,\text{Å}^3$, and $\beta = 1\,\mu\text{eV}\,\text{nm}^3$ [238, 276]. The nuclei of both gallium and arsenic have $I = 3/2$. In the following, we define the double dot orientation to be $\mathbf{d} \,||\, [110]$. The energy spectrum of the hereby obtained system is discussed in Sec. 4.2.1. For the evaluation of the spin relaxation, presented in Sec. 4.2.2, we use $c_t = 2480\,\text{m/s}$ and $c_l = 5290\,\text{m/s}$ for the sound velocities of transverse and longitudinal phonons, $\rho = 5300\,\text{kg}/m^3$ for the mass density, and $\sigma_e = 7\,\text{eV}$ and $eh_{14} = 1.4 \times 10^9\,\text{eV/m}$ for the deformation and piezoelectric constant, respectively [156].

Our results are obtained numerically, as an exact analytical solution is not available. The numerical algorithm first solves the related single-electron system with the method of finite differences, analogous to Chap. 3, and generates Slater determinants [279] afterwards. They are used as the two-electron basis for the configuration interaction method. More details on the numerical scheme can be found in Appendix A. In the following, the discretization grid is typically 135×135, and the two-electron basis consists of 1156 Slater determinants, generated by 34 single-electron orbital states. Hereby, we ensure a relative error for energies below 10^{-5}.

4.2.1. Energy Spectrum

The energy spectrum of two-electron laterally coupled double quantum dots with focus on the role of spin-orbit coupling, which leads to an anisotropic exchange energy J in finite external magnetic fields, has been thoroughly investigated by Baruffa et. al. [280, 281]. The authors also introduce an effective Hamiltonian for the four-dimensional subspace, given by the singlet and the three triplets lowest in energy. Here we do not repeat those results. Instead, we present the numerically calculated energy spectra that we need in order to understand the spin relaxation in unbiased and biased double dots, including the role of hyperfine coupling, which we discuss in Sec. 4.2.2.

Unbiased Double Dot The coupling between the dots is parameterized in analogy to Chap. 3 by the (dimensionless) interdot distance $2d/l_0$, which translates for a two-electron dot into an exponentially sensitive S-T_0 exchange splitting J. Electrical control over J, necessary e.g. to induce the $\sqrt{\text{SWAP}}$ gate [100], allows for a fast switching

---

[1] Parts of Sec. 4.2 are based on Raith et. al., *Theory of Spin Relaxation in Two-Electron Lateral Coupled Quantum Dots*, Phys. Rev. Lett. 108, 246602 (2012) [153].

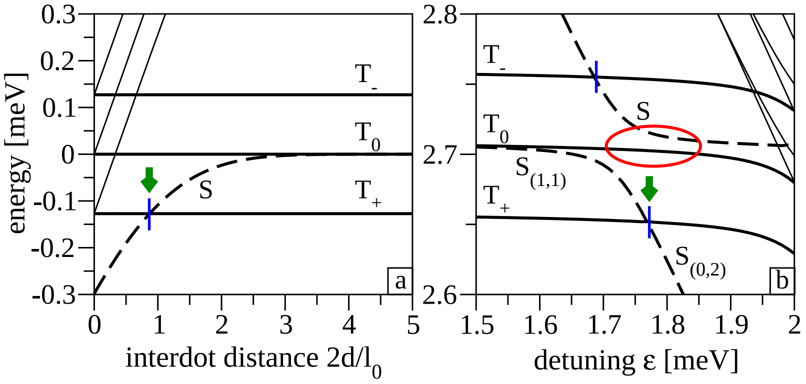

Figure 4.1.: Calculated energies of the lowest states for (a) variable interdot coupling (at $B = 5\,\mathrm{T}$), and (b) detuning (at $B = 2\,\mathrm{T}$, and $2d/l_0 = 4.35$, i.e. $T = 10\,\mu\mathrm{eV}$). Singlet states are given by dashed, triplets by solid lines. The blue strokes mark singlet-triplet anticrossings. In (a), the energy of T_0 is subtracted, and in (b), the quadratic trend in E is subtracted. The green arrows denote points of exact compensation and the red oval in (b) shows where nuclear spins dominate the T_0 relaxation (see Sec. 4.2.2).

between the strong and weak coupling regime, corresponding to the exchange splitting being larger and smaller than the Zeeman energy, respectively. During this switching, the ground state changes at an S-T_+ anticrossing. The energy spectrum of an unbiased double dot as a function of the interdot coupling is plotted in Fig. 4.1(a).

Biased Double Dot Experimentally most relevant are weakly coupled double dots with an applied in-plane electric field that regulates the detuning, Eq. (4.2). In this regime, due to the large potential barrier between the dots, the states can be labeled by (n, m), where n and m give the number of electrons trapped in the left and right dot, respectively. Here, in the case of two-electron double dots, the ground state of the system is a (1,1) configuration for zero, and (2,0) or (0,2) for large detunings. Without magnetic field, the ground state is always the singlet [281]. The energy spectrum of a biased double dot in a finite magnetic field as a function of the detuning is given in Fig. 4.1(b). The pronounced singlet-singlet anticrossing presents the crossover from the low to large detuning regime. This anticrossing is a key handle in spin measurement and manipulation [112]. We also find the S-$T_\pm$ anticrossings, which are exploited for nuclear-spin pumping [154, 282].

4.2.2. Spin Relaxation

Unbiased Double Dot In the first part of this section, the spin relaxation of the singlet (S) and the three triplets (T_+, T_0, T_-) of an unbiased dot is investigated. The corresponding energy spectrum is given in Fig. 4.1(a). We plot the relaxation rate as a function of interdot coupling in Fig. 4.2. Panel a) shows the relaxation of the first

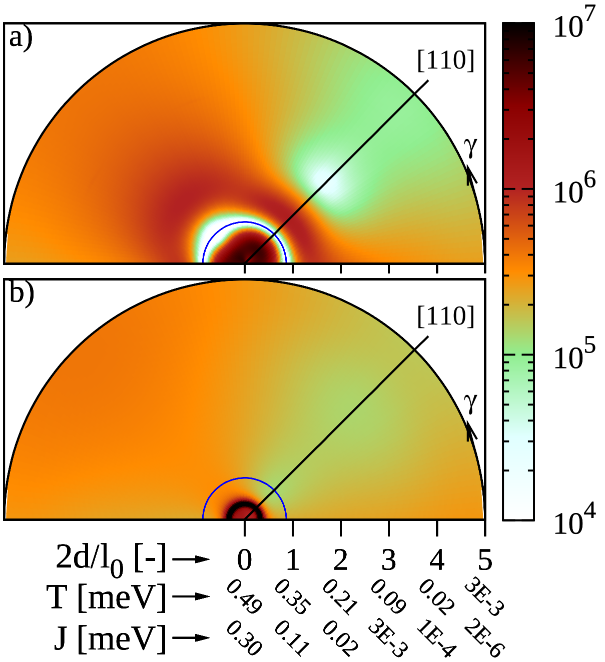

Figure 4.2: Calculated relaxation rates of (a) the first excited state [S or T_+, see Fig. 4.1(a)] and (b) the triplet T_0 as a function of the in-plane magnetic field orientation γ (angle) and the interdot distance $2d/l_0$ (radius of the polar plot), for a double dot at $B = 5\,\mathrm{T}$. The x and y axes correspond to crystallographic axes $[100]$ and $[010]$, respectively. The dot orientation $\mathbf{d} \parallel [110]$ is marked by a line. The blue half circles indicate the S-T_+ anticrossing, also marked on Fig. 4.1(a). The x axis is converted to the tunneling energy T and the exchange J, in addition to $2d/l_0$. The rate is given in inverse seconds by the color scale. The system obeys C_{2v} symmetry, so point reflection would complete the graphs.

excited state [S or T_+, see Fig. 4.1(a)]. First to note is the strong relaxation suppression at the S-T_+ anticrossing as the transferred energy becomes very small. Remarkably, the anticrossing does not influence the rate of T_0, plotted in panel b), at all. Even though the dominant channel, $T_0 \to T_+$, is strongly suppressed here, its reduction is exactly compensated by the elsewhere negligible $T_0 \to S$ channel. Note that the peak close to $d = 0$ is due to an anticrossing with a higher excited state. The origin of this exact compensation and its condition for occurrence is the following:

In general, the relaxation rate channels significantly change at spectral anticrossings because of the strong mixing of states. We consider the total relaxation rate by summing over the individual relaxation channels of transitions into all lower lying states. Therefore, a change in one relaxation channel may be compensated by another channel, such that the total relaxation rate is smooth (no peak or dip) across the anticrossing. This generally happens if a state relaxes *into* a quasi-degenerate subspace of anticrossing states. For the given double dot, the exact compensation occurs at the anticrossings which are marked by a green arrow in Fig. 4.1. We exemplify the exact compensation by considering the relaxation of T_0 (state i) right at the interdot distance where the S-T_+ anticrossing occurs [blue stroke in Fig. 4.1(a)]. The total relaxation of T_0 is calculated from the individual transition rates Γ_{ij}, Eq. (3.12), using

$$\Gamma_i = \sum_j \Gamma_{ij}, \tag{4.6}$$

where the sum includes the two quasi-degenerate states $j_1 = T_+$ and $j_2 = S$. The exact compensation arises if one can approximate the delta functions in Γ_{ij_1} and Γ_{ij_2} to be equal, which is the case if $E_{ij_1} \approx E_{ij_2} \approx \Delta E$ holds for the transition energies. Indeed, the relaxation rate can then be written as

$$\Gamma_i = \frac{\pi}{\rho V} \sum_{\mathbf{Q},\lambda} \frac{Q}{c_\lambda} |V_{\mathbf{Q},\lambda}|^2 \langle i|MPM^\dagger|i\rangle \delta(\Delta E - E_{\mathbf{Q}}^\lambda), \tag{4.7}$$

where $P_j = \sum_j |j\rangle\langle j|$ is the projector on the quasi-degenerate subspace, which is not influenced by mixing of the basis states j. Since the delta function in Eq. (3.12) fixes the phonon energy $E_{\mathbf{Q}}^\lambda$ to the value of the transition energy, the approximation Eq. (4.7) can only be valid if both factors under the integral in Eq. (3.12), the phonon potential as well as the electron overlap integral M, are not too different for the two transition energies E_{ij_1} and E_{ij_2}. The phonon potential scales as a certain power (albeit different for piezoelectric and deformation potential) in the phonon wave vector, which translates into the condition

$$E_{\text{acr}} \ll \Delta E, \tag{4.8}$$

where $E_{\text{acr}} = |E_{ij_1} - E_{ij_2}|$ denotes the energy width of the subspace (the anticrossing gap). On the other hand, the natural scale for the electron wave function is the confinement length l_0, and the overlap M is approximately identical for both transition energies as long as

$$E_{\text{acr}} \ll \hbar c_\lambda / l_0 \tag{4.9}$$

is valid. Loosely speaking, Eq. (4.9) means that if we relate the difference of the two transition energies to a change in phonon wavelength, it is negligible compared to the dot size. Both Eq. (4.8) and Eq. (4.9) together give the condition for the exact compensation, namely

$$E_{\text{acr}} \ll \min\{\Delta E, \hbar c_\lambda / l_0\}. \tag{4.10}$$

The condition states that the energy width E_{acr} is too small to be resolved by either phonons with energy ΔE or the electron wave function scale l_0. Then, the relaxation proceeds into the subspace rather than into its constituent states, so that any mixing of the states within the subspace is irrelevant.

In our case, we obtain $\Delta E = 125\,\mu$eV and $\hbar c_t / l_0 = 48\,\mu$eV for the dominant piezoelectric phonons, while E_{acr} is just $7\,\mu$eV, so that the condition Eq. (4.10) is well satisfied. To illustrate the exact compensation, we plot in Fig. 4.3 the individual relaxation channels as a function of interdot distance. The parameters are chosen the same as in Fig. 4.2. We find the exact compensation at the S-T_+ anticrossing for the T_0 and the T_- relaxation. In the case of the unpolarized triplet, the dip of the $T_0 \to T_+$ channel is compensated by a peak of the $T_0 \to S$ channel. For T_-, the dip and peak occur in the $T_- \to S$ and $T_- \to T_+$ channels, respectively. Note that if the in-plane magnetic field is perpendicular to the dot main axis $\mathbf{d}$ (lower panel in Fig. 4.3), the relaxation channels

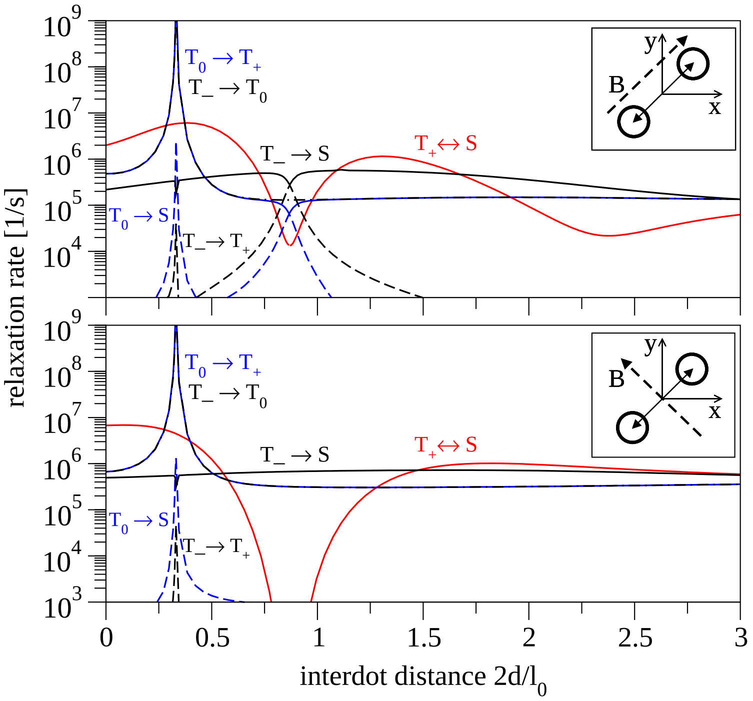

Figure 4.3.: Calculated channel resolved relaxation rates vs. interdot distance in units of l_0 for both parallel (top) and perpendicular (bottom) to **d** in-plane magnetic field orientation ($B = 5\,\mathrm{T}$, zero detuning). The relaxation channels of T_0 and T_- are in blue and black color, respectively. The relaxation rate of the first excited state is red.

for T_- and T_0 do not vary at all, as the S-T_+ anticrossing gap vanishes, $E_{\mathrm{acr}} = 0$, and the exact compensation is trivial.

Besides the exact compensation, Fig. 4.2 shows another interesting feature. It displays the anisotropy of the relaxation, which reflects the anisotropy of the spin-orbit fields. In the weak coupling regime, the relaxation rates are minimal if the magnetic field orientation is parallel to the dot main axis, which results in an isle of strongly prolonged spin lifetimes. Note that this is in contrast to the biased dot (see below), and to the single-electron case, where the minimal in-plane magnetic field direction, the easy passage, of a **d** ∥ [110] double dot is perpendicular to **d** [238, 259]. The switch can be understood from the effective, spin-orbit induced, magnetic field [238] if written using the coordinates along the dot axes $x_d, y_d = (y \pm x)/\sqrt{2}$,

$$\mathbf{B}_{\mathrm{so}} = \mathbf{B} \times \{y_d(l_d^{-1} + l_{br}^{-1})[110] + x_d(l_d^{-1} - l_{br}^{-1})[\bar{1}10]\}. \tag{4.11}$$

A minimal $\mathbf{B}_{\mathrm{so}}$ with respect to the orientation of the magnetic field $\mathbf{B}$ gives a minimal relaxation rate. At the anticrossing, the mixing due to x_d is by far the most dominant, so the minimum appears with $\mathbf{B}$ along $[\bar{1}10]$. This x_d dominance will be the case for

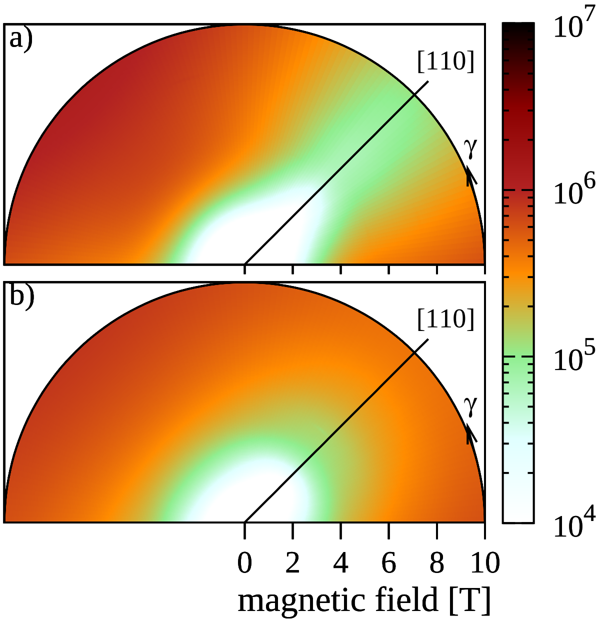

Figure 4.4: Calculated relaxation rates of (a) the first excited state and (b) the triplet T_0 as a function of the in-plane magnetic field orientation γ (angle) and the magnetic field magnitude (radius of the polar plot), for a double dot with $2d/l_0 = 2.88$ ($T = 0.1$ meV). The layout with respect to the crystallographic axes is the same as in Fig. 4.2. The rate is given in inverse seconds by the color scale.

a biased dot, too. On the other hand, in a single dot x_d and y_d induce comparable mixing, and $\mathbf{B}_{so}$ becomes minimal if the larger term (the one with y_d) is eliminated. A weakly coupled unbiased dot is in this respect similar to a single dot as the two-electron transitions can be understood as flips of a particular electron located in a single dot. Since the direction of the rate minimum switches upon changing d, the system does not show an easy passage, that is a low relaxation rate from weak to strong coupling regime.

We plot the magnetic field dependence for a weakly coupled unbiased double dot in Fig. 4.4 and observe similar behavior as in Fig. 4.2. The relaxation rate is minimal if $\mathbf{B} \,||\, \mathbf{d}$ throughout the shown parametric region. This is because the anticrossing and the related directional switch happens here at so small magnetic field that it is not visible at the figure resolution. For completeness, we note that the T_- relaxation behavior is very similar to the one for T_0 on both Figs. 4.2 and 4.4, and we do not show it.

Biased Double Dot In the second part, we look at the spin relaxation of a detuned double dot with the energy spectrum as plotted in Fig. 4.1(b). The spin relaxation of the first excited state as a function of detuning is presented in Fig. 4.5. We find that the relaxation rates are independent of detuning unless close to the singlet-singlet anticrossing, which holds also for the relaxation of T_0 and T_- (not shown). For this reason, we focus on the vicinity of the singlet-singlet anticrossing, defined by the scope of Fig. 4.1(b) (that is for detuning energies from 1.5 meV to 2.0 meV), in our further analysis.

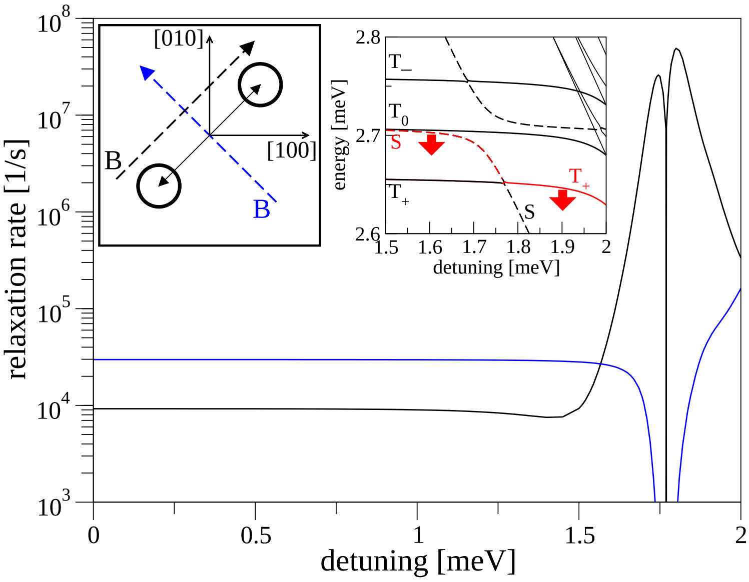

Figure 4.5.: Calculated spin relaxation of the first excited state (S or T_+, see inset) as a function of detuning energy for a double dot with $2d/l_0 = 4.35$ ($T = 10\,\mu$eV), chosen along Ref. [112], and $B = 2\,$T. The in-plane magnetic field is oriented parallel (black line) and perpendicular (blue line) to the dot main axis $\mathbf{d}$ (see drawing). The inset shows the energy spectrum as given in Fig. 4.1(b).

The influence of detuning and an in-plane magnetic field on the relaxation rate is shown in Fig. 4.6. At the singlet-triplet anticrossings, we observe several interesting features. First, the relaxation rate of the first excited state dips at the S-T_+ anticrossing (see also Fig. 4.5). The reason is that due to the small transition energy, and therefore the low phonon density of states at that energy, the relaxation is inhibited. Second, the T_- rate strongly peaks at the S-T_- anticrossing. This is a demonstration of the dominant matrix element M in Eq. (3.12). Third, there are no other manifestations of the S-$T_\pm$ anticrossings, a fact due to the exact compensation already mentioned before. The anisotropy features of this geometry are striking. In the given range of detuning energies, states except T_0 exhibit a very distinctive easy passage for a magnetic field along $[\bar{1}10]$, where the relaxation is up to three orders of magnitude smaller than with $\mathbf{B}$ along [110]. On the other hand, the rates become minimal for a magnetic field along [110] for very small and very large detunings. This directional switch is beyond the scope of Fig. 4.6, but can be observed in Fig. 4.5 for the first excited state. In general, the rates increase at detunings $\gtrsim 2\,$meV, because of spectral crossings with excited triplets [see Fig. 4.1(b)], which sets the boundary for a regime which is normally avoided in experiments. Double dots, with their spectral idiosyncrasies, are a unique system to observe a giant amplification of the spin-orbit anisotropies by a physical observable with bias control.

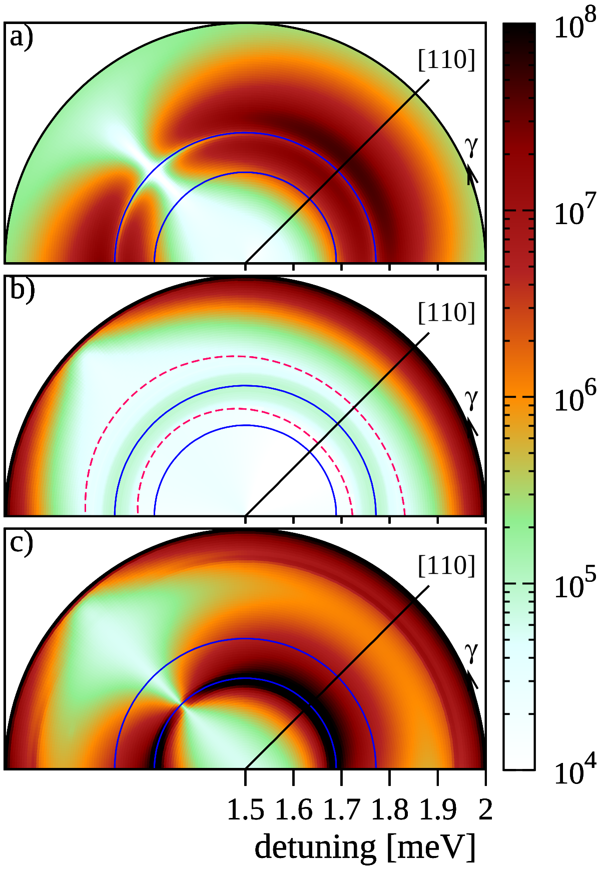

Figure 4.6.: Calculated relaxation rates of (a) the first excited state, (b) T_0, and (c) T_- as a function of the in-plane magnetic field orientation γ (angle) and detuning energy (radius of the polar plot) for a weakly coupled double dot. The dot parameters are identical to Fig. 4.5. The layout with respect to the crystallographic axes is the same as in Fig. 4.2. The rate is given in inverse seconds by the color scale. The blue lines indicate the singlet-triplet anticrossings, in line with the marks in Fig. 4.1(b). The dashed red lines in panel b) confine the area where hyperfine coupling dominates.

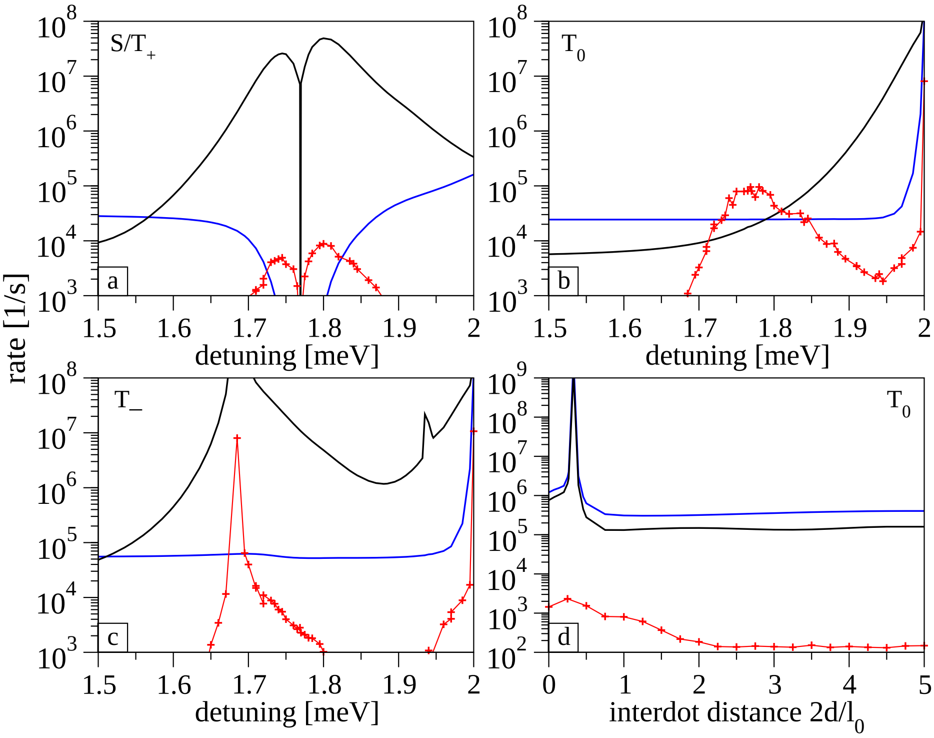

Figure 4.7.: Calculated spin-orbit induced relaxation rates for an in-plane magnetic field orientation parallel (black curves) and perpendicular (blue curves) to the dot main axis $\mathbf{d}$. The red curves show the hyperfine-induced spin relaxation. (a)-(c) Weakly coupled double dot (T = 10 μeV) as a function of detuning for $B = 2\,$T. The panels display the relaxation rates for the first excited state, the unpolarized triplet, and T_{-} respectively. (d) Unbiased double dot as a function of interdot distance (in units of l_0) for $B = 5\,$T. The relaxation rate of T_0 is shown.

In large parts of the parametric space the relaxation of T_0 is dominated by nuclear spins, thus being isotropic. This is surprising, since the effective (Overhauser) nuclear magnetic field $B_{\rm nuc}$ is of the order of mT, much smaller than the spin-orbit field in Eq. (4.11), $B_{\rm so} \sim (l_0/l_{\rm so})B \approx 30\,$mT at $B = 1\,$T for our parameters. One therefore expects the nuclei to lead to much slower relaxation than the spin-orbit coupling. This was indeed the case for the unbiased dots, see Figs. 4.2 and 4.4. How can then nuclei dominate here? Looking at Fig. 4.1(b), this happens when states T_0 and $S(1,1)$ are nearby in energy. Here, the otherwise negligible hyperfine effects take over, because the spin-orbit induced mixing of these two states is forbidden [234]. Estimating the wave function admixture in the lowest order, the nuclei dominate if

$$B_{\rm so}/|E_{T_0} - E_k| \lesssim B_{\rm nuc}/|E_{T_0} - E_S|, \tag{4.12}$$

with k being the closest state to which T_0 is coupled by the spin-orbit interaction.

The above condition can be generalized in an obvious way for states other than T_0. According to Eq. (4.12), there are additional cases of nuclear dominance in our system, which happen on parameter regions too small to be visible on the resolution of Fig. 4.6. We discuss them in the following:

Comparing the value of the nuclear and spin-orbit effective fields, we estimate the relaxation due to the former is typically three orders of magnitude smaller, $(B_{\mathrm{nuc}}/B_{\mathrm{so}})^2 \sim 10^{-3}$, if the external field is of the order of Tesla. However, in a weakly coupled detuned double dot the nuclear spins can dominate over the spin-orbit induced relaxation in some cases, when Eq. (4.12) is satisfied. We plot in Fig. 4.7 the spin relaxation rates enabled by spin-orbit and hyperfine coupling, respectively. Panel a) gives the relaxation rate of the first excited state. The hyperfine coupling becomes relevant only close to the S-T_+ anticrossing along the easy passage. Here, the wide dip is narrowed (red versus the blue curve in Fig. 4.7). However, the rate remains reasonably low, such that the easy passage survives. Adding the nuclear dominated area to Fig. 4.6(a) would barely be visible. Panel b) shows the rate of T_0. We find that the hyperfine-induced relaxation is dominant for any in-plane magnetic field orientation if the unpolarized triplet is close in energy to the first excited singlet, as shown in Fig. 4.6(b). Panel c) displays the relaxation of T_-. At the S-T_- anticrossing, the spin-orbit induced relaxation strongly peaks unless the in-plane magnetic field orientation is perpendicular to the dot main axis. At the anticrossing, also the hyperfine-induced rate is enhanced. Displacing the magnetic field from the easy passage, the spin-orbit rate quickly gains on magnitude, therefore the nuclear-dominated area on Fig. 4.6(c) would cover only a single point at its current resolution. We show the relaxation rate for an unbiased dot in panel d) for comparison. We choose T_0 as an example, the state which is most prone to have relaxation dominated by nuclear spins in the biased dot. Here, the relaxation due to the spin-orbit coupling is several orders of magnitude larger than due to the nuclei, for any orientation of the external field. We observe a similar difference in rates for other states in this setup as well. Therefore, we omitted the discussion on the nuclei in the previous section.

4.3. Silicon

In the previous section we discussed the spin relaxation of a typical two-electron GaAs double dot. We presented a comprehensive picture of what we can expect while changing the model parameters for a wide range within the parametric space, noting that we can relate each parameter to experimentally relevant quantities. In this section, we focus on silicon-based dots and give a thorough picture of the spin relaxation,[2] as presented in Sec. 4.2 for GaAs.

For the silicon-based two-electron double dot, we assume the same material setup as in Sec. 3.3 for the single-electron dots. That is, we use the parameters of a SiGe/Si/SiGe quantum well grown along the $\hat{z} = [001]$ direction with a germanium concentration of 25%, where the two-dimensional electron gas is defined in the thin silicon layer with tensile strain [161, 194]. Other parameters are the isotropic effective mass $m = 0.198 m_e$, the effective Landé factor $g = 2$, the sound velocities $c_l = 9150\,\mathrm{m/s}$ and $c_t = 5000\,\mathrm{m/s}$, the mass density $\rho = 2330\,\mathrm{kg/m^3}$, the material dielectric constant $\varepsilon = 11.9\varepsilon_0$, the deformation potential constants $\Xi_\mathrm{d} = 5\,\mathrm{eV}$ and $\Xi_\mathrm{u} = 9\,\mathrm{eV}$, and the spin-orbit coupling lengths $l_\mathrm{br} = 38.5\,\mu\mathrm{m}$ and $l_\mathrm{d} = 12.8\,\mu\mathrm{m}$, like in Sec. 3.3. In this section we investigate also the role of the nuclei on the spin relaxation. For natural silicon, the ^{29}Si abundance is 4.7%, and we use an abundance of 0.01% for purified silicon [147, 148, 150]. The hyperfine coupling parameter reads as $\beta = -0.05\,\mu\mathrm{eV\,nm^3}$ [276], and ^{29}Si has spin $I = 1/2$. In analogy to Sec. 3.3, we take the confinement length $l_0 = 20\,\mathrm{nm}$, corresponding to the confinement energy $E_0 = 1.0\,\mathrm{meV}$. In the following, the double dot is oriented as $\mathbf{d} \,||\, [110]$, and the magnetic field is in-plane. The energy spectrum of the two-electron dot is introduced in Sec. 4.3.1, and the spin relaxation is discussed in Sec. 4.3.2.

The numerical algorithm is the same as in Sec. 4.2, further described in Appendix A. In the following, we use again 1156 Slater determinants [279] for the two-electron basis, generated by 34 single-electron orbital states. The discretization grid is typically 135×135, and the relative error for energies is below 10^{-5}. In Sec. 4.3.2 we present also an analytical solution of Eq. (3.12) for weakly coupled dots in low magnetic fields—a regime which can be solved adopting some approximations.

4.3.1. Energy Spectrum

Within the single-valley approximation (discussed in Chap. 2), the energy spectrum of the silicon-based two-electron double dot is qualitatively identical to the GaAs-based counterpart, see Sec. 4.2. On a quantitative level, however, there are some important differences. In this section, we quantify a realistic silicon dot and compare the outcome with GaAs. We also present the energy spectra of the unbiased and biased double quantum dot that we use in Sec. 4.3.2 to discuss the spin relaxation.

---

[2] Parts of Sec. 4.3 are based on Raith et. al., *Theory of spin relaxation in two-electron laterally coupled Si/SiGe quantum dots*, Phys. Rev. B 86, 205321 (2012) [283].

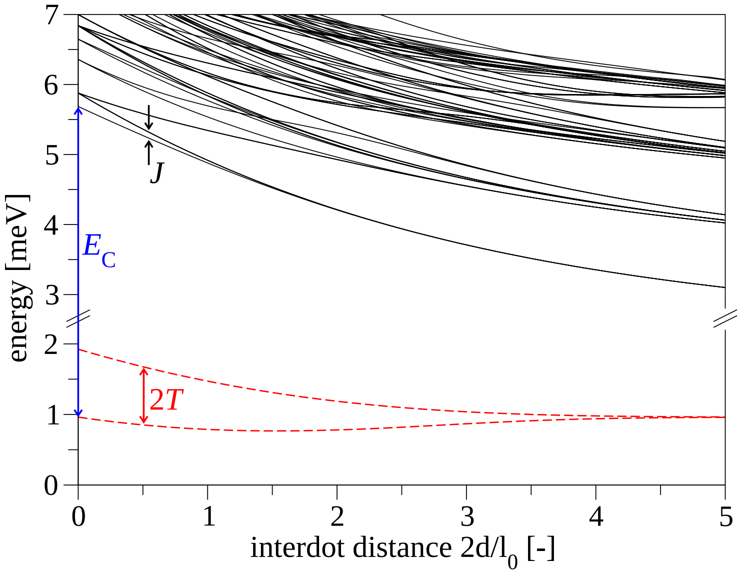

Figure 4.8.: Calculated energy spectrum (lowest 100 states) of a two-electron silicon double dot as a function of interdot distance (black solid lines) without an external magnetic field. The exchange splitting J is also indicated. For comparison, we also give for the same dot parameters the energies of the two lowest single-electron states (red dashed lines), which are split by $2T$, where T is the tunneling energy (see Sec. 3.3 for details). The single-dot charging energy is $E_\mathrm{C} = 4.72\,\mathrm{meV}$.

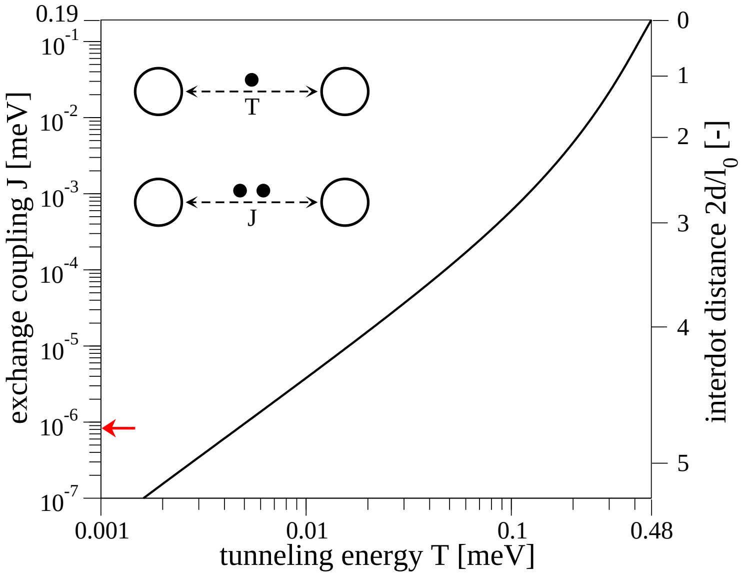

Figure 4.9.: Calculated conversion between the single-electron tunneling energy T (x axis), the two-electron exchange coupling J (left y axis), and the interdot distance $2d/l_0$ (right y axis) of a silicon double dot. In this data, we leave out the nuclear spins. The arrow gives E_nuc, Eq. (4.13), of natural silicon.

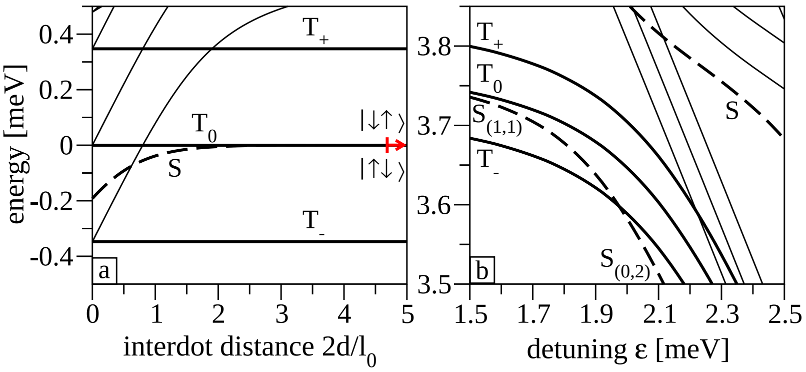

Figure 4.10.: Calculated energies of the lowest states in a silicon double dot varying (a) the interdot coupling (at $B = 3$ T) and (b) the detuning (at $B = 0.5$ T, and $2d/l_0 = 2.85$, i.e. $T = 0.1$ meV). Singlet states are given by dashed and the triplets by solid lines. In (a), the energy of T_0 is subtracted, and in (b), the quadratic trend in E is subtracted. The arrow in (a) marks where $J = E_{\text{nuc}}$ (for natural silicon).

Unbiased Double Dot We plot the energy spectrum of an unbiased silicon double dot as a function of interdot distance in Fig. 4.8. The analog graph for GaAs with a comparable confinement energy ($E_0 = 1.1$ meV) can be found in Ref. [280]. We find that due to the smaller material dielectric constant and larger effective mass, the exchange energy $J = E(T_0) - E(S)$ in silicon is smaller compared to GaAs. For our choice of parameters, we obtain $J_{\text{SD}} = 192\ \mu$eV (Si) and $J_{\text{SD}} = 298\ \mu$eV (GaAs) for the single dot ($d = 0$). The charging energy, which is the energy difference between the single-electron ground state and the two-electron ground state, is for the silicon single dot $E_{\text{C}} = 4.72$ meV, while $E_{\text{C}} = 3.45$ meV for GaAs. We plot the conversion between the tunneling energy T, the exchange coupling J, and the dimensionless interdot distance $2d/l_0$ for the silicon dot in Fig. 4.9.

The numerically calculated energy spectrum of the unbiased double dot in a magnetic field is shown in Fig. 4.10(a). We choose an exemplary magnetic field of $B = 3$ T. The Zeeman energy $E_{\text{Z}} = g\mu_{\text{B}}B$ exceeds J for magnetic fields beyond 1.7 T. Consequently, we find that T_- is the ground state for all interdot distances. The singlet therefore has an anticrossing with an excited triplet in the strong coupling regime, here at $J = 75\,\mu$eV for our choice of parameters. This scenario is hardly met in comparable GaAs double quantum dots, because the required magnitude of the magnetic field is above 10 T mainly due to the smaller g factor. The silicon spectrum of the unbiased double dot resembles the GaAs spectrum for magnetic fields below 1.7 T.

At large interdot distances, the hyperfine coupling induces a splitting of S and T_0, given by

$$E_{\text{nuc}} = 2\sqrt{\left|\sum_{i=1,2} \langle \phi_a T_0 | H_{\text{nuc},i} | \phi_s S \rangle \right|^2}\,. \tag{4.13}$$

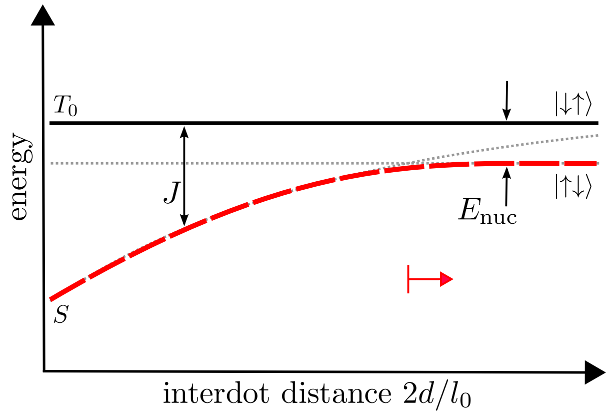
energy
T_0
$|\downarrow\uparrow\rangle$
J
$|\uparrow\downarrow\rangle$
$E_{\rm nuc}$
S
interdot distance $2d/l_0$

Figure 4.11: Schematic energy spectrum of an unbiased double dot showing the singlet S (dashed line) and the triplet T_0 (solid line). For large interdot distances, the exchange coupling J is given by the hyperfine splitting $E_{\rm nuc}$, Eq. (4.13), and the eigenstates change to $|\downarrow\uparrow\rangle$ and $|\uparrow\downarrow\rangle$.

In this regime, the lowest eigenstates are $|\uparrow\downarrow\rangle = (S + T_0)/\sqrt{2}$ and $|\downarrow\uparrow\rangle = (S - T_0)/\sqrt{2}$ (see Fig. 4.11). We evaluate Eq. (4.13) by averaging over random nuclear spin ensembles, and obtain $E_{\rm nuc} \approx 1$ neV for natural and $E_{\rm nuc} \approx 0.04$ neV for purified silicon. This implies a crossover to the nuclear dominated regime at $2d/l_0 \gtrsim 4.7$ [red arrows in Figs. 4.9, 4.10(a), and 4.11] for natural, and at $2d/l_0 \gtrsim 5.4$ for purified silicon.

Biased Double Dot Now we consider a weakly coupled double dot with a finite detuning energy ϵ. Figure 4.12 introduces important characteristic energies in a schematic energy spectrum. The state charge character is given in parenthesis: (1,1) indicates that there is one electron in each dot, and (0,2) states that both electrons are in the same dot. In the spectra, we subtract the quadratic trend in the electric field E. This way, the (1,1) states are displayed horizontally unless influenced by anticrossings. The important quantities are the ST-splitting of the single dot, denoted $J_{\rm SD}$ in the following, the exchange coupling J, and the singlet and triplet anticrossing energy splittings, labeled in Fig. 4.12. The ST-splitting $J_{\rm SD}$ is set by the material parameters, i.e. the Coulomb interaction, and the system parameters, i.e. the confinement length. For non-interacting electrons, $J_{\rm SD}$ is equal to the confinement energy E_0, here 1 meV. For interacting particles, the Coulomb repulsion has a strong impact on the symmetric ground state, the singlet, as here the electrons tend to group together. The first excited state, the triplet, is antisymmetric with respect to point reflection at the dot origin, and therefore less affected. As a consequence, $J_{\rm SD}$ decreases as the Coulomb interaction strength increases. For our choice of parameters $J_{\rm SD} = 0.2\,$meV (see above). In contrast, $J_{\rm SD}$ increases as the confinement length decreases. For instance, a confinement length of $l_0 = 17\,$nm results in $J_{\rm SD} \approx 0.3\,$meV. This can be understood as follows [284]. On the one hand, a stronger confinement increases the Coulomb strength due to smaller effective particle distances $|\mathbf{r}_1 - \mathbf{r}_2|$ in $H_{\rm C}$. This is an effect somewhat linear in l_0^{-1}. Then, one could expect $J_{\rm SD}$ to decrease. However, the confinement energy E_0 scales as l_0^{-2}, by which the exchange coupling increases in a similar way. This scaling

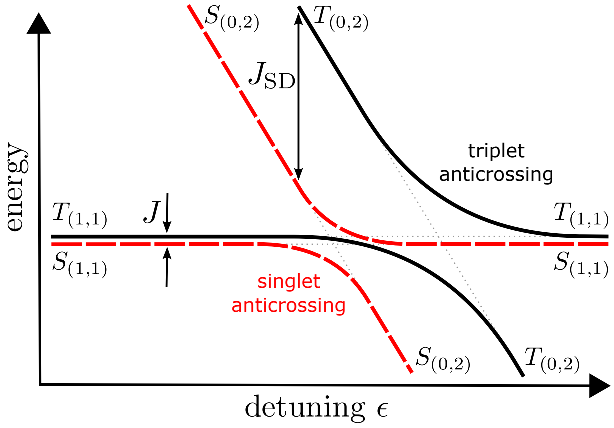

Figure 4.12: Schematic energy spectrum of a biased double dot without magnetic field. The singlets are given by dashed and the triplets by solid lines.

dominates such that the ST-splitting of the single dot increases. The exchange coupling J decreases exponentially with increasing interdot distance d [285]. In the weak coupling regime it holds that $J \ll J_{\mathrm{SD}}$, and we choose d such that $J = 0.6\ \mu\mathrm{eV}$ (that is $2d/l_0 = 2.85$, and $T = 0.1\,\mathrm{meV}$). The anticrossing gap of a spin-alike pair of states at the (1,1) $\leftrightarrow$ (0,2) transition depends on the interdot distance as well. For increasing d (decreasing J), these gaps decrease, that is the anticrossings vanish as $2d/l_0 \to \infty$.

The numerically calculated energy spectrum is plotted in Fig. 4.10(b) for a magnetic field of $B = 0.5\,\mathrm{T}$. The spectrum is qualitatively different from the GaAs double dot counterpart (see Fig. 4.1). In the GaAs double dot, the singlet and triplet anticrossings gaps are small compared to the ST-splitting of the single dot. Consequently, the singlet anticrossing is well separated from the triplet anticrossing, and the excited singlet is close to T_0 between these anticrossings. In the silicon dot this is not the case, as we can see in Fig. 4.10(b). Unless for exceedingly large interdot distances, the singlet-singlet and the triplet-triplet anticrossings overlap significantly. As a consequence, also the relaxation rate maps look qualitatively very different compared to GaAs, presented in Sec. 4.2.2. We discuss the relaxation in the following.

4.3.2. Spin Relaxation

Unbiased Double Dot We plot the relaxation rates of the states S, T_0, and T_+, denoted in Fig. 4.10(a), as functions of the interdot distance and in-plane magnetic field orientation for the unbiased double dot in Fig. 4.13. We also show the relaxation rates of individual channels for the two principal axes, that is for the in-plane magnetic field components parallel and perpendicular to the dot main axis $\mathbf{d}$, in the upper and lower panels of Fig. 4.14, respectively. We find that the relaxation rate of the singlet is highly anisotropic [237], which can be explained by the effective spin-orbit magnetic field, Eq. (4.11), discussed in Sec. 4.2.2. The spin lifetime is maximal if $\mathbf{B} \parallel \mathbf{d}$, reaching the order of tens of milliseconds for any dot coupling strength (red curve in the upper

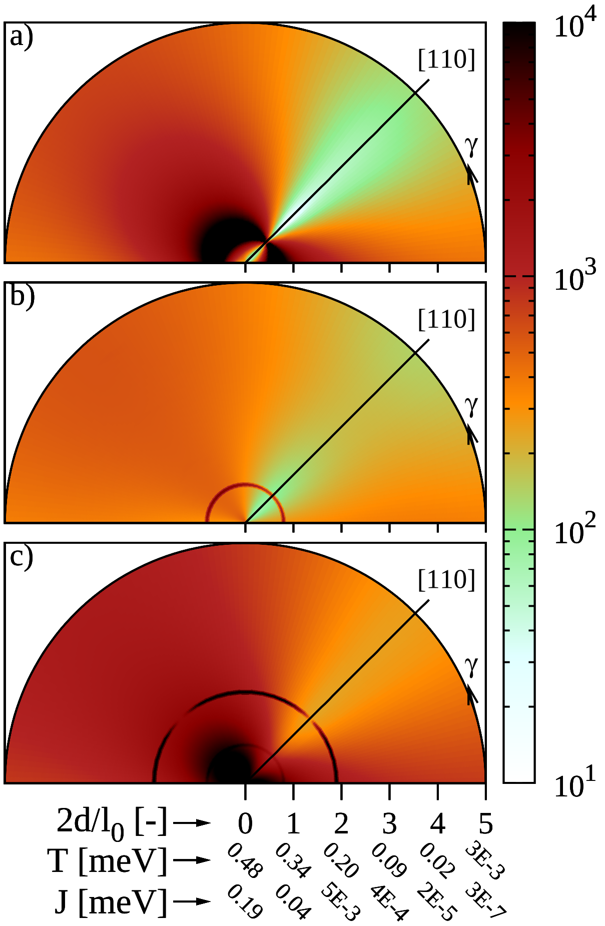

Figure 4.13.: Calculated relaxation rates of (a) the singlet, (b) the triplet T_0, and (c) the triplet T_+ as functions of the in-plane magnetic field orientation γ (angle) and the interdot distance $2d/l_0$ (radius of the polar plot), for a double dot at $B = 3\,\mathrm{T}$. The corresponding energy spectrum is given in Fig. 4.10(a). The x and y axes correspond to crystallographic axes $[100]$ and $[010]$, respectively. The dot orientation $\mathbf{d} \parallel [110]$ is marked by a line. The x axis is converted to the tunneling energy T and the exchange J, in addition to $2d/l_0$. The rate is given in inverse seconds by the color scale. The system obeys C_{2v} symmetry, so point reflection would complete the graphs.

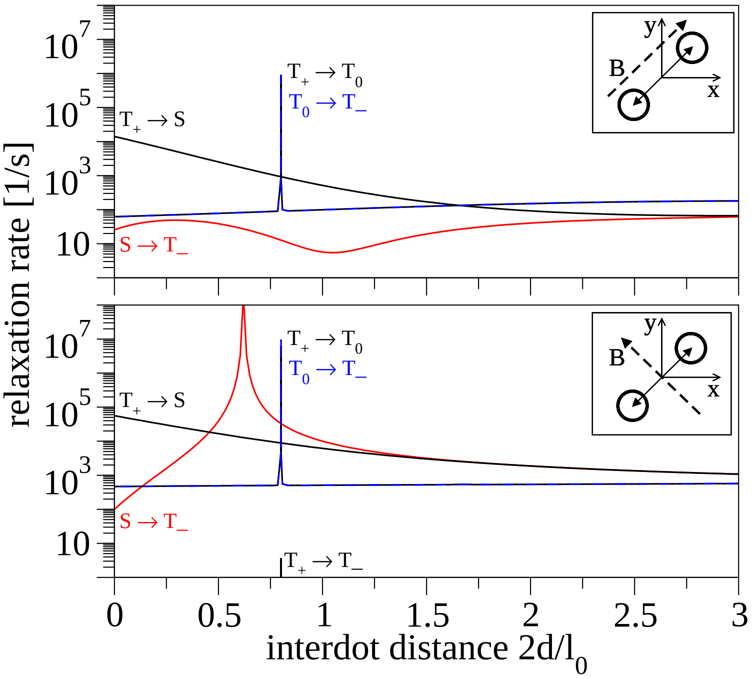

Figure 4.14.: Calculated channel-resolved relaxation rates vs. interdot distance for both parallel (top) and perpendicular to $\mathbf{d}$ (bottom) in-plane magnetic field orientation ($B = 3$ T). The corresponding energy spectrum is given in Fig. 4.10(a). The relaxation channels of T_+ are displayed in black, of T_0 in blue, and of S in red color.

panel of Fig. 4.14). As previously defined, we call this characteristic an easy passage [199, 238]. In the strong coupling regime, the rate away from the easy passage is enhanced by orders of magnitude. This results from the coupling of the singlet with the excited triplet, which favors the transition into T_-. For $\mathbf{B} \parallel \mathbf{d}$, the rate at the anticrossing is extremely sensitive to variations of γ, such that the easy passage becomes very narrow.

The relaxation rate of T_0 is given in Fig. 4.13(b). We find the same general anisotropic behavior, which is that the rate is minimal for $\mathbf{B} \parallel \mathbf{d}$. Figure 4.14 shows that the dominant channel of the relaxation is the transition $T_0 \to T_-$. Consequently, there is no impact from the singlet-triplet anticrossing [see Fig. 4.10(a)]. However, the anticrossing of the excited triplet with T_0 manifests itself in a very sharp peak of its rate. This spike is also anisotropic, with a difference of roughly one order of magnitude [not visible in Fig. 4.13(b) due to its resolution].

Fig. 4.13(c) shows the relaxation rate of T_+. In addition to the anisotropic background, there are two spikes of enhanced rate generated by the anticrossings of T_+ with the excited triplets. The enhancement close to the single dot regime originates

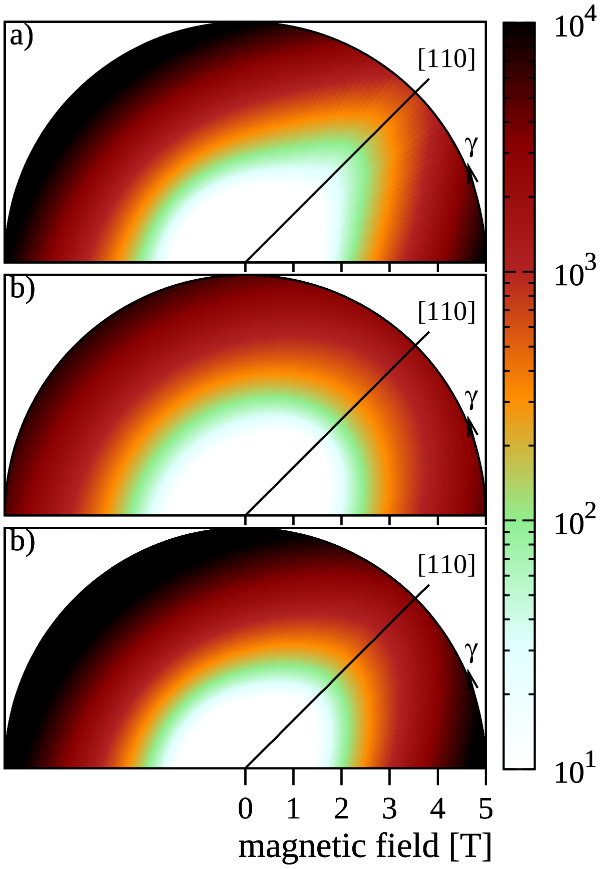

Figure 4.15.: Calculated relaxation rates of (a) the singlet, (b) the triplet T_0, and (c) the triplet T_+ as a function of the in-plane magnetic field orientation γ (angle) and the magnetic field magnitude (radius of the polar plot), for a double dot with $2d/l_0 = 2.85$ ($T = 0.1\,\text{meV}$). The layout with respect to the crystallographic axes is the same as in Fig. 4.13. The rate is given in inverse seconds by the color scale.

from the dominant $T_+ \rightarrow S$ transition (see Fig. 4.14). Interestingly, the anticrossing of the singlet hardly influences the overall trend of this relaxation channel.

For completeness, we plot in Fig. 4.15 the relaxation rates of a weakly coupled double dot as a function of the in-plane magnetic field. Here we find the same qualitative behavior for all three panels. As in Fig. 4.13, the relaxation rate is minimal for $\mathbf{B} \parallel \mathbf{d}$, but there are no spin hot-spots here.

Analytical Calculation of Relaxation Rates In the following we analytically calculate the relaxation rate, Eq. (3.12), of an unbiased silicon double dot adopting several approximations. The calculation proves useful to explain the physical mechanism and to verify our numerical results. The validity of the adopted approximations will be discussed afterwards. In the following, the hyperfine coupling is neglected.

Approximating the sum in Eq. (3.12) by an integral, and rewriting the δ-function with respect to the z component of $\mathbf{Q}$, we obtain $(i \neq j)$

$$\Gamma_{ij} = \frac{E_{ij}}{8\pi^2 \rho \hbar^2} \sum_{\lambda} \int \mathrm{d}\mathbf{q} \int \mathrm{d}Q_z \, \frac{Q}{c_\lambda^3 \bar{Q}_z^\lambda} \left| D_{\mathbf{Q}}^\lambda \right|^2 |M_{ij}|^2 \left[\delta(Q_z - \bar{Q}_z^\lambda) + \delta(Q_z + \bar{Q}_z^\lambda) \right], \quad (4.14)$$

where $\bar{Q}_z^\lambda = \sqrt{E_{ij}^2/(\hbar^2 c_\lambda^2) - q^2}$. Assuming the validity of the dipole approximation, the matrix element reads as

$$M_{ij} \approx \mathrm{i} \langle i | \mathbf{q} \cdot (\mathbf{r}_1 + \mathbf{r}_2) | j \rangle, \quad (4.15)$$

where $|i\rangle$ and $|j\rangle$ are the spin-orbit coupled two-electron eigenstates. Note that the contribution of the wave function overlap along the z direction in M_{ij} is about 1 [199], which is consistent with the two-dimensional approximation. We restrict ourselves to weakly coupled double dots, i.e. $d \gg l_0$, and incorporate the effect of spin-orbit coupling perturbatively via the unitary transformation given in Sec. 3.3.2. For the eigenstates, it holds (l labels the electrons)

$$|i\rangle = U \left(|i\rangle_0 + \sum_k \sum_{l=1,2} \frac{{}_0\langle k | \bar{H}_{\mathrm{so},l} | i \rangle_0}{E_i^0 - E_k^0} |k\rangle_0 \right), \quad (4.16)$$

where the transformation operator U, introduced in Eq. (3.18) for single-electron states, now reads as

$$U = \exp\left(\frac{\mathrm{i}}{2} \sum_{l=1,2} \mathbf{n}_{\mathrm{so},l} \cdot \boldsymbol{\sigma}_l \right). \quad (4.17)$$

The spin rotation axis $\mathbf{n}_{\mathrm{so}}$ is given in Eq. (3.19). The transformation yields the effective spin-orbit operator $\bar{H}_{\mathrm{so},l} = \bar{H}_{\mathrm{so},l}^Z + \bar{H}_{\mathrm{so},l}^{(2)}$, where

$$\bar{H}_{\mathrm{so},l}^Z = \frac{g}{2} \mu_{\mathrm{B}} (\mathbf{n}_{\mathrm{so},l} \times \mathbf{B}) \cdot \boldsymbol{\sigma}_l, \quad (4.18)$$

$$\bar{H}_{\mathrm{so},l}^{(2)} = \frac{\hbar}{4m} \left(\frac{1}{l_{\mathrm{d}}^2} - \frac{1}{l_{\mathrm{br}}^2} \right) L_{z,l} \sigma_{z,l} + \mathrm{const.} \quad (4.19)$$

Here, $L_z = l_z + (e/2)r^2 B_z$, where l_z is the angular momentum operator. The states in Eq. (4.16), labeled with subscript 0, are eigenstates of the Hamiltonian

$$H^0 = \sum_{i=1,2} (T_i + V_i + H_{Z,i}) + H_\mathrm{C}, \tag{4.20}$$

their eigenenergies are denoted as E^0. We use the Heitler-London ansatz [286] to approximate the eigenstates of Eq. (4.20).

We evaluate the matrix element M_{ij} using the states given in Eq. (4.16). First, we demonstrate that contributions from coupling within the lowest four-dimensional subspace $\mathcal{M} = \{S, T_-, T_0, T_+\}$ are zero or exponentially suppressed in d/l_0. Then, we calculate M_{ij} considering higher excited states.

Within the subspace $\mathcal{M}$, the sum over k in Eq. (4.16) includes only the singlet and the three triplets at the bottom of the energy spectrum. In this case, the matrix element M_{ij}, Eq. (4.15), reads as

$$M_{ij}\Big|_{\mathcal{M}} \approx 2\mathrm{i} \sum_{l=1,2} \frac{{}_0\langle i|\bar{H}_{\mathrm{so},l}|j\rangle_0}{E_j^0 - E_i^0} \Big({}_0\langle i|q_x x_1 + q_y y_1|i\rangle_0 - {}_0\langle j|q_x x_1 + q_y y_1|j\rangle_0 \Big). \tag{4.21}$$

Note that other terms in $M_{ij}\big|_{\mathcal{M}}$ vanish because the matrix elements of the electron-phonon coupling are zero for states with different spin. In addition, the matrix elements ${}_0\langle i|q_x x_1 + q_y y_1|i\rangle_0$ and ${}_0\langle j|q_x x_1 + q_y y_1|j\rangle_0$ vanish also upon integration because of the orbital symmetry of the quantum dot states [280], which can be easily verified by explicit calculation using the Heitler-London ansatz. Finally, we obtain

$$M_{ij}\Big|_{\mathcal{M}} \approx 0, \tag{4.22}$$

and therefore a negligible contribution to the relaxation rate.

Now we consider higher excited states for the expansion Eq. (4.16), and calculate M_{ij}. Neglecting the L_z contribution to the effective spin-orbit coupling, Eq. (4.19), we obtain

$$\begin{aligned} \frac{M_{ij}}{\mathrm{i}g\mu_\mathrm{B}} = \sum_{k \notin \mathcal{M}} \sum_{l=1,2} \Bigg[& \frac{{}_0\langle i|(\mathbf{n}_{\mathrm{so},l} \times \mathbf{B}) \cdot \boldsymbol{\sigma}_l|k\rangle_0}{E_i^0 - E_k^0} {}_0\langle k|q_x x_1 + q_y y_1|j\rangle_0 + \\ & + \frac{{}_0\langle k|(\mathbf{n}_{\mathrm{so},l} \times \mathbf{B}) \cdot \boldsymbol{\sigma}_l|j\rangle_0}{E_j^0 - E_k^0} {}_0\langle i|q_x x_1 + q_y y_1|k\rangle_0 \Bigg] . \end{aligned} \tag{4.23}$$

The singlet is symmetric with respect to the inversion operator I_{xy} (point reflection in real space), the triplets are antisymmetric [280]. Consequently, it follows from Eq. (4.23) that, within the dipole approximation, the singlet-triplet transition is forbidden. We also find that Eq. (4.23) forbids a $T_+ \leftrightarrow T_-$ transition because the effective spin-orbit operator $\bar{H}^Z_{\mathrm{so},l}$ acts on only one of the two electron spins. Let us now look at the transition between T_0 and $T_\pm$.

To evaluate Eq. (4.23), we reduce the infinite sum over k to cover only states within the energy window of about the confinement energy $E_0 = \hbar^2/(ml_0^2)$. Additionally, we can exclude any singlet from the sum, because the electron-phonon operator does not act in spin space. What is left can be captured by the Heitler-London approach.

Let $|\mathrm{R0}\rangle$ be the (orbital) ground state of a single dot shifted to the right by d, i.e. the Fock-Darwin state [87, 265, 266] of the right dot with the principal quantum number $n = 0$ and the orbital quantum number $l = 0$. Analogously we define the ground state of the left dot. The properly symmetrized triplet lowest in energy is

$$|\Psi_T\rangle_0 = (|\mathrm{R0},\mathrm{L0}\rangle - |\mathrm{L0},\mathrm{R0}\rangle) \otimes |T\rangle/\sqrt{2}. \tag{4.24}$$

The orbitally excited triplets can be constructed analogously, using $|\mathrm{R1}\rangle$ and $|\mathrm{L1}\rangle$, the displaced Fock-Darwin states with $n = 0$ and $|l| = 1$:

$$|k_\pm\rangle_0 = [|\mathrm{R0},\mathrm{L1}\rangle - |\mathrm{L1},\mathrm{R0}\rangle \pm (|\mathrm{R1},\mathrm{L0}\rangle - |\mathrm{L0},\mathrm{R1}\rangle)] \otimes |T\rangle/2. \tag{4.25}$$

Neglecting the wave function overlap of states localized in different quantum dots, we calculate the matrix elements ${}_0\langle\Psi_T|x_1|k_\pm\rangle_0$ and ${}_0\langle\Psi_T|y_1|k_\pm\rangle_0$ analytically, yielding

$$\begin{aligned} {}_0\langle\Psi_T|x_1|k_+\rangle_0 &= l_0/\sqrt{8}, && (4.26)\\ {}_0\langle\Psi_T|y_1|k_+\rangle_0 &= \mathrm{sgn}(l)\mathrm{i}l_0/\sqrt{8}, && (4.27) \end{aligned}$$

and ${}_0\langle\Psi_T|x_1|k_-\rangle_0 = {}_0\langle\Psi_T|y_1|k_-\rangle_0 = 0$. We use Eqs. (4.26) and (4.27) as an approximation for the matrix elements in Eq. (4.23). We also require the matrix elements of Pauli matrices respecting the spin quantization axis along $\mathbf{B}$. They read as

$$\langle T_\pm|\boldsymbol{\sigma}_1|T_0\rangle = \frac{\mathrm{e}^{\mp\mathrm{i}\gamma}}{2\sqrt{2}}\begin{pmatrix}\cos(\gamma-\theta)+\cos(\gamma+\theta)\pm 2\mathrm{i}\sin(\gamma)\\ \sin(\gamma-\theta)+\sin(\gamma+\theta)\mp 2\mathrm{i}\cos(\gamma)\\ 2\sin(\theta)\end{pmatrix}, \tag{4.28}$$

where $\theta = \cos^{-1}(B_z/B_\parallel)$. The energy differences in Eq. (4.23) are approximated by the confinement energy, $E_0 = \hbar^2/(ml_0^2)$.

With these ingredients, we can solve Eq. (4.14), integrating over the phonon momentum, and finally obtain

$$\begin{aligned}\Gamma_{T_0\to T_-} &= \Gamma_{T_+\to T_0} = \\ &= \frac{m^2 l_0^8 \mathcal{L}_{\mathrm{so}}^{-2}}{12\pi\rho\hbar^{10}}(g\mu_{\mathrm{B}}B)^7\left[c_l^{-7}\left(\frac{3}{35}\Xi_{\mathrm{u}}^2+\frac{2}{5}\Xi_{\mathrm{u}}\Xi_{\mathrm{d}}+\Xi_{\mathrm{d}}^2\right)+c_t^{-7}\frac{4}{35}\Xi_{\mathrm{u}}^2\right],\end{aligned} \tag{4.29}$$

with the effective spin-orbit length $\mathcal{L}_{\mathrm{so}}$, defined by

$$\mathcal{L}_{\mathrm{so}}^{-2} = \begin{cases} 2\left(l_{\mathrm{br}}^{-2}+l_{\mathrm{d}}^{-2}\right) & \text{if } \theta = 0,\\ l_{\mathrm{br}}^{-2}+l_{\mathrm{d}}^{-2}-2\frac{\sin(2\gamma)}{l_{\mathrm{br}}l_{\mathrm{d}}} & \text{if } \theta = \pi/2.\end{cases} \tag{4.30}$$

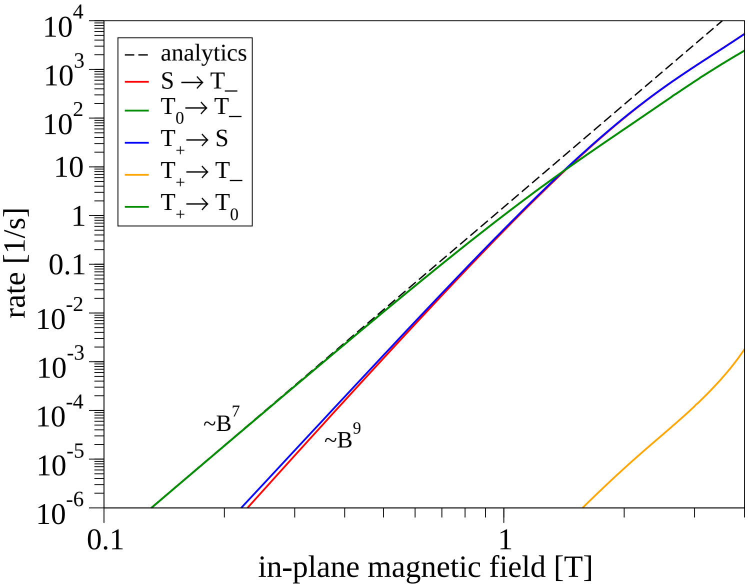

Figure 4.16.: Calculated relaxation rates of individual transition channels as a function of in-plane magnetic field for a weakly coupled quantum dot. The magnetic field is oriented along $[\bar{1}10]$ ($\gamma = 3\pi/4$), and the dots along $[110]$ ($\delta = \pi/4$). The interdot distance is $2d/l_0 = 2.85$ ($T = 0.1$ meV). The dashed, black line gives the analytical relaxation rate, evaluated with Eq. (4.29).

Now we discuss the validity of the approximations used during the derivation of Eq. (4.29). The matrix element M_{ij} is calculated using the dipole approximation, Eq. (4.15). It requires that the energy difference between the transition states, here T_0 and $T_\pm$, fulfills $E_{ij} \ll \hbar c_\lambda / l_0$ [199]. Using $E_{ij} = g\mu_{\mathrm{B}} B$, and $c_\lambda = c_t$, we obtain the condition $B \ll 1.4\,\mathrm{T}$. We consider also a weakly coupled double dot, $d \gg l_0$, to comply with most experiments. This limit ensures negligible matrix elements among the states of $\mathcal{M}$, and justifies the Heitler-London approximation. Here, the spectrum also develops bundles of eigenenergies separated by the confinement energy $E_0 = \hbar^2/(ml_0^2)$, a fact used to approximate the energy differences in Eq. (4.23). Note that within the restriction of the dipole approximation ($B \ll 1.4\,\mathrm{T}$), the Zeeman energy ($E_{\mathrm{Z}} \ll 0.16\,\mathrm{meV}$) is negligible compared to the confinement energy ($E_0 = 1\,\mathrm{meV}$). The Schrieffer-Wolff transformation is the essential tool for a perturbative treatment of spin-orbit coupling in a double dot [256]. Perturbation theory with the unitarily transformed Hamiltonian yields results which are of higher order in small quantities compared to the original Hamiltonian [237, 256]. Finally, we note that, since L_z is symmetric with respect to the inversion I_{xy}, the perturbation $\bar{H}^{(2)}_{\mathrm{so},l}$, Eq. (4.19), vanishes for all transitions $T_0 \leftrightarrow T_\pm$.

In Fig. 4.16, we compare the analytical formula for the relaxation rate of the transition $T_0 \to T_-$, and $T_+ \to T_0$, given in Eq. (4.29), with the numerical results. We find perfect agreement for low magnetic fields, in line with the condition $B \ll 1.4\,\mathrm{T}$. For larger magnetic fields, the results significantly deviate from the B^7 power law, due to the breakdown of the dipole approximation. We also find that the $S \leftrightarrow T_{\pm}$ relaxation channels, which we found to be zero in the lowest order dipole approximation due to their symmetry, show B^9 dependence, indicating that the relaxation is driven by the second order term of $\mathbf{q}$. Being of higher order, the relaxation rate, for small $\mathbf{B}$, is at least one order of magnitude lower than the $T_0 \leftrightarrow T_{\pm}$ transitions.

Biased Double Dot Finally, we consider the detuned silicon double dot. The corresponding energy spectrum is given in Fig. 4.10(b). The relaxation rate of the first excited state, that is S for detuning energies up to 1.97 meV, and T_- beyond, is plotted in Fig. 4.17(a). At the singlet-triplet anticrossing, the relaxation rate is very low as the transferred energy becomes very small. The easy passage occurs if the external, in-plane magnetic field is perpendicular to $\mathbf{d}$. The same anisotropy is visible for the relaxation rates of T_0 and T_+, Figs. 4.17(b) and 4.17(c), respectively. There is no signature of the singlet-triplet anticrossing in the rate because of the exact compensation of individual relaxation channels. Also, there is no indication of the crossing of T_+ with the excited triplet T_-. This rate behavior—anisotropies, easy passage directional switch, and the exact compensation—is analogous to the GaAs dot (see Sec. 4.2.2 for a detailed discussion and explanation). Other anticrossings with excited triplets (at $\epsilon \approx 2.47$ meV) manifest themselves in extremely narrow peaks of the rate, not visible in Fig. 4.17 at the current resolution.

In the following we discuss the possible effects of nuclear spins and show that the spin relaxation is essentially unaffected for experimentally relevant dot parameters. Comparing the hyperfine interaction strengths with the spin-orbit fields, the former are expected to be negligible. Indeed, the Overhauser field characterizing the fluctuating collective nuclear field [131],

$$\mathbf{B}_{\mathrm{nuc}} = \frac{\beta}{g\mu_{\mathrm{B}}} \left\langle \sum_n \mathbf{I}_n \left|\psi(\mathbf{R_n})\right|^2 \right\rangle, \tag{4.31}$$

of natural silicon is of the order of tens of μT, and for purified silicon (0.01% of ^{29}Si) even one order of magnitude lower. On the other hand, the effective spin-orbit field, Eq. (4.11), is about 2 mT at $B = 1$ T. The two fields become comparable for external magnetic fields below roughly 10 mT. This regime is not usually met in experiments, where a sizable Zeeman splitting is necessary for electron spin manipulations and measurements.

However, in Sec. 4.2.2 we found for the GaAs quantum dot that, despite the large discrepancy of the effective fields, there are anomalous cases where the above expectation fails and nuclei are indeed the dominant channel. This happens in a weakly coupled double dot biased to the $S_{1,1} - S_{0,2}$ anticrossing, if the corresponding anticrossing gap E_{S-S} is small enough. Namely, due to the absence of the spin-orbit coupling between

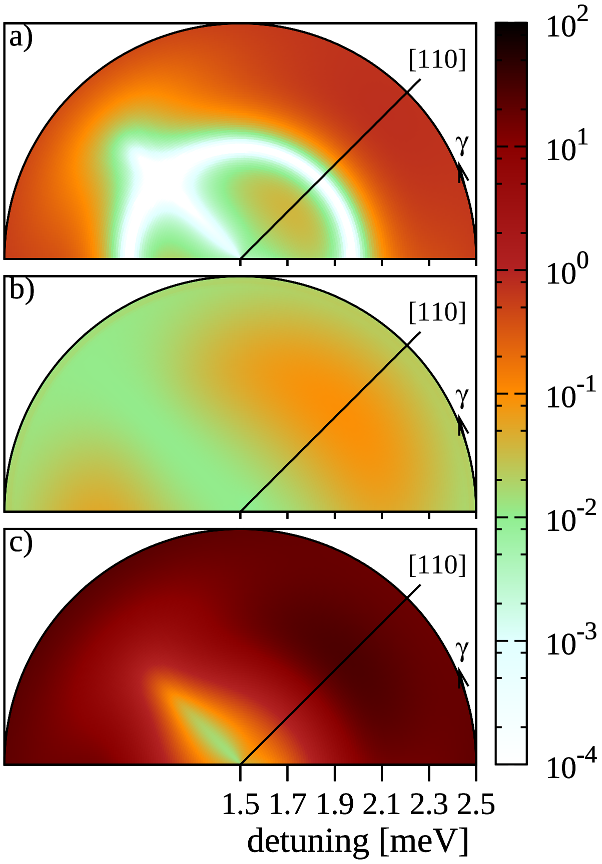

Figure 4.17.: Calculated relaxation rates of (a) the first excited state [S or T_-; see Fig. 4.10(b)], (b) T_0, and (c) T_+ as functions of the in-plane magnetic field orientation γ (angle) and detuning energy (radius of the polar plot), for a double dot with $2d/l_0 = 2.85$ ($T = 0.1$ meV), and $B = 0.5$ T. The layout with respect to the crystallographic axes is the same as in Figs. 4.13 and 4.15. The rate is given in inverse seconds by the color scale.

states T_0 and S, the small magnitude of the nuclear-induced wave function admixture is compensated by the small energetic distance between these two states. The very same mechanism is also present in Si, raising the question of the conditions needed for it to become manifest.

We illustrate the case by comparing Si to GaAs. For this, we assume that the single dot energy E_0 and the Zeeman energy are the same in the two quantum dots, each built in one of the two materials. We estimate the ratio of the exchange energies (which characterize the interdot coupling) below for which the nuclei dominate. As described in Sec. 4.2.2, the condition for this to happen is given by Eq. (4.12), where the effective magnetic fields B_{so} and B_{nuc} are defined in Eqs. (4.11) and (4.31), respectively. Let us approximate the energy difference $|E_{T_0} - E_S|$ by the $S_{1,1} - S_{0,2}$ anticrossing gap, denoted E_{S-S}, and $|E_{T_0} - E_k|$ by the orbital energy scale E_0. We define a “critical” $|E_{T_0} - E_S|$ energy difference by Eq. (4.12) with an equality sign. Approximating the two-electron wave functions by Slater determinants composed of localized Fock-Darwin states of a single dot, we get the following auxiliary results, valid for large interdot distances,

$$E_{S-S} \approx \frac{e^2}{\sqrt{2}\epsilon_0\epsilon_r d}\exp(-d^2/l_0^2), \tag{4.32}$$

and

$$J \approx \exp(-2d^2/l_0^2)\frac{4d}{\sqrt{\pi}l_0}\frac{\hbar^2}{ml_0^2}. \tag{4.33}$$

Both of these quantities fall off exponentially with increasing interdot distance in weakly coupled dots. However the $S_{1,1} - S_{0,2}$ anticrossing gap scales as the tunneling energy T, whereas the exchange energy is much smaller, $J \sim T^2/E_{\mathrm{C}}$, where E_{C} is the charging energy [287]. With these we get for the ratio of critical exchange energies

$$\frac{J_{\mathrm{crit}}^{\mathrm{Si}}}{J_{\mathrm{crit}}^{\mathrm{GaAs}}} \sim \left(p\frac{(I\beta l_{\mathrm{so}}\epsilon_r)_{\mathrm{Si}}}{(I\beta l_{\mathrm{so}}\epsilon_r)_{\mathrm{GaAs}}}\right)^2 \approx 10^{-6}. \tag{4.34}$$

Here p is the fraction of the isotope ^{29}Si. As discussed in Sec. 4.2.2, in a GaAs quantum dot with parameters typical in experiments, the nuclear dominance requires exchange energies of the order of $0.1\,\mu$eV. As follows from Eq. (4.34), the requirements are much more stringent in silicon. Here the exchange coupling J needs to be of the order of sub-peV, usually not pursued in experiments. The matrix elements of the spin-flipping transitions are in Si therefore dominated by the spin-orbit fields, rather than nuclear spin fields, and the same holds for anticrossing gaps. An illustration is given in Fig. 4.18. The reason for the dominance of spin-orbit coupling are the different material parameters, most importantly the much weaker coupling of the conduction electrons to the nuclear spins, and the low fraction of atoms with non-zero nuclear magnetic moment in silicon.

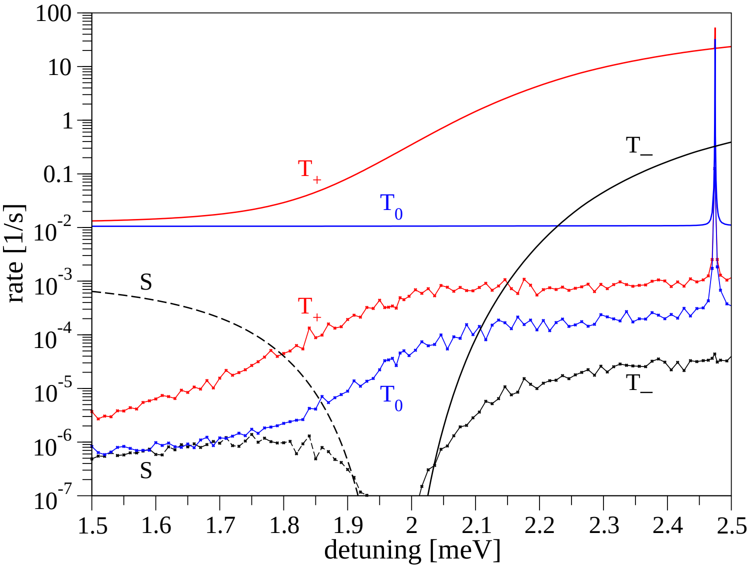

Figure 4.18.: Calculated relaxation rates of a detuned silicon double dot ($2d/l_0 = 2.85$, $T = 0.1$ meV) in an in-plane magnetic field ($B = 0.5$ T, $\gamma = 3\pi/4$) as a function of detuning. The straight lines give the spin-orbit induced relaxation, the wiggly lines the hyperfine induced relaxation rates (natural silicon).

A second possibility for the nuclei to dominate the spin relaxation is a dot detuned so far (such small J) that the singlet and triplet T_0 become degenerate with respect to $E_{\rm nuc}$. The Hamiltonian eigenstates change from entangled states into separable states, with spin up or down in the left or right dot, respectively (we show this schematically in Fig. 4.11). Note that the figures in the first part of Sec. 4.3.2 cover this regime, but the qualitative change in the eigenstate character has no visible effects on the relaxation rates (verified also for $2d/l_0 > 5$, not shown). This is because the relaxation to a fully spin polarized final state T_+ from the initial state S or T_0 (or any of their superpositions, such as $|\uparrow\downarrow\rangle$) proceeds through an individual single-dot spin-flip, with the transition matrix element magnitude being essentially the same in all these cases. Thus, the rate is not affected.

In the presence of a random nuclear field, the states may also undergo direct transitions without phonon assistance. Such transitions are possible if the eigenstates have unsharp energies (finite lifetimes). However, as the states we are interested in are low lying, even at finite temperature their energy broadening is so small that the resulting nuclear-induced spin relaxation is negligible.

Finally, a fourth possibility comes from the random character of the nuclear field itself. This statistical rather than quantum mechanical uncertainty, which blurs the electron energies, can be grasped roughly by convolution of the relaxation curves with a Gaussian with an appropriate width, depending on which parameter we change, defined ultimately by the energy $g\mu_B\mathbf{B}_{\text{nuc}}$. However, we find this width to be unnoticeably small—as an example, the extremely narrow peaks in Fig. 4.14 survive practically untouched by such smoothing. In other words, this effect does not change our results in any significant way.

We conclude that unpolarized nuclear spins in natural or purified Si are not expected to be visible in the electron spin relaxation within the parametric space we investigate. We find that such a situation might occur only for very small external fields ($B \leq 0.01$ T) or very weakly coupled dots ($J \leq$ peV), conditions hardly met in the experiment.

The figures presented and results discussed in this chapter are for zero temperature. In addition to the phonon emission processes present at zero temperature, a finite temperature in our model amounts solely to allowing for energy-increasing transitions (phonon absorption). Adopting a typical experimental value of 100 mK, we do not find any case where such additional transitions would change the relaxation rates in any significant way (figures not shown). Our conclusion from those investigations is that the relaxation character, most notably its anisotropies, will not be influenced by experimentally relevant subkelvin temperatures.

4.4. Summary

In Chap. 4, we discussed the spin relaxation of a laterally coupled two-electron quantum dot based on GaAs (Sec. 4.2) and Si (Sec. 4.3). The underlying theory, which was already introduced in Sec. 3.1 for the single-electron case, was extended in Sec. 4.1 to cope with two electrons. Other constraints, such as the single-valley approximation for the silicon-based dots, were already discussed in Chap. 2 and Sec. 3.1, and remained valid throughout the discussion of Chap. 4.

Perhaps the most striking results are the existence of islands of inhibited spin relaxation in the magnetic field and detuning maps, and the switch of the two principal C_{2v} axes along which the relaxation shows a minimum or maximum when detuning is turned on. This holds for both gallium arsenide and silicon quantum dots. The origin of both features is the anisotropy of the spin-orbit field, which manifests itself in the total spin relaxation rates of all states with only one exception. While all singlets and polarized triplets relax due to spin-orbit coupling, the relaxation of the spin-unpolarized triplet in biased GaAs dots is dominated by nuclear spins over a wide parameter range (the spin-orbit induced anisotropy is wiped out). Although in principle also present in silicon, we do not find this nuclear dominance in related relaxation rate maps. Here the effect is much harder to unveil. The reason is the different material parameters, which result in a rather small ST-splitting of the single dot compared to the anticrossing energy. This qualitative difference between GaAs and silicon can also be seen from the energy spectra of the detuned double dots close to the singlet-singlet anticrossing. Regarding the role of the nuclei in silicon, we find in general that the hyperfine-induced relaxation rates of natural silicon are typically two or more orders of magnitude lower than the spin-orbit induced relaxation rates. The hyperfine-induced rates of purified silicon (0.01% of ^{29}Si) are further suppressed by about two orders of magnitude compared to those in natural silicon. We therefore conclude that, concerning the relaxation, the nuclear field is negligible in silicon-based quantum dots. The predicted giant anisotropy of the spin relaxation in semiconductor dots is a unique and experimentally testable signature of spin relaxation enabled by spin-orbit coupling. It can also be useful for spin nanodevices (see Chap. 5).

The spin relaxation rates in silicon are typically at least two orders of magnitude lower than in comparable GaAs dots due to its small spin-orbit coupling. Moreover, the relaxation rate peaks at spin hot spots are very narrow in parameter space. We find that a temperature of 0.1 K does not change our findings in any qualitative way.

Our results demonstrate control over the spin-orbit induced anticrossing gaps (easy passages appear if the gaps are closed) by sample and magnetic field geometry. It offers electrical tunability of spin relaxation, by changing the double dot orientation (in Chap. 5, we suggest a spin current measurement device exploiting the easy passage). In addition, such control may be especially useful when dealing with hyperfine spins. Indeed, in the polarization scheme considered in Ref. [138], the nuclear spin polarization, is proportional to non-hyperfine assisted spin relaxation [see Eq. (7) therein] and so would benefit from a setup with maximized spin-orbit induced relaxation rates (out of the easy passage). On the other hand, the adiabatic pumping scheme, demonstrated in Ref. [282] relies on the S-T_+ anticrossing being solely due to the nuclear spins (and not the spin-orbit coupling), suggesting improved efficiency in an easy passage configuration. We present a similar non-adiabatic nuclear pumping scheme based on the easy passage in Chap. 5. All these examples illustrate the potential benefits which intentional control of the spin relaxation, based on our results, may offer.

CHAPTER 5

Conclusions and Outlook

Semiconductor quantum dots are among the top candidates for solid state qubits. Within this class of systems, the most important structures are top-gated lateral quantum dots, usually grown on gallium arsenide or silicon heterostructures. In most schemes, the qubit is defined by the spin state of a single electron, or the singlet-triplet states of two electrons. Manipulation and readout can be done electrically, supported by an additional magnetic field. However, two fundamental issues remain on the way to an operational quantum computer made of quantum dots: scalability and decoherence. A lateral dot requires several independent top-gates to control its dimensions (size and shape), the number of electrons, and the coupling to other dots and the leads. Moreover, for each dot there is a dedicated measurement device (a quantum point contact or another quantum dot), additional dots for error correction, and a magnetic field. It is obvious that the number of parameters increases immensely with each qubit. The scalability of top-gated dots is a serious and challenging issue, which needs to be addressed properly in the future with better designs and careful engineering. The other problem is decoherence. The quantum states of semiconductor dots are still too fragile for large scale quantum computation. For this reason, understanding and controlling the decoherence is a top priority for fundamental research.

In this thesis, we comprehensively investigated one form of decoherence, the spin relaxation, for single-electron spins and singlet-triplet states in laterally coupled double quantum dots. For the analysis, we used a robust microscopic model and exact numerical methods, supported by analytical calculations. For the first time, the two main environmental noise sources, the nuclear spins and the spin-orbit interactions, were included simultaneously. Our results provide a quantitative understanding of the spin relaxation for a wide range of experimentally relevant parameters. In this work, we considered both the well-established gallium arsenide quantum dots, and the recently revived silicon dots, which are advantageous because the majority of natural silicon is free of nuclear spins.

Until now the strength of the spin-orbit coupling, and in particular the anisotropy of the spin relaxation, has not been experimentally analyzed in weakly coupled quantum dots yet. Technical, rather than fundamental limitations, prohibited a systematic study. However, employing vector magnets it should now be possible to overcome earlier experimental challenges, change the magnetic field orientation while keeping the sample fixed, and detect the anisotropy [288]. Therefore, based on the quality of our model and the accuracy of our numerical method, we believe that our predictions can be observed in experiments. In principle, the spin-orbit- and nuclear-induced relaxation could be masked by cotunneling and smeared by a finite temperature. But the former is reduced in the charge sensing readout setups [289], in which the coupling to the leads can be made small, and the latter effect is small for experimentally relevant subkelvin temperatures, such that the directional anisotropies are well preserved.

In the following, we present two examples of how the easy passage of a two-electron double quantum dot (discussed in Chap. 4.2.2 and 4.3.2) could be used for the dynamical nuclear spin polarization and the detection of a spin polarized current.

Dynamical nuclear spin polarization Nuclear spins in the host material are the major source of decoherence. The dynamical nuclear spin polarization is a state preparation scheme that uses an electron-nuclear flip-flop cycle to polarize the nuclear spins. Ideally, in the case of a complete polarization, the magnetic field of the nuclear spins acts as a simple renormalization of the external magnetic field, which does not cause decoherence. And even at partial polarization, the decoherence time can be boosted by orders of magnitude [282]. We sketch two schemes of dynamical nuclear spin pumping in Fig. 5.1. The first is the one originally proposed by Reilly et. al. in Ref. [282]. Here, the double dot is initialized in the $S_{(0,2)}$ state. Then the system is adiabatically brought through the anticrossing (step 1), which flips a nuclear spin, assuming the anticrossing is due to the (transverse component of) the nuclear effective field (and not due to the spin-orbit coupling). Thus, placing the system into the easy passage, which was not done in the experiment, offers improved scheme efficiency. The cycle is finished by resetting the system into the $S_{(0,2)}$ state, through a fast transition (step 2) and a subsequent relaxation via spin-orbit coupling or an electron exchange with the reservoir (step 3).

Second, we present a non-adiabatic scheme of dynamical nuclear spin polarization, sketched in Fig. 5.1(b). Instead of changing the detuning slowly from $S_{(0,2)}$ to T_+, we go fast, but now we end step 1 at the anticrossing. This necessarily requires to monitor the anticrossing position, which however is possible. Here, the detuning is kept constant until the system relaxes to the ground state (step 2). This transition must be driven by the hyperfine coupling, such that a nuclear spin is flipped. After that, a fast change

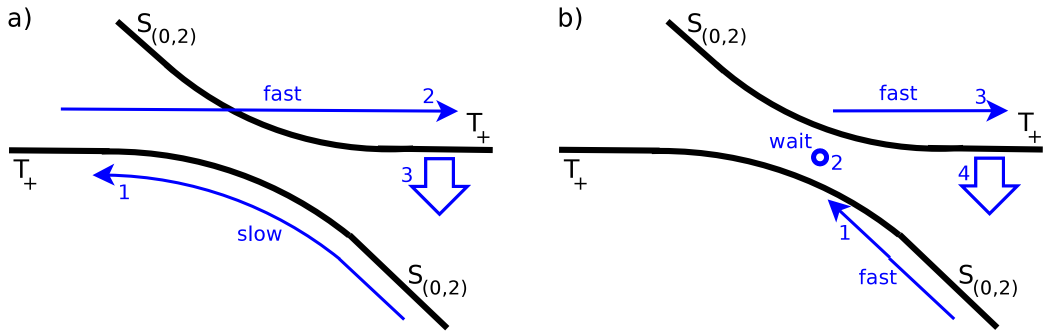

Figure 5.1.: Sketches of two schemes of dynamical nuclear spin pumping in a two-electron double quantum dot. The blue arrows indicate the path which the system state follows during one pump cycle.

of the bias brings the system into the excited T_+ state (step 3), where a mechanism other than hyperfine coupling must enable the transition to the ground state (step 4). Again, the scheme is most efficient if the spin-orbit contribution to the anticrossing gap is minimized, what happens in the easy passage configuration.

Spin polarization detection Here we propose a device that allows to detect the spin polarization of a lead using a weakly coupled double dot. The dot is connected to source and drain leads such that the current passes only through the left dot via single-electron tunneling. The system is biased in a range where only (1,0), (1,1) and (0,2) occupations of the double dot are allowed. For the measurement scheme, we repeatedly cycle through a specific sequence, which produces an effective resistance of the device depending on the spin polarization of the electrons in the source lead. For this sequence, the current experiences on average a lower resistance the higher the polarization. It goes as follows:

First, the double dot is initialized in the (1,0) configuration. That is, the right dot is emptied via a detuning energy which brings it above both source and drain leads. Current is allowed to flow through the left dot. Second, the right dot is lowered in energy by a gate, and the electron, which is traversing the device, may tunnel into the right dot and becomes trapped (we assume its spin is preserved). Now, if an electron with the same spin orientation enters the left dot, a $T_{+,(1,1)}$ triplet state with a long lifetime is formed, such that the electron in the left dot tunnels out and the current flows, see Fig. 5.2(a). If, on the other hand, an electron with opposite spin enters the left dot, the system quickly collapses into the $S_{(0,2)}$ state and the current is blocked, see Fig. 5.2(b). At this point, it is crucial that the energies of the system are chosen such that adding a third electron is prohibited by Coulomb blockade [290]. Finally, the system is reset again by emptying the right dot via a gate voltage, and the sequence can start from beginning.

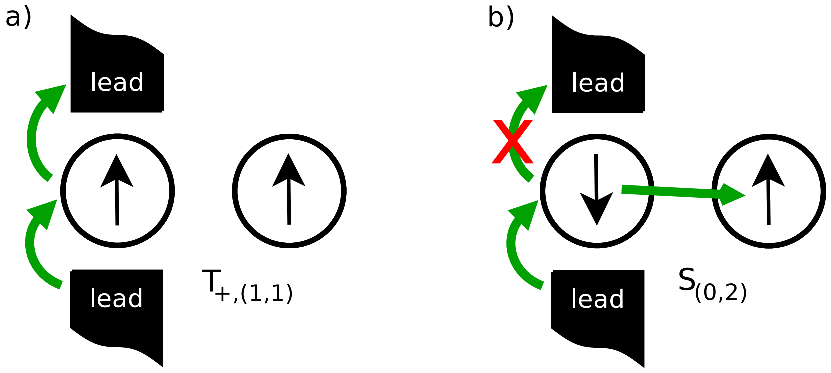

Figure 5.2.: Spin polarization detection scheme. (a) If the double dot is in the $T_{+,(1,1)}$ state, the current is enabled. (b) For the $S_{(0,2)}$ state the current is blocked.

The device needs to fulfill a certain condition for proper operation. The scheme requires

$$\Gamma_{T_0 \to S} \gtrsim \Gamma_{\text{left}\to\text{lead}} \gg \Gamma_{T_+ \to S}, \tag{5.1}$$

where Γ are the rates for transitions corresponding to the indices. This condition is only achievable in the easy passage configuration, while $\Gamma_{T_0 \to S}$ must be dominated by the hyperfine-induced relaxation. This implies that the described device for measuring the spin polarization works only with a GaAs double quantum dot, because the spin relaxation of a silicon dot in general, and in particular the $\Gamma_{T_0 \to S}$ rate, is never dominated by the nuclei (see Sec. 4.2.2 and 4.3.2 for details).

Final remarks Despite the long tradition of semiconductor quantum dot research, there are still many open questions. For instance, gallium arsenide is the more advanced material with regard to manufacturing techniques. All fundamental discoveries for the realization of a top-gated quantum dot qubit have been found in gallium arsenide first. The downside is certainly the unavoidable presence of nuclear spins. For a quantum computer built from gallium arsenide, it is indispensable to have an efficient way of controlling this source of decoherence. From this perspective, silicon is the better host material for a quantum dot, as it is (almost) free of nuclear spins. During the last few years, the fabrication of silicon devices has even become good enough to build few-electron quantum dots that can be used for trapping and coherently manipulating electron spins. However, the downside of silicon are the valleys of the conduction band. Without a good control of the valley splitting, undesired states may add to the qubit space which allows the system to leak into an “undefined” state. For a silicon-based quantum computer made of top-gated quantum dots, a more profound theoretical understanding and an excellent experimental control of the valley splitting is a fundamental requirement.

The work presented in this thesis can be naturally extended in several ways. For our calculations in silicon-based dots, we assumed validity of the single-valley approximation (the valley splitting is larger than any other relevant energy scale), justified because otherwise the realization of a (well-defined) qubit seems impossible. However, the nature of the valleys itself is an exceptionally interesting topic for solid state research. For a deeper understanding in general, and maybe for an operational silicon qubit even in the presence of nearby valley states, an implementation of valley coupling could be added to the numerical code and the analytical analysis.

Additionally, other dot geometries could be considered, such as a triple dot, a quantum ring, a dot inside a ring, and so on. Such an extension is straightforward because the different potentials can easily be implemented in the code. However, the enhancement toward a three-dimensional structure, and considering devices with three or more electrons, is extremely demanding, maybe impossible, for numerics using the exact diagonalization method (configuration interaction method) that we chose for our analysis. It is unlikely that we will see such calculations with a reasonable precision in the near future.

Instead of more electrons, one could think of adding a localized, magnetic impurity to the structure that the electron(s) can interact with. For instance, if the only degree of freedom of that impurity is its spin state, the Hilbert space would increase only by a factor of the order of 1. In that case, the computational demands are comparable to the electron-only problem, which can be solved in reasonable time.

With this thesis, we present an extensive study of the spin lifetime T_1. A different story is the dephasing time of a system, named T_2. An exact computation of the dephasing time is impossible for the available computing power today. Consider e.g. a gallium arsenide quantum dot with a single electron. In a quantum dot of typical size, there are roughly 10^6 nuclear spins, which affect the dynamics of the electron spin. For an exact treatment we must therefore consider the Hilbert space of 10^6 spins, which are also coupled to each other. Moreover, other sources of dephasing, i.e. charge noise, have not been included in this picture yet. It is obvious that such an approach must fail. Although there is no general relation between T_1 and T_2, the inequality $T_2 \leq 2T_1$ usually holds [22, 291]. However, the spin dephasing time is typically orders of magnitude lower than the spin lifetime, that is $T_2 \ll 2T_1$. It has been shown that for fault-tolerant quantum computation, the coherence needs to last for at least $\sim 10^5$ gate operations [292], which requires a very long coherence or fast gate operations. Thus, the overall goal is to bring the spin dephasing time as close to the spin lifetime as possible, and to have a deep understanding of the spin relaxation, which defines the upper boundary of T_2.

APPENDIX A

Numerical Method

In the present work, we use a highly accurate numerical method to obtain the eigenfunctions and energies of the single- and two-electron Hamilton operator, Eqs. (3.1) and (4.1), which are again needed to calculate the relaxation rates via Fermi's Golden Rule, Eq. (3.12). An analytical approach is possible only in a few exceptional cases. Numerics is indispensable in the case of coupled quantum dots, and, because the Coulomb interaction is comparable to the strength of the electrostatic confinement in a typical dot, for two-electron dots in general [275]. The numerical method that we use throughout this thesis was thoroughly benchmarked and discussed by Baruffa et. al. [275, 281]. For this reason, we omit to present convergence tests and benchmarks in the following. We rather give an overview of the scheme and list relevant references. On the other hand, we extend the method with an implementation of nuclear spins, which is missing in Refs. [275, 281]. We discuss the nuclear spins in more detail below.

In Chap. 3 of this thesis, we solve the Hamiltonian of Eq. (3.1) for a single-electron quantum dot. This is done in a single step, by diagonalization of the full Hamiltonian using finite differences (see below). Since this scheme is straightforward, we consider this a special case of the two-electron Hamiltonian and do not discuss it further.

In Chap. 4, we put another electron into the double dot and solve the two-electron Hamiltonian of Eq. (4.1). This is numerically much more demanding because of the increased Hilbert space. As an illustration, from N single-electron orbital wave functions (no spin) we can generate $N(N+1)/2$ symmetric and $N(N-1)/2$ antisymmetric two-electron orbital wave functions, i.e. the basis increases from N to N^2. With spin, we have $2N$ single-electron states and get $2N^2 - N$ two-electron wave functions. Thus, instead of solving the Hamiltonian in a single step, we consider a three-step approach [275, 281, 293]. First, we assume a single spinless particle, and solve the Hamiltonian $H = T + V + V_{\mathrm{E}}$, given by Eqs. (3.2), (3.3), and (4.2), using finite differences [294–

297] with the Dirichlet boundary condition [298], meaning that the wave functions are forced to be zero at the boundary. The diagonalization is carried out by the Lanczos algorithm [275, 299] with the help of the LAPACK [300] and ARPACK [301] software libraries. Second, from the single-electron wave functions calculated in the first step, we generate the two-electron wave functions as Slater determinants and permanents [279]. We take those as a basis for the quantum dot Hamiltonian of two spinless electrons, $H = \sum_{i=1,2} (T_i + V_i + V_{\mathrm{E},i}) + H_{\mathrm{C}}$, to create the matrix representation of H in that basis. For this purpose, we need to calculate the Coulomb matrix elements, which is an extensive task (see below). Finally, the Hamilton matrix is diagonalized to get the eigenstates. This procedure is referred to as the configuration interaction method [302]. In the third and last step, we add the electron spin, that is we include the Zeeman energy H_{Z}, Eq. (3.4), the spin-orbit coupling H_{so}, Eq. (3.5), and the hyperfine coupling H_{nuc}, Eq. (4.3), to the Hamiltonian. Again, we use the configuration interaction method, i.e. we write the Hamilton operator in matrix representation for the basis given by the eigenstates that we computed in the previous step. As a final result, we obtain the eigenenergies and the eigenstates of the full quantum dot system, Eq. (4.1), in high precision, assuming a sufficiently dense discretization grid, and a suitable number of basis states for the configuration interaction methods used in the second and third steps. In the present work, our discretization grid consists of typically 135 × 135 grid points, and we use the lowest 34 single-electron orbital states to generate a basis of 1156 two-electron states. Hereby, we ensure that the relative error for energies is below 10^{-5}.

In the following, we give insight into the method of finite differences, the Slater determinants, the computation of the Coulomb integrals, and the configuration interaction method. Last, we present our approach to the numerical implementation of nuclear spins.

Finite Differences In the first step of the numerical scheme, we solve the Hamiltonian for a single spinless electron using the method of finite differences [294–297]. The finite difference of a function $f(x)$ is an expression of the form $f(x + a) - f(x + b)$.[1] We can write an approximation of the first derivative of f at point x for small a with the help of a finite difference,

$$f'(x) \approx \frac{f(x+a) - f(x)}{a}. \tag{A.1}$$

In the same spirit, we can take the first derivative of $f'(x)$ and obtain

$$f''(x) \approx \frac{f(x+2a) - 2f(x+a) + f(x)}{a^2}. \tag{A.2}$$

---

[1] Here we assume a well-behaved function according to Taylor's theorem, which applies to a wave function that solves the Schrödinger equation with a realistic potential. For simplicity, we consider a one-dimensional system in this paragraph.

Equations of this type are called forward difference. The backward difference is constructed in a similar way. For numerical purposes, we use the central difference,

$$f'(x) \approx \frac{f(x+a) - f(x-a)}{2a}, \tag{A.3}$$

and

$$f''(x) \approx \frac{f(x+a) - 2f(x) + f(x-a)}{a^2}, \tag{A.4}$$

because the truncation error of this approximation is of second order in a compared to linear order for the forward or backward difference.

The Schrödinger equation in real space is solved numerically on a discrete grid, $\{x\} \to \{x_i\}$, $i \in \mathbb{N}$. Then, the Hamiltonian H becomes a matrix, and the wave function $\psi(x)$ becomes a vector, $\{\psi(x_i)\} \equiv \{\psi_i\}$. From Eqs. (A.3) and (A.4), we can easily read off the form of the first and second derivative suitable for numerics,

$$\psi_i' \approx \frac{\psi_{i+1} - \psi_{i-1}}{2h}, \tag{A.5}$$

and

$$\psi_i'' \approx \frac{\psi_{i+1} - 2\psi_i + \psi_{i-1}}{h^2}, \tag{A.6}$$

where h is the distance between two grid points. This allows us to find the matrix representation of the momentum operator, as present in the kinetic energy. We can construct now the Hamiltonian matrix of the system, noting that the position operator of the potential term in matrix representation is diagonal.

The grid dimensions for the computation must be finite, which requires that we introduce a boundary. A good choice of boundary conditions for confined systems is a vanishing wave function along the edge of the grid, referred to as the Dirichlet boundary condition [298]. Note that we must choose a grid which is large enough to cover the main region of the potential. The boundary should be such that a continuous wave function is negligible where we define the edge. Obviously, a larger grid reduces the error, but raises the computational demands. Similarly, a higher grid point density (small h) gives better results, but the computational time increases.

We can now compute the eigenenergies of the system by diagonalization of the Hamilton matrix. The eigenvectors of the matrix are the eigenstates of the system in real space, defined on the grid. These states are used further in the next steps.

Slater Determinants and Permanents The Slater determinant [279] is a handy aid to memory for the construction of fully antisymmetrized fermionic many-particle wave functions. The equivalent for bosonic wave functions is the Slater permanent [279]. We present here both in short.

For a given many-particle wave function $|i_1 i_2 i_3 \dots\rangle$, where the j-th particle is in state $|i_j\rangle$, we can write a transposition $P_{\alpha\beta}$ such that

$$P_{\alpha\beta}|i_1 i_2 i_3 \dots i_\alpha \dots i_\beta \dots\rangle = |i_1 i_2 i_3 \dots i_\beta \dots i_\alpha \dots\rangle. \tag{A.7}$$

An arbitrary permutation $\mathcal{P}_{\alpha_1\alpha_2\alpha_3\dots}$ of single-particle states, where

$$\mathcal{P}_{\alpha_1\alpha_2\alpha_3\dots}|i_1 i_2 i_3 \dots\rangle = |i_{\alpha_1} i_{\alpha_2} i_{\alpha_3} \dots\rangle, \tag{A.8}$$

can be written as a sequence of transpositions, say $\mathcal{P}_{\alpha_1\alpha_2\alpha_3\dots} = P_{\alpha\beta}P_{\gamma\delta}\dots$, according to the properties of the permutation group [163, 303]. Let $|\mathcal{P}|$ be the number of transpositions in the decomposition of $\mathcal{P}$, then

$$S_\pm = \frac{1}{\sqrt{N!}} \sum_{\mathcal{P}} (\pm 1)^{|\mathcal{P}|} \mathcal{P} \tag{A.9}$$

is the operator of total symmetrization (+) and antisymmetrization (−). Hence, the state $S_-|i_1 i_2 i_3 \dots\rangle$ is a proper, normalized many-particle state of fermions, and analogously for bosons, $S_+|i_1 i_2 i_3 \dots\rangle$. For instance, for two electrons in state $|i_1\rangle$ and $|i_2\rangle$ respectively, the antisymmetrized wave function reads as $S_-|i_1 i_2\rangle = (|i_1 i_2\rangle - |i_2 i_1\rangle)/\sqrt{2}$.

A totally antisymmetric state of N fermions can also be written using a determinant,

$$\frac{1}{\sqrt{N!}} \begin{vmatrix} |i_1\rangle_{(1)} & |i_2\rangle_{(1)} & \cdots & |i_N\rangle_{(1)} \\ |i_1\rangle_{(2)} & |i_2\rangle_{(2)} & \cdots & |i_N\rangle_{(2)} \\ \vdots & \vdots & \ddots & \vdots \\ |i_1\rangle_{(N)} & |i_2\rangle_{(N)} & \cdots & |i_N\rangle_{(N)} \end{vmatrix} = S_-|i_1 i_2 \dots i_N\rangle, \tag{A.10}$$

where $|i_j\rangle_{(k)}$ denotes the state of the k-th electron. The left hand side of Eq. (A.10) is called the Slater determinant. Similarly, we can write the totally symmetric state of N bosons with the help of a permanent,

$$\frac{1}{\sqrt{n_1! n_2! \dots}\sqrt{N!}} \begin{vmatrix} |i_1\rangle_{(1)} & |i_2\rangle_{(1)} & \cdots & |i_N\rangle_{(1)} \\ |i_1\rangle_{(2)} & |i_2\rangle_{(2)} & \cdots & |i_N\rangle_{(2)} \\ \vdots & \vdots & \ddots & \vdots \\ |i_1\rangle_{(N)} & |i_2\rangle_{(N)} & \cdots & |i_N\rangle_{(N)} \end{vmatrix}_+ = S_+|i_1 i_2 i_3 \dots i_N\rangle. \tag{A.11}$$

Note the additional normalization factor $(n_1! n_2! \dots)^{-1/2}$, where n_i gives the occupation number of state $|i\rangle$. The object on the left hand side of Eq. (A.11) is called the Slater permanent.

Coulomb Integrals In the second step of our numerical scheme, we create the matrix representation of the Hamiltonian in the basis of the two-electron states generated with the help of Slater determinants. For this purpose, we need to calculate all matrix elements of the Hamiltonian for the given basis, which is numerically demanding because of the Coulomb interaction, Eq. (4.5). Note that for $\sim N$ single electron states, we get $\mathcal{O}(N^2)$ two-electron states, resulting in $\mathcal{O}(N^4)$ Coulomb elements that we need to compute [275, 281]. They read as

$$\langle i|H_\mathrm{C}|j\rangle = \frac{e^2}{4\pi\varepsilon}\int \mathrm{d}\boldsymbol{r}_1 \int \mathrm{d}\boldsymbol{r}_2 \Psi_i^*(\boldsymbol{r}_1,\boldsymbol{r}_2)\frac{1}{|\mathbf{r}_1-\mathbf{r}_2|}\Psi_j(\boldsymbol{r}_1,\boldsymbol{r}_2), \tag{A.12}$$

where $\langle \boldsymbol{r}_1\boldsymbol{r}_2|i\rangle = \Psi_i(\boldsymbol{r}_1,\boldsymbol{r}_2)$ and $\langle \boldsymbol{r}_1\boldsymbol{r}_2|j\rangle = \Psi_j(\boldsymbol{r}_1,\boldsymbol{r}_2)$ are the (anti)symmetrized two-electron orbital wave functions created before. Equation (A.12) is defined in two dimensions. If we considered a finite width along the growth direction z, the Coulomb energies would become smaller by up to several percent. This is inevitable unless we use a full three-dimensional calculation, which is a desperate numerical challenge. Fortunately, the error of the approximation of Eq. (A.12) is suppressed for double quantum dots if the electrons are located in different dots. Further, we can improve our results by slightly adjusting the confinement length and the interdot distance. In any case, the two-dimensional approximation remains qualitatively valid because the symmetry of the system stays the same, and we stick to it throughout this thesis. More details on this issue can be found in Ref. [275].

In order to solve Eq. (A.12) numerically, we perform a discrete Fourier transformation [304]. In the numerics, we use the “Fastest Fourier Transform in the West” (FFTW) software library [305] together with a correction factor [275, 306]. The Fourier transform of the wave functions’ components is expressed by a Taylor series, and the remaining integrals can be computed analytically [275, 281]. Then, only the derivatives of the Taylor expansion need to be computed numerically, which can be done with high accuracy [307]. A detailed discussion about the numerical precision of the Coulomb integrals is given in Ref. [275].

Configuration Interaction Method In the configuration interaction method [302], the eigenstates of a given system are calculated by means of a chosen basis. If we work with a reduced basis, the solutions will be an approximation. The number of basis states needed for accurate results strongly depends on the choice of basis functions. In our case, we consider more than a thousand states. As a basis in the second step of the numerical scheme, we use the Slater determinants generated from the single-particle states which we calculate in the first step. The solution of the second step is then taken as a basis for the third step, where we diagonalize the full Hamiltonian, Eq. (4.1).

The configuration interaction method is a highly accurate numerical approach, which can be applied to many systems. Yet, the main idea is very simple. From the time-independent Schrödinger equation,

$$H|\phi\rangle = E|\phi\rangle, \tag{A.13}$$

we can read off the matrix representation of H in the basis $\{|\psi_j\rangle\}$, writing

$$\sum_j \langle\psi_i|H|\psi_j\rangle\langle\psi_j|\phi\rangle = E\langle\psi_i|\phi\rangle, \tag{A.14}$$

and $H_{ij} = \langle\psi_i|H|\psi_j\rangle$. To proceed, we need to compute all matrix elements H_{ij}, which implies the Coulomb integrals (see above). After the diagonalization of the matrix of H, we obtain the eigenenergies and eigenstates of the system in terms of the chosen basis,

$$|\phi\rangle = \sum_i \langle\psi_i|\phi\rangle|\psi_i\rangle. \tag{A.15}$$

Obviously, if $\{|\psi_j\rangle\}$ is not a complete basis of the full Hilbert space, Eq. (A.15) cannot be valid in general. However, if we are interested only in the states at the bottom of the energy spectrum, we can find a reduced basis where the matrix elements $\langle\psi_k|\phi\rangle$ of the omitted basis states and the eigenstates of interest are zero or negligible. In general, a larger basis leads to better results. The limits to the maximal number of basis states are set by the computational power. In our case, a two-dimensional system of two confined electrons, a reasonable basis can be chosen such that the eigenstates can be computed with very high accuracy.

Numerical Formula of Hyperfine Coupling Let us now discuss the numerical implementation of the nuclear spins.[2] Since our numerical approach is based on space discretization (the method of finite differences), we need to derive a discretized form of the Hamiltonian in Eq. (4.3). We comment on the calculation of hyperfine-enabled relaxation rates at the end of this paragraph.

Consider a basic element of the spatial grid, a rectangular box with lateral dimensions h_x and h_y. Such volume elements are labeled by the index $k = 1, ..., M$, where M is the total amount of boxes of the grid. In the two-dimensional approximation one assumes that the electron wave function along the z direction is fixed to $\psi_0(z)$. In this work, we assume the ground state of a hard-wall confinement of width $w = 11$ nm.

We can write the matrix representation of the operator H_{nuc}, Eq. (4.3), in the basis of the discretized space, with matrix elements

$$(H_{\text{nuc}})_{kk'} = \langle k, \psi_0|H_{\text{nuc}}|k', \psi_0\rangle. \tag{A.16}$$

The function $|k\rangle$ represents a projection on the xy-plane of the box with label k. In other words, $\langle\boldsymbol{r}|k\rangle$ is $1/\sqrt{h_x h_y}$ inside the k-th box and zero everywhere else. Note that the basis functions $|k\rangle$ are orthonormal, i.e. $\langle k|k'\rangle = \delta_{kk'}$. For the δ-function in H_{nuc}, the projection reads as

---

[2] Parts of this paragraph are based on Raith et. al., *Theory of Spin Relaxation in Two-Electron Lateral Coupled Quantum Dots*, Phys. Rev. Lett. 108, 246602 (2012) [153].

$$\langle k, \psi_0|\delta(\mathbf{R}-\mathbf{R}_n)|k', \psi_0\rangle = \begin{cases} \delta_{kk'}|\psi_0(z_n)|^2/h_x h_y, & \text{if } n \in k, \\ 0 & \text{otherwise .} \end{cases} \tag{A.17}$$

Then, Eq. (A.16) is given by

$$(H_{\mathrm{nuc}})_{kk'} = \delta_{kk'}(\beta/v_0)\sum_{n\in k} v_0 \mathbf{I}_n \cdot \boldsymbol{\sigma}|\psi_0(z_n)|^2/h_x h_y, \tag{A.18}$$

where we introduce the nuclei volume density $1/v_0$. We now replace the sum over (typically many) nuclear spins by an effective spin $\boldsymbol{\mathcal{I}}$ and get the discretized form of the Hamiltonian as

$$(H_{\mathrm{nuc}})_{kk'} = \delta_{kk'}(\beta/v_0)\boldsymbol{\mathcal{I}}_k \cdot \boldsymbol{\sigma}. \tag{A.19}$$

By the central limit theorem [307], the effective spins are completely described by their average and dispersion, which follow from the corresponding characteristics of the nuclear spin ensemble. For random unpolarized nuclear spins, which we consider, it holds

$$\begin{aligned} \langle \mathbf{I}_n \rangle &= 0, \\ \langle \mathbf{I}_n \cdot \mathbf{I}_m \rangle &= \delta_{nm} I(I+1), \end{aligned} \tag{A.20}$$

so that the effective spins have zero average and the following dispersion

$$\langle \boldsymbol{\mathcal{I}}_k \cdot \boldsymbol{\mathcal{I}}_{k'} \rangle = \delta_{kk'} I(I+1)/N. \tag{A.21}$$

Here, $N = h_x h_y h_z/v_0$ is the number of nuclei in the grid volume element, where the effective extension along z is defined by the wave function profile [278], given in Eq. (4.4). For the hard-wall potential we get $h_z = 2w/3$.

To calculate relaxation rates, we average Γ_{ij}, Eq. (3.12), over typically 50 configurations of nuclear ensembles. A single such configuration is parametrized by a set of effective spins, $\{\boldsymbol{\mathcal{I}}_k\}$, drawn from a random Gaussian ensemble described by Eq. (A.21), for which we diagonalize the two-electron Hamiltonian. Having the two-electron spectrum allows us to calculate the matrix elements M_{ij} and energy differences E_{ij}, which enter the relaxation rates Γ_{ij} in Eq. (3.12).

Bibliography

[1] Behar, R. *Who Invented Microprocessors?* (Retrieved April, 2013). URL `http://www.time.com/time/magazine/article/0,9171,155487,00.html`.

[2] Moore, G. E. *Cramming more components onto integrated circuits.* Electronics **38**, 8 (1965).

[3] Dell, M., Mora, G., Howard, J. & Kleinrock, L. *Will Moore's Law eventually collapse?* (Retrieved April, 2013). URL `http://curiosity.discovery.com/question/moores-law-collapse`.

[4] Theis, T. & Solomon, P. *In Quest of the "Next Switch": Prospects for Greatly Reduced Power Dissipation in a Successor to the Silicon Field-Effect Transistor.* Proceedings, IEEE **98**, 2005 (2010).

[5] Bennett, C. H. & DiVincenzo, D. P. *Quantum information and computation.* Nature **404**, 247 (2000).

[6] Aaronson, S. *Shor, I'll do it* (Retrieved April, 2013). URL `http://www.scottaaronson.com/blog/?p=208`.

[7] Feynman, R. P. *Simulating Physics with Computers.* Int. J. Theor. Phys. **21**, 467 (1982).

[8] Deutsch, D. & Jozsa, R. *Rapid Solution of Problems by Quantum Computation.* Proceedings, RSL **439**, 553 (1992).

[9] Cleve, R., Ekert, A., Macchiavello, C. & Mosca, M. *Quantum algorithms revisited.* Proceedings, RSL **454**, 339 (1998).

[10] Shor, P. *Algorithms for quantum computation: discrete logarithms and factoring.* IEEE Comput. Soc. Press **35**, 124 (1994).

[11] Koblitz, N. *A Course in Number Theory and Cryptography* (Springer, 1994), 2nd edn.

[12] Grover, L. K. *A fast quantum mechanical algorithm for database search.* Proceedings, STOC **28**, 212 (1996).

[13] Grover, L. K. *From Schrödinger's equation to the quantum search algorithm.* Pramana **56**, 333 (2001).

[14] Fayyad, U., Piatetsky-shapiro, G. & Smyth, P. *From Data Mining to Knowledge Discovery in Databases.* AI Magazine **17**, 37 (1996).

[15] Zalka, C. *Grover's quantum searching algorithm is optimal.* Phys. Rev. A **60**, 2746 (1999).

[16] Bennett, C., Bernstein, E., Brassard, G. & Vazirani, U. *Strengths and Weaknesses of Quantum Computing.* SIAM Journal on Computing **26**, 1510 (1997).

[17] Jordan, S. *Algebraic and Number Theoretic Algorithms* (Retrieved April, 2013). URL `http://math.nist.gov/quantum/zoo/`.

[18] DiVincenzo, D. P. *The Physical Implementation of Quantum Computation.* Fortschr. Phys. **48**, 771 (2000).

[19] Ladd, T. D., Jelezko, F., Laflamme, R., Nakamura, Y., Monroe, C. & O'Brien, J. L. *Quantum computers.* Nature **464**, 45 (2010).

[20] Gottesman, D. *An Introduction to Quantum Error Correction and Fault-Tolerant Quantum Computation.* arXiv:0904.2557 (unpublished).

[21] Wolf, S. A. *et al. Spintronics: A Spin-Based Electronics Vision for the Future.* Science **294**, 1488 (2001).

[22] Žutić, I., Fabian, J. & Das Sarma, S. *Spintronics: fundamentals and applications.* Rev. Mod. Phys. **76**, 323 (2004).

[23] Fabian, J., Matos-Abiague, A., Ertler, C., Stano, P. & Žutić, I. *Semiconductor spintronics.* Acta Phys. Slov. **57**, 565 (2007).

[24] Baibich, M. N. *et al. Giant Magnetoresistance of (001)Fe/(001)Cr Magnetic Superlattices.* Phys. Rev. Lett. **61**, 2472 (1988).

[25] Binasch, G., Grünberg, P., Saurenbach, F. & Zinn, W. *Enhanced magnetoresistance in layered magnetic structures with antiferromagnetic interlayer exchange.* Phys. Rev. B **39**, 4828 (1989).

[26] Shulman, M. D., Dial, O. E., Harvey, S. P., Bluhm, H., Umansky, V. & Yacoby, A. *Demonstration of Entanglement of Electrostatically Coupled Singlet-Triplet Qubits.* Science **336**, 202 (2012).

[27] Kloeffel, C. & Loss, D. *Prospects for Spin-Based Quantum Computing in Quantum Dots.* Annu. Rev. Condens. Matter Phys. **4**, 51 (2013).

[28] Nielsen, M. A. & Chuang, I. L. *Quantum Computation and Quantum Information* (Cambridge University Press, Cambridge, 2000).

[29] Hanson, R. & Awschalom, D. D. *Coherent manipulation of single spins in semiconductors.* Nature **453**, 1043 (2008).

[30] Awschalom, D. D., Bassett, L. C., Dzurak, A. S., Hu, E. L. & Petta, J. R. *Quantum Spintronics: Engineering and Manipulating Atom-Like Spins in Semiconductors.* Science **339**, 1174 (2013).

[31] Politi, A., Matthews, J. C. F. & O'Brien, J. L. *Shor's Quantum Factoring Algorithm on a Photonic Chip.* Science **325**, 1221 (2009).

[32] Knill, E., Laflamme, R. & Milburn, G. J. *A scheme for efficient quantum computation with linear optics.* Nature **409**, 46 (2001).

[33] Beige, A., Huelga, S., Knight, P., Plenio, M. & Thomson, R. *Coherent manipulation of two dipole-dipole interacting ions.* J. Mod. Opt. **47**, 401 (2000).

[34] Häffner, H., Roos, C. & Blatt, R. *Quantum computing with trapped ions.* Physics Reports **469**, 155 (2008).

[35] Cirac, J. I. & Zoller, P. *A scalable quantum computer with ions in an array of microtraps.* Nature **404**, 579 (2000).

[36] Blatt, R. & Roos, C. F. *Quantum simulations with trapped ions.* Nat. Phys. **8**, 277 (2012).

[37] Monroe, C. & Kim, J. *Scaling the Ion Trap Quantum Processor.* Science **339**, 1164 (2013).

[38] Brennen, G. K., Caves, C. M., Jessen, P. S. & Deutsch, I. H. *Quantum Logic Gates in Optical Lattices.* Phys. Rev. Lett. **82**, 1060 (1999).

[39] Jaksch, D., Briegel, H.-J., Cirac, J. I., Gardiner, C. W. & Zoller, P. *Entanglement of Atoms via Cold Controlled Collisions.* Phys. Rev. Lett. **82**, 1975 (1999).

[40] Briegel, H.-J., Calarco, T., Jaksch, D., Cirac, J. I. & Zoller, P. *Quantum computing with neutral atoms.* J. Mod. Opt. **47**, 415 (2000).

[41] Ahn, J., Weinacht, T. C. & Bucksbaum, P. H. *Information Storage and Retrieval Through Quantum Phase.* Science **287**, 463 (2000).

[42] Wineland, D., Monroe, C., Itano, W., Leibfried, D., King, B. *et al. Experimental issues in coherent quantum state manipulation of trapped atomic ions.* J. Res. Natl. Inst. Stand. Technol. **103**, 259 (1998).

[43] Häffner, H. *et al. Scalable multiparticle entanglement of trapped ions.* Nature **438**, 643 (2005).

[44] Blatt, R. & Wineland, D. *Entangled states of trapped atomic ions.* Nature **453**, 1008 (2008).

[45] Urban, E., Johnson, T. A., Henage, T., Isenhower, L., Yavuz, D. D., Walker, T. G. & Saffman, M. *Observation of Rydberg blockade between two atoms.* Nat. Phys. **5**, 110 (2009).

[46] Gaëtan, A. *et al. Observation of collective excitation of two individual atoms in the Rydberg blockade regime.* Nat. Phys. **5**, 115 (2009).

[47] Makhlin, Y., Schön, G. & Shnirman, A. *Quantum-state engineering with Josephson-junction devices.* Rev. Mod. Phys. **73**, 357 (2001).

[48] Devoret, M. H. & Schoelkopf, R. J. *Superconducting Circuits for Quantum Information: An Outlook.* Science **339**, 1169 (2013).

[49] Yu, Y., Han, S., Chu, X., Chu, S.-I. & Wang, Z. *Coherent Temporal Oscillations of Macroscopic Quantum States in a Josephson Junction.* Science **296**, 889 (2002).

[50] Schreier, J. A. *et al. Suppressing charge noise decoherence in superconducting charge qubits.* Phys. Rev. B **77**, 180502 (2008).

[51] Nakamura, Y., Pashkin, Y. A. & Tsai, J. S. *Coherent control of macroscopic quantum states in a single-Cooper-pair box.* Nature **398**, 786 (1999).

[52] Vion, D. *et al. Manipulating the Quantum State of an Electrical Circuit.* Science **296**, 886 (2002).

[53] Pashkin, Y. A., Yamamoto, T., Astafiev, O., Nakamura, Y., Averin, D. V. & Tsai, J. S. *Quantum oscillations in two coupled charge qubits.* Nature **421**, 823 (2003).

[54] Yamamoto, T., Pashkin, Y. A., Astafiev, O., Nakamura, Y. & Tsai, J. S. *Demonstration of conditional gate operation using superconducting charge qubits.* Nature **425**, 941 (2003).

[55] Chiorescu, I., Nakamura, Y., Harmans, C. J. P. M. & Mooij, J. E. *Coherent Quantum Dynamics of a Superconducting Flux Qubit.* Science **299**, 1869 (2003).

[56] Martinis, J. M., Nam, S., Aumentado, J. & Urbina, C. *Rabi Oscillations in a Large Josephson-Junction Qubit.* Phys. Rev. Lett. **89**, 117901 (2002).

[57] DiCarlo, L. *et al. Demonstration of two-qubit algorithms with a superconducting quantum processor.* Nature **460**, 240 (2009).

[58] Preskill, J. *Fault-tolerant quantum computation.* arXiv:quant-ph/9712048 (unpublished).

[59] Niskanen, A. O., Harrabi, K., Yoshihara, F., Nakamura, Y., Lloyd, S. & Tsai, J. S. *Quantum Coherent Tunable Coupling of Superconducting Qubits.* Science **316**, 723 (2007).

[60] Awschalom, D. D., Epstein, R. & Hanson, R. *The Diamond Age of Spintronics.* Scientific American **297**, 84 (2007).

[61] Reynhardt, E. C., High, G. L. & van Wyk, J. A. *Temperature dependence of spin-spin and spin-lattice relaxation times of paramagnetic nitrogen defects in diamond.* J. Chem. Phys. **109**, 8471 (1998).

[62] Takahashi, S., Hanson, R., van Tol, J., Sherwin, M. S. & Awschalom, D. D. *Quenching Spin Decoherence in Diamond through Spin Bath Polarization.* Phys. Rev. Lett. **101**, 047601 (2008).

[63] Jelezko, F., Popa, I., Gruber, A., Tietz, C., Wrachtrup, J., Nizovtsev, A. & Kilin, S. *Single spin states in a defect center resolved by optical spectroscopy.* Appl. Phys. Lett. **81**, 2160 (2002).

[64] Jelezko, F., Gaebel, T., Popa, I., Gruber, A. & Wrachtrup, J. *Observation of Coherent Oscillations in a Single Electron Spin.* Phys. Rev. Lett. **92**, 076401 (2004).

[65] Jelezko, F., Gaebel, T., Popa, I., Domhan, M., Gruber, A. & Wrachtrup, J. *Observation of Coherent Oscillation of a Single Nuclear Spin and Realization of a Two-Qubit Conditional Quantum Gate.* Phys. Rev. Lett. **93**, 130501 (2004).

[66] Gaebel, T. *et al. Room-temperature coherent coupling of single spins in diamond.* Nat. Phys. **2**, 408 (2006).

[67] Hanson, R., Mendoza, F. M., Epstein, R. J. & Awschalom, D. D. *Polarization and Readout of Coupled Single Spins in Diamond.* Phys. Rev. Lett. **97**, 087601 (2006).

[68] Childress, L. *et al. Coherent Dynamics of Coupled Electron and Nuclear Spin Qubits in Diamond.* Science **314**, 281 (2006).

[69] Dutt, M. V. G. *et al.* *Quantum Register Based on Individual Electronic and Nuclear Spin Qubits in Diamond.* Science **316**, 1312 (2007).

[70] Santori, C. *et al.* *Coherent Population Trapping of Single Spins in Diamond under Optical Excitation.* Phys. Rev. Lett. **97**, 247401 (2006).

[71] Kane, B. E. *A silicon-based nuclear spin quantum computer.* Nature **393**, 133 (1998).

[72] Vrijen, R. *et al.* *Electron-spin-resonance transistors for quantum computing in silicon-germanium heterostructures.* Phys. Rev. A **62**, 012306 (2000).

[73] Skinner, A. J., Davenport, M. E. & Kane, B. E. *Hydrogenic Spin Quantum Computing in Silicon: A Digital Approach.* Phys. Rev. Lett. **90**, 87901 (2003).

[74] Pla, J. J. *et al.* *A single-atom electron spin qubit in silicon.* Nature **489**, 541 (2012).

[75] Gordon, J. P. & Bowers, K. D. *Microwave Spin Echoes from Donor Electrons in Silicon.* Phys. Rev. Lett. **1**, 368 (1958).

[76] Tyryshkin, A. M., Lyon, S. A., Astashkin, A. V. & Raitsimring, A. M. *Electron spin relaxation times of phosphorus donors in silicon.* Phys. Rev. B **68**, 193207 (2003).

[77] Tyryshkin, A. M. *et al.* *Electron spin coherence exceeding seconds in high-purity silicon.* Nat. Mater. **11**, 143 (2012).

[78] Ladd, T. D., Maryenko, D., Yamamoto, Y., Abe, E. & Itoh, K. M. *Coherence time of decoupled nuclear spins in silicon.* Phys. Rev. B **71**, 014401 (2005).

[79] The University of Manchester. *Graphene: Future Applications* (Retrieved April, 2013). URL `http://www.graphene.manchester.ac.uk/future/`.

[80] Lin, Y.-M., Dimitrakopoulos, C., Jenkins, K. A., Farmer, D. B., Chiu, H.-Y., Grill, A. & Avouris, P. *100-GHz Transistors from Wafer-Scale Epitaxial Graphene.* Science **327**, 662 (2010).

[81] Wu, Y. *et al.* *High-frequency, scaled graphene transistors on diamond-like carbon.* Nature **472**, 74 (2011).

[82] Trauzettel, B., Bulaev, D. V., Loss, D. & Burkard, G. *Spin qubits in graphene quantum dots.* Nat. Phys. **3**, 192 (2007).

[83] Recher, P. & Trauzettel, B. *Quantum dots and spin qubits in graphene.* Nanotechnology **21**, 302001 (2010).

[84] Calogeracos, A. & Dombey, N. *History and physics of the Klein paradox.* Contemp. Phys. **40**, 313 (1999).

[85] Abergel, D., Apalkov, V., Berashevich, J., Ziegler, K. & Chakraborty, T. *Properties of graphene: a theoretical perspective.* Adv. Phys. **59**, 261 (2010).

[86] Castro Neto, A. H., Guinea, F., Peres, N. M. R., Novoselov, K. S. & Geim, A. K. *The electronic properties of graphene.* Rev. Mod. Phys. **81**, 109 (2009).

[87] Chakraborty, T. *Quantum Dots* (Elsevier, 1999), 1st edn.

[88] Reimann, S. M. & Manninen, M. *Electronic structure of quantum dots.* Rev. Mod. Phys. **74**, 1283 (2002).

[89] Cerletti, V., Coish, W. A., Gywat, O. & Loss, D. *Recipes for spin-based quantum computing.* Nanotechnology **16**, R27 (2005).

[90] Zak, R. A., Röthlisberger, B., Chesi, S. & Loss, D. *Quantum Computing with Electron Spins in Quantum Dots.* arXiv:0906.4045 (unpublished).

[91] Bera, D., Qian, L., Tseng, T.-K. & Holloway, P. H. *Quantum Dots and Their Multimodal Applications: A Review.* Materials **3**, 2260 (2010).

[92] Bimberg, D. *Der Zoo der Quantenpunkte.* Physik Journal **09**, 43 (2006).

[93] Buckley, S., Rivoire, K. & Vučković, J. *Engineered quantum dot single-photon sources.* Reports on Progress in Physics **75**, 126503 (2012).

[94] Stangl, J., Holý, V. & Bauer, G. *Structural properties of self-organized semiconductor nanostructures.* Rev. Mod. Phys. **76**, 725 (2004).

[95] Wang, Z. M. *Self-Assembled Quantum Dots* (Springer, NY, 2008), 1st edn.

[96] Hanson, R., Kouwenhoven, L. P., Petta, J. R., Tarucha, S. & Vandersypen, L. M. K. *Spins in few-electron quantum dots.* Rev. Mod. Phys. **79**, 1217 (2007).

[97] Schneider, C. *et al. Lithographic alignment to site-controlled quantum dots for device integration.* Appl. Phys. Lett. **92**, 183101 (2008).

[98] Stalford, H. L., Young, R., Nordberg, E. P., Levy, J. E., Borras Pinilla, C. & Carroll, M. S. *Capacitance modeling of complex topographical silicon quantum dot structures.* arXiv:0911.3670 (unpublished).

[99] Burkard, G. *Spin coherence and entanglement in nanostructures* (Retrieved April, 2013). URL `http://thp.uni-due.de/~koenig/DPG_School_10/Burkard.pdf`.

[100] Loss, D. & DiVincenzo, D. P. *Quantum computation with quantum dots.* Phys. Rev. A **57**, 120 (1998).

[101] Koppens, F. H. L. *et al. Driven coherent oscillations of a single electron spin in a quantum dot.* Nature **442**, 766 (2006).

[102] Nowack, K. C., Koppens, F. H. L., Nazarov, Y. V. & Vandersypen, L. M. K. *Coherent Control of a Single Electron Spin with Electric Fields.* Science **318**, 1430 (2007).

[103] Levy, J. *Universal Quantum Computation with Spin*-1/2 *Pairs and Heisenberg Exchange.* Phys. Rev. Lett. **89**, 147902 (2002).

[104] Petta, J. R. *et al. Coherent manipulation of coupled electron spins in semiconductor quantum dots.* Science **309**, 2180 (2005).

[105] Taylor, J. M., Engel, H.-A., Dur, W., Yacoby, A., Marcus, C. M., Zoller, P. & Lukin, M. D. *Fault-tolerant architecture for quantum computation using electrically controlled semiconductor spins.* Nat. Phys. **1**, 177 (2005).

[106] Hanson, R. & Burkard, G. *Universal set of quantum gates for double-dot spin qubits with fixed interdot coupling.* Phys. Rev. Lett. **98**, 050502 (2007).

[107] Hu, X. & Das Sarma, S. *Hilbert-space structure of a solid-state quantum computer: Two-electron states of a double-quantum-dot artificial molecule.* Phys. Rev. A **61**, 062301 (2000).

[108] Burkard, G. *Spin-entangled electrons in solid-state systems.* J. Phys.: Condens. Matter **19**, 233202 (2007).

[109] Fabian, J. & Hohenester, U. *Entanglement distillation by adiabatic passage in coupled quantum dots.* Phys. Rev. B **72**, 201304 (2005).

[110] Brunner, R. *et al. Two-Qubit Gate of Combined Single-Spin Rotation and Interdot Spin Exchange in a Double Quantum Dot.* Phys. Rev. Lett. **107**, 146801 (2011).

[111] Barenco, A. *et al. Elementary gates for quantum computation.* Phys. Rev. A **52**, 3457 (1995).

[112] Taylor, J. M., Petta, J. R., Johnson, A. C., Yacoby, A., Marcus, C. M. & Lukin, M. D. *Relaxation, dephasing, and quantum control of electron spins in double quantum dots.* Phys. Rev. B **76**, 035315 (2007).

[113] Laird, E. A., Barthel, C., Rashba, E. I., Marcus, C. M., Hanson, M. P. & Gossard, A. C. *Hyperfine-Mediated Gate-Driven Electron Spin Resonance.* Phys. Rev. Lett. **99**, 246601 (2007).

[114] Pioro-Ladriere, M. *et al. Electrically driven single-electron spin resonance in a slanting Zeeman field.* Nat. Phys. **4**, 776 (2008).

[115] Meunier, T., Calado, V. E. & Vandersypen, L. M. K. *Efficient controlled-phase gate for single-spin qubits in quantum dots.* Phys. Rev. B **83**, 121403 (2011).

[116] Foletti, S., Bluhm, H., Mahalu, D., Umansky, V. & Yacoby, A. *Universal quantum control of two-electron spin quantum bits using dynamic nuclear polarization.* Nat. Phys. **5**, 903 (2009).

[117] Gustavsson, S. *et al. Counting statistics and super-Poissonian noise in a quantum dot: Time-resolved measurements of electron transport.* Phys. Rev. B **74**, 195305 (2006).

[118] Shaji, N. *et al. Spin blockade and lifetime-enhanced transport in a few-electron Si/SiGe double quantum dot.* Nat. Phys. **4**, 540 (2008).

[119] Zwanenburg, F. A. *et al. Ultrasmall silicon quantum dots.* J. Appl. Phys. **105**, 124314 (2009).

[120] Lim, W. H. *et al. Electrostatically defined few-electron double quantum dot in silicon.* Appl. Phys. Lett. **94**, 173502 (2009).

[121] Nordberg, E. P. *et al. Enhancement-mode double-top-gated metal-oxide-semiconductor nanostructures with tunable lateral geometry.* Phys. Rev. B **80**, 115331 (2009).

[122] Liu, H. W., Fujisawa, T., Ono, Y., Inokawa, H., Fujiwara, A., Takashina, K. & Hirayama, Y. *Pauli-spin-blockade transport through a silicon double quantum dot.* Phys. Rev. B **77**, 073310 (2008).

[123] Xiang, Y., Lee, W., Nielsch, K., Abstreiter, G. & Fontcuberta i Morral, A. *Microstructured horizontal alumina pore arrays as growth templates for large area few and single nanowire devices.* Phys. Status Solidi RRL **2**, 59 (2008).

[124] Wild, A., Sailer, J., Nützel, J., Abstreiter, G., Ludwig, S. & Bougeard, D. *Electrostatically defined quantum dots in a Si/SiGe heterostructure.* New J. Phys. **12**, 113019 (2010).

[125] Borselli, M. G. *et al. Pauli spin blockade in undoped Si/SiGe two-electron double quantum dots.* Appl. Phys. Lett. **99**, 063109 (2011).

[126] Prance, J. R. *et al. Single-Shot Measurement of Triplet-Singlet Relaxation in a Si/SiGe Double Quantum Dot.* Phys. Rev. Lett. **108**, 046808 (2012).

[127] Maune, B. M. *et al. Coherent singlet-triplet oscillations in a silicon-based double quantum dot.* Nature **481**, 344 (2012).

[128] Yang, C. H. *et al. Spin-valley lifetimes in a silicon quantum dot with tunable valley splitting.* arxiv:1302.0983 (unpublished).

[129] Simmons, C. B. *et al. Tunable Spin Loading and* T_1 *of a Silicon Spin Qubit Measured by Single-Shot Readout.* Phys. Rev. Lett. **106**, 156804 (2011).

[130] Khaetskii, A. V. & Nazarov, Y. V. *Spin-flip transitions between Zeeman sublevels in semiconductor quantum dots.* Phys. Rev. B **64**, 125316 (2001).

[131] Schliemann, J., Khaetskii, A. & Loss, D. *Electron spin dynamics in quantum dots and related nanostructures due to hyperfine interaction with nuclei.* J. Phys: Condens. Matter **15**, R1809 (2003).

[132] Schliemann, J. *Spins coupled to a spin bath: From integrability to chaos.* Phys. Rev. B **81**, 081301 (2010).

[133] Johnson, A. C. *et al. Triplet-singlet spin relaxation via nuclei in a double quantum dot.* Nature **435**, 925 (2005).

[134] Koppens, F. H. L., Nowack, K. C. & Vandersypen, L. M. K. *Spin Echo of a Single Electron Spin in a Quantum Dot.* Phys. Rev. Lett. **100**, 236802 (2008).

[135] de Sousa, R. *Electron Spin as a Spectrometer of Nuclear-Spin Noise and Other Fluctuations.* Top. Appl. Phys. **115**, 183 (2009).

[136] Winter, M. *WebElements: the periodic table on the web* (Retrieved April, 2013). URL `http://www.webelements.com`.

[137] Petta, J. R. *et al. Dynamic Nuclear Polarization with Single Electron Spins.* Phys. Rev. Lett. **100**, 067601 (2008).

[138] Rudner, M. S. & Levitov, L. S. *Electrically Driven Reverse Overhauser Pumping of Nuclear Spins in Quantum Dots.* Phys. Rev. Lett. **99**, 246602 (2007).

[139] Imamoglu, A., Knill, E., Tian, L. & Zoller, P. *Optical Pumping of Quantum-Dot Nuclear Spins.* Phys. Rev. Lett. **91**, 017402 (2003).

[140] Stepanenko, D., Burkard, G., Giedke, G. & Imamoglu, A. *Enhancement of Electron Spin Coherence by Optical Preparation of Nuclear Spins.* Phys. Rev. Lett. **96**, 136401 (2006).

[141] Koppens, F. H. L. *et al. Control and Detection of Singlet-Triplet Mixing in a Random Nuclear Field.* Science **309**, 1346 (2005).

[142] Vink, I. T., Nowack, K. C., Koppens, F. H. L., Danon, J., Nazarov, Y. V. & Vandersypen, L. M. K. *Locking electron spins into magnetic resonance by electron-nuclear feedback.* Nat. Phys. **5**, 764 (2009).

[143] Bluhm, H., Foletti, S., Neder, I., Rudner, M., Mahalu, D., Umansky, V. & Yacoby, A. *Dephasing time of GaAs electron-spin qubits coupled to a nuclear bath exceeding* $200\,\mu s$. Nat. Phys. **7**, 109 (2011).

[144] Petersen, G., Hoffmann, E. A., Schuh, D., Wegscheider, W., Giedke, G. & Ludwig, S. *Large Nuclear Spin Polarization in Gate-Defined Quantum Dots Using a Single-Domain Nanomagnet.* Phys. Rev. Lett. **110**, 177602 (2013).

[145] Balasubramanian, G. *et al. Ultralong spin coherence time in isotopically engineered diamond.* Nat. Mater. **8**, 383 (2009).

[146] Morton, J. J. L., McCamey, D. R., Eriksson, M. A. & Lyon, S. A. *Embracing the quantum limit in silicon computing.* Nature **479**, 345 (2011).

[147] Sailer, J. *et al. A Schottky top-gated two-dimensional electron system in a nuclear spin free Si/SiGe heterostructure.* Phys. Status Solidi RRL **3**, 61 (2009).

[148] Ager, J. W. & Haller, E. E. *Isotopically engineered semiconductors: from the bulk to nanostructures.* physica status solidi (a) **203**, 3550 (2006).

[149] Feher, G., Gordon, J. P., Buehler, E., Gere, E. A. & Thurmond, C. D. *Spontaneous Emission of Radiation from an Electron Spin System.* Phys. Rev. **109**, 221 (1958).

[150] Wild, A. *et al. Few electron double quantum dot in an isotopically purified* ^{28}Si *quantum well.* Appl. Phys. Lett. **100**, 143110 (2012).

[151] Itoh, K., Hansen, W., Haller, E., Farmer, J., Ozhogin, V., Rudnev, A. & Tikhomirov, A. *High purity isotopically enriched* ^{70}Ge *and* ^{74}Ge *single crystals: Isotope separation, growth, and properties.* J. Mater. Res. **8**, 1341 (1993).

[152] Ozhogin, V., Inyushkin, A., Taldenkov, A., Tikhomirov, A., Popov, G., Haller, E. & Itoh, K. *Isotope effect in the thermal conductivity of germanium single crystals.* JETP Letters **63**, 490 (1996).

[153] Raith, M., Stano, P., Baruffa, F. & Fabian, J. *Theory of Spin Relaxation in Two-Electron Lateral Coupled Quantum Dots.* Phys. Rev. Lett. **108**, 246602 (2012).

[154] Pfund, A., Shorubalko, I., Ensslin, K. & Leturcq, R. *Suppression of Spin Relaxation in an InAs Nanowire Double Quantum Dot.* Phys. Rev. Lett. **99**, 036801 (2007).

[155] Rudner, M. S. & Levitov, L. S. *Self-Polarization and Dynamical Cooling of Nuclear Spins in Double Quantum Dots.* Phys. Rev. Lett. **99**, 036602 (2007).

[156] Madelung, O., Rössler, U. & Schulz, M. *Landolt-Börnstein, Group III Condensed Matter - Semiconductors: Group IV Elements, IV-IV and III-V Compounds, vol. 41A1b* (Springer, Berlin, 2002).

[157] Blakemore, J. S. *Semiconducting and other major properties of gallium arsenide.* J. Appl. Phys. **53**, R123 (1982).

[158] Winkler, R. *Spin-Orbit Coupling Effects in Two-Dimensional Electron and Hole Systems* (Springer, Berlin, 2003), 1st ed. edn.

[159] Yu, P. Y. & Cardona, M. *Fundamentals of Semiconductors: Physics and Materials Properties* (Springer, Berlin, 2005), 3rd edn.

[160] Harrison, P. *Quantum Wells, Wires and Dots: Theoretical and Computational Physics of Semiconductor Nanostructures* (Wiley, 2005), 2nd edn.

[161] Schäffler, F. *High-mobility Si and Ge structures.* Semicond. Sci. Technol. **12**, 1515 (1997).

[162] Paul, D. J. *Si/SiGe heterostructures: from material and physics to devices and circuits.* Semicond. Sci. Technol. **19**, R75 (2004).

[163] Dresselhaus, M. S., Dresselhaus, G. & Jorio, A. *Group Theory: Application to the Physics of Condensed Matter* (Springer, Berlin, 2008), 1st edn.

[164] Ando, T., Fowler, A. B. & Stern, F. *Electronic properties of two-dimensional systems.* Rev. Mod. Phys. **54**, 437 (1982).

[165] Li, Q., Cywinski, Ł., Culcer, D., Hu, X. & Das Sarma, S. *Exchange coupling in silicon quantum dots: Theoretical considerations for quantum computation.* Phys. Rev. B **81**, 085313 (2010).

[166] Culcer, D., Cywiński, Ł., Li, Q., Hu, X. & Das Sarma, S. *Quantum dot spin qubits in silicon: Multivalley physics.* Phys. Rev. B **82**, 155312 (2010).

[167] Friesen, M. & Coppersmith, S. N. *Theory of valley-orbit coupling in a Si/SiGe quantum dot.* Phys. Rev. B **81**, 115324 (2010).

[168] Friesen, M., Chutia, S., Tahan, C. & Coppersmith, S. N. *Valley splitting theory of SiGe/Si/SiGe quantum wells.* Phys. Rev. B **75**, 115318 (2007).

[169] Ando, T. *Valley splitting in the silicon inversion layer: Misorientation effects.* Phys. Rev. B **19**, 3089 (1979).

[170] Weitz, P., Haug, R., von. Klitzing, K. & Schäffler, F. *Tilted magnetic field studies of spin- and valley-splittings in Si/Si$_{1-x}$Ge$_x$ heterostructures.* Surf. Sci. **361**, 542 (1996).

[171] Goswami, S. *et al. Controllable valley splitting in silicon quantum devices.* Nat. Phys. **3**, 41 (2007).

[172] Saraiva, A. L., Calderón, M. J., Hu, X., Das Sarma, S. & Koiller, B. *Physical mechanisms of interface-mediated intervalley coupling in Si.* Phys. Rev. B **80**, 081305 (2009).

[173] Borselli, M. G. *et al. Measurement of valley splitting in high-symmetry Si/SiGe quantum dots.* Appl. Phys. Lett. **98**, 123118 (2011).

[174] Lim, W. H., Yang, C. H., Zwanenburg, F. A. & Dzurak, A. S. *Spin filling of valley–orbit states in a silicon quantum dot.* Nanotechnology **22**, 335704 (2011).

[175] Zwanenburg, F. A. *et al. Silicon Quantum Electronics.* arxiv:1206.5202 (unpublished).

[176] Koester, S. J., Ismail, K. & Chu, J. O. *Determination of spin- and valley-split energy levels in strained Si quantum wells.* Semicond. Sci. Technol. **12**, 384 (1997).

[177] Schumacher, H. W., Nauen, A., Zeitler, U., Haug, R. J., Weitz, P., Jansen, A. G. M. & Schäffler, F. *Anomalous coincidences between valley split Landau levels in a Si/SiGe heterostructure.* Physica B **256**, 260 (1998).

[178] Khrapai, V. S., Shashkin, A. A. & Dolgopolov, V. T. *Strong enhancement of the valley splitting in a two-dimensional electron system in silicon.* Phys. Rev. B **67**, 113305 (2003).

[179] Lai, K., Pan, W., Tsui, D. C., Lyon, S., Mühlberger, M. & Schäffler, F. *Two-Flux Composite Fermion Series of the Fractional Quantum Hall States in Strained Si.* Phys. Rev. Lett. **93**, 156805 (2004).

[180] Wilde, M. A. *et al. Direct measurements of the spin and valley splittings in the magnetization of a Si/SiGe quantum well in tilted magnetic fields.* Phys. Rev. B **72**, 165429 (2005).

[181] Boykin, T. B. *et al. Valley splitting in strained silicon quantum wells.* Appl. Phys. Lett. **84**, 115 (2004).

[182] Friesen, M., Eriksson, M. A. & Coppersmith, S. N. *Magnetic field dependence of valley splitting in realistic Si/SiGe quantum wells.* Appl. Phys. Lett. **89**, 202106 (2006).

[183] Lee, S. & von Allmen, P. *Magnetic-field dependence of valley splitting in Si quantum wells grown on tilted SiGe substrates.* Phys. Rev. B **74**, 245302 (2006).

[184] von Allmen, P. & Lee, S. *Zero valley splitting at zero magnetic field for strained Si/SiGe quantum wells grown on tilted substrates.* arXiv:cond-mat/0606395 (unpublished).

[185] Saraiva, A. L., Calderón, M. J., Capaz, R. B., Hu, X., Das Sarma, S. & Koiller, B. *Intervalley coupling for interface-bound electrons in silicon: An effective mass study.* Phys. Rev. B **84**, 155320 (2011).

[186] McGuire, L. M., Friesen, M., Slinker, K. A., Coppersmith, S. N. & Eriksson, M. A. *Valley splitting in a Si/SiGe quantum point contact.* New J. Phys. **12**, 033039 (2010).

[187] Ouisse, T., Maude, D., Horiguchi, S., Ono, Y., Takahashi, Y., Murase, K. & Cristoloveanu, S. *Subband structure and anomalous valley splitting in ultra-thin silicon-on-insulator MOSFET's.* Physica B **249**, 731 (1998).

[188] Takashina, K., Ono, Y., Fujiwara, A., Takahashi, Y. & Hirayama, Y. *Valley Polarization in Si(100) at Zero Magnetic Field.* Phys. Rev. Lett. **96**, 236801 (2006).

[189] Takashina, K., Fujiwara, A., Horiguchi, S., Takahashi, Y. & Hirayama, Y. *Valley splitting control in* $SiO_2/Si/SiO_2$ *quantum wells in the quantum Hall regime.* Phys. Rev. B **69**, 161304 (2004).

[190] Culcer, D., Cywinski, Ł., Li, Q., Hu, X. & Das Sarma, S. *Realizing singlet-triplet qubits in multivalley Si quantum dots.* Phys. Rev. B **80**, 205302 (2009).

[191] Lai, N. S. *et al. Pauli Spin Blockade in a Highly Tunable Silicon Double Quantum Dot.* Sci. Rep. **1**, 110 (2011).

[192] Hayes, R. R. *et al. Lifetime measurements (T1) of electron spins in Si/SiGe quantum dots.* arXiv:0908.0173 (unpublished).

[193] Culcer, D., Saraiva, A. L., Koiller, B., Hu, X. & Das Sarma, S. *Valley-Based Noise-Resistant Quantum Computation Using Si Quantum Dots.* Phys. Rev. Lett. **108**, 126804 (2012).

[194] Yang, L., Watling, J. R., Wilkins, R. C. W., Boriçi, M., Barker, J. R., Asenov, A. & Roy, S. *Si/SiGe heterostructure parameters for device simulations.* Semicond. Sci. Technol. **19**, 1174 (2004).

[195] Eriksson, M. A. *et al. Spin-Based Quantum Dot Quantum Computing in Silicon.* Quantum Inf. Proc. **3**, 133 (2004).

[196] Coish, W. A. & Baugh, J. *Nuclear spins in nanostructures.* physica status solidi (b) **246**, 2203 (2009).

[197] Fabian, J. & Das Sarma, S. *Spin Relaxation of Conduction Electrons in Polyvalent Metals: Theory and a Realistic Calculation.* Phys. Rev. Lett. **81**, 5624 (1998).

[198] Elzerman, J. M., Hanson, R., Willems van Beveren, L. H., Witkamp, B., Vandersypen, L. M. K. & Kouwenhoven, L. P. *Single-shot read-out of an individual electron spin in a quantum dot.* Nature **430**, 431 (2004).

[199] Stano, P. & Fabian, J. *Orbital and spin relaxation in single and coupled quantum dots.* Phys. Rev. B **74**, 045320 (2006).

[200] Mahan, G. *Many particle physics* (Kluwer, 2000), 3rd edn.

[201] Herring, C. & Vogt, E. *Transport and Deformation-Potential Theory for Many-Valley Semiconductors with Anisotropic Scattering.* Phys. Rev. **101**, 944 (1956).

[202] Prada, M., Blick, R. H. & Joynt, R. *Singlet-triplet relaxation in two-electron silicon quantum dots.* Phys. Rev. B **77**, 115438 (2008).

[203] Wang, L., Shen, K., Sun, B. Y. & Wu, M. W. *Singlet-triplet relaxation in multivalley silicon single quantum dots.* Phys. Rev. B **81**, 235326 (2010).

[204] Pop, E., Dutton, R. W. & Goodson, K. E. *Analytic band Monte Carlo model for electron transport in Si including acoustic and optical phonon dispersion.* J. Appl. Phys. **96**, 4998 (2004).

[205] Dür, M., Gunther, A. D., Vasileska, D. & Goodnick, S. M. *Acoustic phonon scattering in silicon quantum dots.* Nanotechnology **10**, 142 (1999).

[206] Fujisawa, T., Austing, D. G., Tokura, Y., Hirayama, Y. & Tarucha, S. *Allowed and forbidden transitions in artificial hydrogen and helium atoms.* Nature **419**, 278 (2002).

[207] Sasaki, S., Fujisawa, T., Hayashi, T. & Hirayama, Y. *Electrical pump-and probe study of spin singlet-triplet relaxation in a quantum dot.* Phys. Rev. Lett. **95**, 056803 (2005).

[208] Meunier, T. *et al. Experimental signature of phonon-mediated spin relaxation in a two-electron quantum dot.* Phys. Rev. Lett. **98**, 126601 (2007).

[209] Petta, J. R., Johnson, A. C., Yacoby, A., Marcus, C. M., Hanson, M. P. & Gossard, A. C. *Pulsed-gate measurements of the singlet-triplet relaxation time in a two-electron double quantum dot.* Phys. Rev. B **72**, 161301 (2005).

[210] Amasha, S., MacLean, K., Radu, I. P., Zumbühl, D. M., Kastner, M. A., Hanson, M. P. & Gossard, A. C. *Electrical Control of Spin Relaxation in a Quantum Dot.* Phys. Rev. Lett. **100**, 046803 (2008).

[211] Semenov, Y. G. & Kim, K. W. *Elastic spin-relaxation processes in semiconductor quantum dots.* Phys. Rev. B **75**, 195342 (2007).

[212] Pan, W., Yu, X. Z. & Shen, W. Z. *Spin relaxation in silicon coupled quantum dots.* Appl. Phys. Lett. **95**, 013103 (2009).

[213] Tyryshkin, A. *et al. Electron spin coherence in Si.* Physica E **35**, 257 (2006).

[214] Xiao, M., House, M. G. & Jiang, H. W. *Measurement of the Spin Relaxation Time of Single Electrons in a Silicon Metal-Oxide-Semiconductor-Based Quantum Dot.* Phys. Rev. Lett. **104**, 096801 (2010).

[215] Lim, W. H., Zwanenburg, F. A., Huebl, H., Mottonen, M., Chan, K. W., Morello, A. & Dzurak, A. S. *Observation of the single-electron regime in a highly tunable silicon quantum dot.* Appl. Phys. Lett. **95**, 242102 (2009).

[216] Simmons, C. B. *et al. Single-electron quantum dot in Si/SiGe with integrated charge sensing.* Appl. Phys. Lett. **91**, 213103 (2007).

[217] McMullan, D. *Scanning electron microscopy 1928–1965.* Scanning **17**, 175 (1995).

[218] Lu, W., Ji, Z., Pfeiffer, L., West, K. W. & Rimberg, A. J. *Real-time detection of electron tunneling in a quantum dot.* Nature **423**, 422 (2003).

[219] Hanson, R., Witkamp, B., Vandersypen, L. M. K., van Beveren, L. H. W., Elzerman, J. M. & Kouwenhoven, L. P. *Zeeman energy and spin relaxation in a one-electron quantum dot.* Phys. Rev. Lett. **91**, 196802 (2003).

[220] Hanson, R. *et al. Single-shot readout of electron spin states in a quantum dot using spin-dependent tunnel rates.* Phys. Rev. Lett. **94**, 196802 (2005).

[221] Leggett, A., Ruggiero, B. & Silvestrini, P. *Quantum Computing and Quantum Bits in Mesoscopic Systems* (Springer, 2004).

[222] Elzerman, J. M. *et al. Few-electron quantum dot circuit with integrated charge read out.* Phys. Rev. B **67**, 161308R (2003).

[223] Dovzhenko, Y., Stehlik, J., Petersson, K. D., Petta, J. R., Lu, H. & Gossard, A. C. *Nonadiabatic quantum control of a semiconductor charge qubit.* Phys. Rev. B **84**, 161302 (2011).

[224] Blick, R. H., Haug, R. J., Weis, J., Pfannkuche, D., v. Klitzing, K. & Eberl, K. *Single-electron tunneling through a double quantum dot: The artificial molecule.* Phys. Rev. B **53**, 7899 (1996).

[225] Blick, R. H., Pfannkuche, D., Haug, R. J., v. Klitzing, K. & Eberl, K. *Formation of a Coherent Mode in a Double Quantum Dot.* Phys. Rev. Lett. **80**, 4032 (1998).

[226] Petta, J. *Ultra-Coherent Spin Qubits* (Retrieved April, 2013). URL `http://pettagroup.princeton.edu/sige.html`.

[227] Morello, A. *et al. Single-shot readout of an electron spin in silicon.* Nature **467**, 687 (2010).

[228] Tahan, C., Friesen, M. & Joynt, R. *Decoherence of electron spin qubits in Si-based quantum computers.* Phys. Rev. B **66**, 035314 (2002).

[229] Culcer, D., Hu, X. & Das Sarma, S. *Dephasing of Si spin qubits due to charge noise.* Appl. Phys. Lett. **95**, 073102 (2009).

[230] Climente, J. I., Bertoni, A., Goldoni, G., Rontani, M. & Molinari, E. *Triplet-Singlet Spin Relaxation in Quantum Dots with Spin-Orbit Coupling.* Phys. Rev. B **75**, 081303(R) (2007).

[231] Golovach, V. N., Khaetskii, A. & Loss, D. *Spin relaxation at the singlet-triplet crossing in a quantum dot.* Phys. Rev. B **77**, 045328 (2008).

[232] Chaney, D. & Maksym, P. *Size-dependent suppression of spin relaxation in electrostatic quantum dots.* Phys. Rev. B **75**, 035323 (2007).

[233] Shen, K. & Wu, M. W. *Triplet-singlet relaxation in semiconductor single and double quantum dots.* Phys. Rev. B **76**, 235313 (2007).

[234] Florescu, M. & Hawrylak, P. *Spin relaxation in lateral quantum dots: Effects of spin-orbit interaction.* Phys. Rev. B **73**, 045304 (2006).

[235] Olendski, O. & Shahbazyan, T. V. *Theory of anisotropic spin relaxation in quantum dots.* Phys. Rev. B **75**, 041306(R) (2007).

[236] Wang, L. & Wu, M. W. *Singlet-triplet relaxation in SiGe/Si/SiGe double quantum dots.* J. Appl. Phys. **110**, 043716 (2011).

[237] Golovach, V. N., Khaetskii, A. & Loss, D. *Phonon-Induced Decay of the Electron Spin in Quantum Dots.* Phys. Rev. Lett. **93**, 016601 (2004).

[238] Stano, P. & Fabian, J. *Theory of Phonon-Induced Spin Relaxation in Laterally Coupled Quantum Dots.* Phys. Rev. Lett. **96**, 186602 (2006).

[239] Raith, M. *Orbital Effects of Transverse Magnetic Fields in Quasi Two-Dimensional Electron Systems.* Diploma thesis, University of Regensburg, Germany (2009).

[240] Pedersen, J., Flindt, C., Mortensen, N. A. & Jauho, A.-P. *Failure of standard approximations of the exchange coupling in nanostructures.* Phys. Rev. B **76**, 125323 (2007).

[241] Stano, P. & Fabian, J. *Control of electron spin and orbital resonances in quantum dots through spin-orbit interactions.* Phys. Rev. B **77**, 045310 (2008).

[242] Bychkov, Y. A. & Rashba, E. I. *Oscillatory effects and the magnetic susceptibility of carriers in inversion layers.* J. Phys. C **17**, 6039 (1984).

[243] Dresselhaus, G. *Spin orbit coupling effects in zinc blende structures.* Phys. Rev. **100**, 580 (1955).

[244] Golub, L. E. & Ivchenko, E. L. *Spin splitting in symmetrical SiGe quantum wells.* Phys. Rev. B **69**, 115333 (2004).

[245] Nestoklon, M. O., Ivchenko, E. L., Jancu, J.-M. & Voisin, P. *Electric field effect on electron spin splitting in* SiGe/Si *quantum wells.* Phys. Rev. B **77**, 155328 (2008).

[246] Grodecka, A., Jacak, L., Machnikowski, P. & Roszak, K. *Phonon impact on the coherent control of quantum states in semiconductor quantum dots* (Nova Science, New York, 2005).

[247] Hasegawa, H. *Spin-Lattice Relaxation of Shallow Donor States in Ge and Si through a Direct Phonon Process.* Phys. Rev. **118**, 1523 (1960).

[248] Dirac, P. A. M. *The Quantum Theory of the Emission and Absorption of Radiation.* Proceedings, RSL **114**, 243 (1927).

[249] Fermi, E. *Nuclear Physics: A Course Given by Enrico Fermi at the University of Chicago* (University Of Chicago Press, 1950), rev. edn.

[250] Ashoori, R. C., Stormer, H. L., Weiner, J. S., Pfeiffer, L. N., Baldwin, K. W. & West, K. W. *N-electron ground state energies of a quantum dot in magnetic field.* Phys. Rev. Lett. **71**, 613 (1993).

[251] de Sousa, R. & Das Sarma, S. *Gate control of spin dynamics in III-V semiconductor quantum dots.* Phys. Rev B **68**, 155330 (2003).

[252] Kuan, W. H., Tang, C. S. & Xu, W. *Energy levels of a parabolically confined quantum dot in the presence of spin-orbit interaction.* J. Appl. Phys. **95**, 6368 (2004).

[253] Tsitsishvili, E., Lozano, G. S. & Gogolin, A. O. *Rashba coupling in quantum dots: An exact solution.* Phys. Rev. B **70**, 115316 (2004).

[254] Bulgakov, E. N. & Sadreev, A. F. *Spin polarization in quantum dots by radiation field with circular polarization.* JETP Letters **73**, 505 (2001).

[255] Destefani, C. F. & Ulloa, S. E. *Anisotropic electron g factor in quantum dots with spin-orbit interaction.* Phys. Rev. B **71**, 161303(R) (2005).

[256] Stano, P. & Fabian, J. *Spin-orbit effects in single-electron states in coupled quantum dots.* Phys. Rev. B **72**, 155410 (2005).

[257] Nowak, M. P. & Szafran, B. *Coupling of bonding and antibonding electron orbitals in double quantum dots by spin-orbit interaction.* Phys. Rev. B **81**, 235311 (2010).

[258] Pangerl, T. *Spin relaxation in single electron GaAs based lateral coupled double quantum dots in the presence of spin-orbit coupling and hyperfine coupling.* Bachelor thesis, University of Regensburg, Germany (2012).

[259] Raith, M., Stano, P. & Fabian, J. *Theory of single electron spin relaxation in Si/SiGe lateral coupled quantum dots.* Phys. Rev. B **83**, 195318 (2011).

[260] Rieger, M. M. & Vogl, P. *Electronic-band parameters in strained $Si_{1-x}Ge_x$ alloys on $Si_{1-y}Ge_y$ substrates.* Phys. Rev. B **48**, 14276 (1993).

[261] Malissa, H., Jantsch, W., Mühlberger, M., Schäffler, F., Wilamowski, Z., Draxler, M. & Bauer, P. *Anisotropy of g-factor and electron spin resonance linewidth in modulation doped SiGe quantum wells.* Appl. Phys. Lett. **85**, 1739 (2004).

[262] Gandolfo, D. S., Williams, D. A. & Qin, H. *Characterization of a silicon–germanium quantum dot structure at 4.2 K and 40 mK.* J. Appl. Phys. **97**, 063710 (2005).

[263] Fischetti, M. V. & Laux, S. E. *Band structure, deformation potentials, and carrier mobility in strained Si, Ge, and SiGe alloys.* J. Appl. Phys. **80**, 2234 (1996).

[264] Peierls, R. *Zur Theorie des Diamagnetismus von Leitungselektronen.* Zeitschrift für Physik **80**, 763 (1933).

[265] Fock, V. *Bemerkung zur Quantelung des harmonischen Oszillators im Magnetfeld.* Zeitschrift für Physik **47**, 446 (1928).

[266] Darwin, C. G. *The Diamagnetism of the Free Electron.* Proceedings, CPS **27**, 86 (1931).

[267] Löwdin, P. *A Note on the Quantum-Mechanical Perturbation Theory.* J. Chem. Phys. **19**, 1396 (1951).

[268] Schrieffer, J. R. & Wolff, P. A. *Relation between the Anderson and Kondo Hamiltonians.* Phys. Rev. **149**, 491 (1966).

[269] Simmons, C. B. *et al.* *Charge Sensing and Controllable Tunnel Coupling in a Si/SiGe Double Quantum Dot.* Nano Lett. **9**, 3234 (2009).

[270] Aleiner, I. L. & Fal'ko, V. I. *Spin-Orbit Coupling Effects on Quantum Transport in Lateral Semiconductor Dots.* Phys. Rev. Lett. **87**, 256801 (2001).

[271] Könemann, J., Haug, R. J., Maude, D. K., Fal'ko, V. I. & Altshuler, B. L. *Spin-orbit coupling and anisotropy of spin-splitting in quantum dots.* Phys. Rev. Lett. **94**, 226404 (2005).

[272] Tokatly, I. & Sherman, E. *Gauge theory approach for diffusive and precessional spin dynamics in a two-dimensional electron gas.* Annals of Physics **325**, 1104 (2010).

[273] Erlingsson, S. I., Nazarov, Y. V. & Fal'ko, V. I. *Nucleus-mediated spin-flip transitions in GaAs quantum dots.* Phys. Rev. B **64**, 195306 (2001).

[274] Mizuno, H., Taniguchi, K. & Hamaguchi, C. *Electron-transport simulation in silicon including anisotropic phonon scattering rate.* Phys. Rev. B **48**, 1512 (1993).

[275] Baruffa, F. *Spin-orbit coupling effects in two-electron coupled quantum dots.* Ph.D. thesis, University of Regensburg, Germany (2010).

[276] Assali, L. V. C., Petrilli, H. M., Capaz, R. B., Koiller, B., Hu, X. & Das Sarma, S. *Hyperfine interactions in silicon quantum dots.* Phys. Rev. B **83**, 165301 (2011).

[277] Khaetskii, A., Loss, D. & Glazman, L. *Electron spin evolution induced by interaction with nuclei in a quantum dot.* Phys. Rev. B **67**, 195329 (2003).

[278] Merkulov, I. A., Efros, A. L. & Rosen, M. *Electron spin relaxation by nuclei in semiconductor quantum dots.* Phys. Rev. B **65**, 205309 (2002).

[279] Slater, J. C. *The Theory of Complex Spectra.* Phys. Rev. **34**, 1293 (1929).

[280] Baruffa, F., Stano, P. & Fabian, J. *Theory of Anisotropic Exchange in Laterally Coupled Quantum Dots.* Phys. Rev. Lett. **104**, 126401 (2010).

[281] Baruffa, F., Stano, P. & Fabian, J. *Spin-orbit coupling and anisotropic exchange in two-electron double quantum dots.* Phys. Rev. B **82**, 045311 (2010).

[282] Reilly, D. J., Taylor, J. M., Petta, J. R., Marcus, C. M., Hanson, M. P. & Gossard, A. C. *Suppressing Spin Qubit Dephasing by Nuclear State Preparation.* Science **321**, 817 (2008).

[283] Raith, M., Stano, P. & Fabian, J. *Theory of spin relaxation in two-electron laterally coupled Si/SiGe quantum dots.* Phys. Rev. B **86**, 205321 (2012).

[284] Merkt, U., Huser, J. & Wagner, M. *Energy spectra of two electrons in a harmonic quantum dot.* Phys. Rev. B **43**, 7320 (1991).

[285] Gorkov, L. P. & Krotkov, P. L. *Exact asymptotic form of the exchange interaction between shallow centers in doped semiconductors.* Phys. Rev. B **68**, 155206 (2003).

[286] Heitler, W. & London, F. *Wechselwirkung neutraler Atome und homöopolare Bindung nach der Quantenmechanik.* Zeitschrift für Physik **44**, 455 (1927).

[287] Burkard, G., Loss, D. & DiVincenzo, D. P. *Coupled quantum dots as quantum gates.* Phys. Rev. B **59**, 2070 (1999).

[288] S. Amasha (private communication).

[289] Barthel, C., Reilly, D. J., Marcus, C. M., Hanson, M. P. & Gossard, A. C. *Rapid Single-Shot Measurement of a Singlet-Triplet Qubit.* Phys. Rev. Lett. **103**, 160503 (2009).

[290] De Franceschi, S., Sasaki, S., Elzerman, J. M., van der Wiel, W. G., Tarucha, S. & Kouwenhoven, L. P. *Electron cotunneling in a semiconductor quantum dot.* Phys. Rev. Lett. **86**, 878 (2001).

[291] Yafet, Y. *g Factors and Spin-Lattice Relaxation of Conduction Electrons.* vol. 14 of *Solid State Physics*, 1 (Academic Press, 1963).

[292] Preskill, J. *Reliable quantum computers.* Proceedings, RSL **454**, 385 (1998).

[293] Türeci, H. E. & Alhassid, Y. *Spin-orbit interaction in quantum dots in the presence of exchange correlations: An approach based on a good-spin basis of the universal Hamiltonian.* Phys. Rev. B **74**, 165333 (2006).

[294] Kimball, G. E. & Shortley, G. H. *The Numerical Solution of Schrödinger's Equation.* Phys. Rev. **45**, 815 (1934).

[295] Spiegel, M. R. *Endliche Differenzen und Differenzengleichungen* (McGraw Hill, 1982).

[296] Datta, S. *Electronic Transport in Mesoscopic Systems* (Cambridge University Press, 1997).

[297] Wimmer, M. *Quantum transport in nanostructures: From computational concepts to spintronics in graphene and magnetic tunnel junctions*. Ph.D. thesis, University of Regensburg, Germany (2008).

[298] Cheng, A. H.-D. & Cheng, D. T. *Heritage and early history of the boundary element method*. Eng. Anal. Boundary Elements **29**, 268 (2005).

[299] Lanczos, C. *An Iteration Method for the Solution of the Eigenvalue Problem of Linear Differential and Integral Operators*. J. Res. Natl. Bur. Stand. **45**, 255 (1950).

[300] Anderson, E. *et al.* *LAPACK Users' Guide* (Society for Industrial and Applied Mathematics, 1999), third edn.

[301] Lehoucq, R., Maschhoff, K., Sorensen, D. & Yang, C. *ARPACK — Arnoldi Package* (Retrieved April, 2013). URL `http://www.caam.rice.edu/software/ARPACK/`.

[302] Cramer, C. J. *Essentials of Computational Chemistry: Theories and Models* (Wiley, 2004), 2nd edn.

[303] Tinkham, M. *Group Theory and Quantum Mechanics* (Dover Publications, New York, 2003), 1st edn.

[304] Arfken, G. B., Weber, H. J. & Harris, F. E. *Mathematical Methods for Physicists* (Academic Press, 2005), 6th edn.

[305] Frigo, M. & Johnson, S. G. *Fastest Fourier Transform in the West (FFTW)* (Retrieved April, 2013). URL `http://www.fftw.org`.

[306] Press, W. H., Teukolsky, S. A., Vetterling, W. T. & Flannery, B. P. *Numerical Recipes 3rd Edition: The Art of Scientific Computing* (Cambridge University Press, 2007), 3rd edn.

[307] Abramowitz, M. & Stegun, I. A. *Handbook of Mathematical Functions: with Formulas, Graphs, and Mathematical Tables* (Dover Publications, 1965).

Acknowledgment

"If I have seen further it is by standing on the shoulders of giants." The famous words by Isaac Newton[3] have never been more suitable. The giants of my personal career have even helped me all the way up to their shoulders, where I was able to see as far as I have never seen before. This is why I want to dedicate the following lines to them. Without their patience and perseverance I would still be sitting on the ground playing in the sandpit.

First of all, I want to thank my supervisor and mentor Prof. Dr. Jaroslav Fabian for the continuous support and his faith in me. It was truly inspiring to work in your group and to be part of the team. Thank you also for making the time in Munich possible! Special thanks go to Dr. Peter Staňo for his patience and perseverance. I wish you with all my heart all the best for your private and professional future! Our secretary Angela Reißer was a great support for administrative things of any kind. Thank you so much for all your work done! My colleagues Dr. Benedikt Scharf and Sebastian Putz have always been great teammates, confederates, and friends. I want you to know that I am particularly thankful for your support and encouragement during the last years! Moreover, I want to thank all other members of the group, namely Dr. Alex Matos-Abiague, Dr. Martin Gmitra, Dr. Denis Kochan, and Dr. Carlos López-Monís, and also the former members Dr. Fabio Baruffa, Dr. Christian Ertler, and Dr. Sergej Konschuh for an excellent atmosphere in the group and all the things that I have learnt from you. And not to forget, I want to express my gratitude to Michael Jobst, Dr. Björn Erbe, Jan Bundesmann, Dr. Viktor Krückl, Dr. Michael Wimmer, and many others. Last but not least, I want to thank my family and all my friends for their help and support!

This work was enabled by the Deutsche Forschungsgemeinschaft via their programs SPP 1285 and SFB 689. I gladly acknowledge the DFG for their support.

---

[3] In fact, the first documented use of this metaphor gives credit to Bernard of Chartres, in the twelfth century.

CURRICULUM VITAE

PERSONAL DATA

Name	Martin Raith
Date of birth	22.Apr.1983
Place of birth	Regensburg
Nationality	German

POSITIONS

2009-	Universität Regensburg, Research and Teaching Assistant

EDUCATION

2009-	Universität Regensburg, Ph.D. Student
2006-2009	Universität Regensburg, Physics Student
2005-2006	Trinity College of Dublin, Physics Student
2003-2005	Universität Regensburg, Physics Student
1993-2002	Gymnasium Neutraubling, Student

MILITARY SERVICE

2002-2003	Bayreuth and Bad Kötzting, Motorcar Mechanic